Targeting tumor tight junctions: The Junction Opener protein

Jiho Kim

A dissertation
submitted in partial fulfillment of the
requirements for the degree of

Doctor of Philosophy

University of Washington
2020

Reading Committee:
Darrick Carter, Chair
Paul Lampe
Andre Lieber
Steve Reed
Roland Strong

Program Authorized to Offer Degree:
Pathobiology

University of Washington

Abstract

Targeting tumor tight junctions: The Junction Opener protein

Jiho Kim

Chair of the Supervisory Committee:

Darrick Carter

Department of Global Health

With the advent of new approaches - including cellular therapy and immunotherapies - cancer treatment has entered a new era. However, solid epithelial tumors have yet to benefit from these new modalities, and new tools for diagnosis and treatment are sorely needed. Desmoglein-2 (DSG2) is a desmosomal protein involved in cellular structure integrity and junction formation, contributing to the formation of tight physical barriers. Several cancers have been observed to upregulate its expression to resist therapies and the immune system, representing its potential as a biomarker and target. This dissertation explores the identification of DSG2 as a biomarker and prognostic indicator for ovarian cancer, which commonly manifests as an epithelial solid tumor. DSG2 overexpression was linked to survival, chemoresistance, and prognosis. A recombinant, engineered adenoviral protein, Junction Opener (JO) targets DSG2 and causes the transient opening of tight junction allowing easier passage of chemotherapeutics. JO's ability to home to

overexpressed DSG2 and to compromise one of a tumor's defense mechanisms makes it an attractive co-therapeutic with monoclonal antibodies or chemotherapeutics. A conjugatable form of JO, JOC-x, was developed and confirmed to retain JO's properties and binding characteristics. JOC-x was then successfully conjugated to PEGylated liposomal doxorubicin (PLD) and was shown to have enhanced efficacy over the separate combination, thus indicating its potential as a chemotherapeutic candidate. Finally, we explored the pharmacokinetic and immunogenic properties of JO and PLD in *Macaca fascicularis* to ascertain parameters for future use in humans. Macaque studies indicated induction of anti-JO antibodies and inflammatory cytokines, but these could be suppressed with an immunosuppressive regimen commonly found in the clinic. In short, this dissertation explores the establishment of DSG2 as an ovarian cancer biomarker and therapeutic target for the JO protein as tools to use in ovarian cancer diagnosis and treatment.

Grandescunt Aucta Labore

Tuum Est

Lux sit

TABLE OF CONTENTS

Chapter 1

LIST OF FIGURES

LIST OF TABLES

ACKNOWLEDGEMENTS

In completing this dissertation there are many people to thank, and nary impossible to address in a short paragraph. Many thanks to Dr. Darrick Carter and Dr. Andre Lieber, who as co-supervisors were instrumental in guiding my scientific progress and growth. Their expertise and advice, through times good and bad, helped immensely in navigating a field that was at first foreign to me. Thanks to the lab members in both Carter and Lieber labs who went out of their way to accommodate even the slightest issue or question. Particular thanks to Dr. Sean Gray for his supervision and guidance at PAI Life Sciences as another mentor figure who provided much scientific opinion and a humorous side to science throughout my years there.

I deeply appreciate the support shown by my friends worldwide, reflective of my life on the move – from Toronto, Montreal, Vancouver, Uganda, Seattle, Korea and elsewhere. While many of them were not here to experience the PhD process with me, their support (spoken and unspoken) will always be a source of inspiration and emotional support. Finally, none of this would ever have been possible without the unwavering support of my family – my parents and sisters. Although as a family we have been through many trials and tribulations, our bonds remain strong and it is my hope that they will endure so. All of you continue to impress me and inspire me in the way you live life, however arduous it may be.

To myself – likely the only one reading this again a few years in the future – it is no easy task to complete a doctorate, beginning from scratch. A new field, a new city, a new country, full of uncertainties. Those uncertainties will most certainly continue, and it is my sincere hope that reflecting back upon this, you will truly appreciate what was done and that you will try your utmost to ensure that you have no regrets in living a life which has certainly been a thrill thus far.

LIST OF ABBREVIATIONS

Ad	Adenovirus
AUC	Area under curve
CAR	Coxsackie and Adenovirus Receptor
CAR-T	Chimeric Antigen Receptor T-cells
CRS	Cytokine Release Syndrome
DLS	Dynamic Light Scattering
DSG2	Desmoglein-2
ELISA	Enzyme-linked immunosorbent assay
EMT	Epthelial-to-mesenchymal transition
FBS	Fetal Bovine Serum
GFP	Green fluorescent protein
HRP	Horseradish peroxidase
IHC	Immunohistochemistry
JO	Junction Opener
JOC-LD	JOC conjugated to Liposomal Doxorubicin
JOC-x	Junction Opener conjugable to x
NHP	Non-human primate
OS	Overall survival
Ovc	Ovarian Cancer
PEG	Polyethylene Glycol

PFS	Progression-free survival
PK	Pharmacokinetics
PLD	PEGylated Liposomal Doxorubicin
SDS-PAGE	Sodium dodecyl sulfate-polyacrylamide agarose gel electrophoresis
SEC-MALS	Size exclusion chromatography – multiple angle light scattering
SPR	Surface plasmon resonance
TCGA	The Cancer Genome Atlas Program
VIA	Viral Inhibition Assay

Chapter 1 INTRODUCTION

1.1 Ovarian Cancer Biology and Epidemiology

Ovarian cancer, a solid epithelial cancer exclusively affecting women, was diagnosed in an estimated 295,414 patients worldwide in 2018, thus ranking it third in gynecologic cancers after cervical and uterine cancers (1). Ovarian cancer represents a significant proportion of cancer deaths worldwide at 161,000 in 2015 alone (2). 5-year survival rates have improved in recent years, ranging from 47% to 93% depending on the type (3).

Ovarian cancer is classified in different ways including pathology, staging, and grading. Pathological classifications can span many different cellular/tissue origins, but can be grouped into epithelial, germ cell, and sex-cord stromal (4). Cancers of ovarian origin can further be classified by the cell of origin, which includes mucinous, endometrioid, clear cell, and undifferentiated. Epithelial ovarian cancer is the most common and the most deadly of the subtypes, comprising 85-90% of all cases and has the lower 47% 5-year survival rate mentioned above (3, 5). In this dissertation epithelial ovarian cancers will be investigated in depth, as they are characterized by the biomarker and target of the Junction-Opener (JO) protein.

Like most other cancers, ovarian cancer arises upon abnormal cell growth and replication due to mutational burden and errors in DNA repair. Mutational signatures bear some similarity to breast cancer, with genes such as *BRCA1* and *BRCA2* being represented highly, although implications for testing are unclear (6). Diagnostic and prognostic testing for ovarian cancer using these gene signatures remain an unclear prospect require additional research. While treatment has advanced with the advent of immunotherapy and cellular therapy, these remain

nascent alternatives and the vast majority of treatment regimens for ovarian cancer remain chemotherapy and radiotherapy or a combination thereof (7).

1.2 Biology of Tight Junctions and Desmosomes

Cell junctions are structures formed at the intercellular points of contact (or points of contact with extracellular matrix). These junctions serve multiple purposes, including: structural integrity, attachment/anchoring, cell-cell communication, morphogenesis, and exclusion of molecules or cells (8). There are five primary types of cell junctions: desmosomes, hemidesmosomes, adherens junctions, gap junctions, tight junctions. Of these, desmosomes, hemidesmosomes and adherens junctions are primarily involved in anchoring cells to each other and to extracellular matrix and are collectively termed anchoring junctions (9). Gap junctions allow communication between cells through a tight cytoplasm-to-cytoplasm channel-like linkage for the passage of electrical (ionic), chemical or small molecule (<485 Da) passage through the junction (10). Finally, tight junctions, also referred to as zonula occludens, are extensively involved in holding cells together tightly and to exclude entry and/or exit of solutes by means of a physical barrier (11). Tight junctions play an especially important role in the maintenance of vital barriers such as the blood-brain barrier (12) and the stomach epithelium (13) where barrier integrity is of utmost importance.

Desmosomes are known as macula adherens and are specialized for the cell-to-cell adhesion. Desmosomal proteins involve a multitude of proteins, specifically desmoplakins, plakophilins, plakoglobins, desmocollins, and desmogleins. Of these, desmoplakins are involved in anchoring intermediate filaments (keratin) in the cell cytoplasm, forming the intracellular junction between the desmosome and cellular components. Plakoglobins and plakophilins act as scaffolds for the desmosomal complex, providing stability and an anchoring site between the

intracellular and extracellular components of the desmosome. Desmocollins and desmogleins are transmembrane proteins with extracellular components that reach out from the cell to other desmosomes, thus forming the cell-to-cell junction (14, 15). Desmosomes have an important function in tissues subjected to mechanical stress, such as cardiac muscle, epithelia, and the gastrointestinal mucosa (16). Desmosome dysfunction is thought to be a cause of arrhythmogenic cardiomyopathy, and autoantibodies against desmosomal proteins (Desmogleins 1,3) are thought to cause pemphigus vulgaris and pemphigus foliaceus, autoimmune disease affecting the skin epithelia which often result in blisters (17).

Tight junctions are also referred to as zonula occludens and are characterized by tight bonds between cells (<20 nm separation, excluding molecules > 400 Da). The proteins involved in these junctions are occludin and claudins which act as the integral membrane proteins, and a family of junction adhesion molecules. Occludin and claudins form a “wire mesh” network and are anchored in by zonula scaffolding proteins ZO-1 and ZO-2 in the cell cytoplasm; these proteins in turn are networked into the actin cytoskeleton. The claudin/occludin intercellular binding is further facilitated by the immunoglobulin-like JAM proteins, further contributing to the junction’s strength and integrity (11). Tight junctions’ strength and occlusiveness make them an ideal component of water(or solute)-tight barriers, and they can be found in multiple locations including the blood-brain barrier and others requiring tight barriers. Tight junctions have been recently implicated in the maintenance of cell polarization, by serving as sites for protein complexes (e.g. CRB, Par) which then mediate signaling cascades to differentiate the apical and basolateral domains of the cell (18).

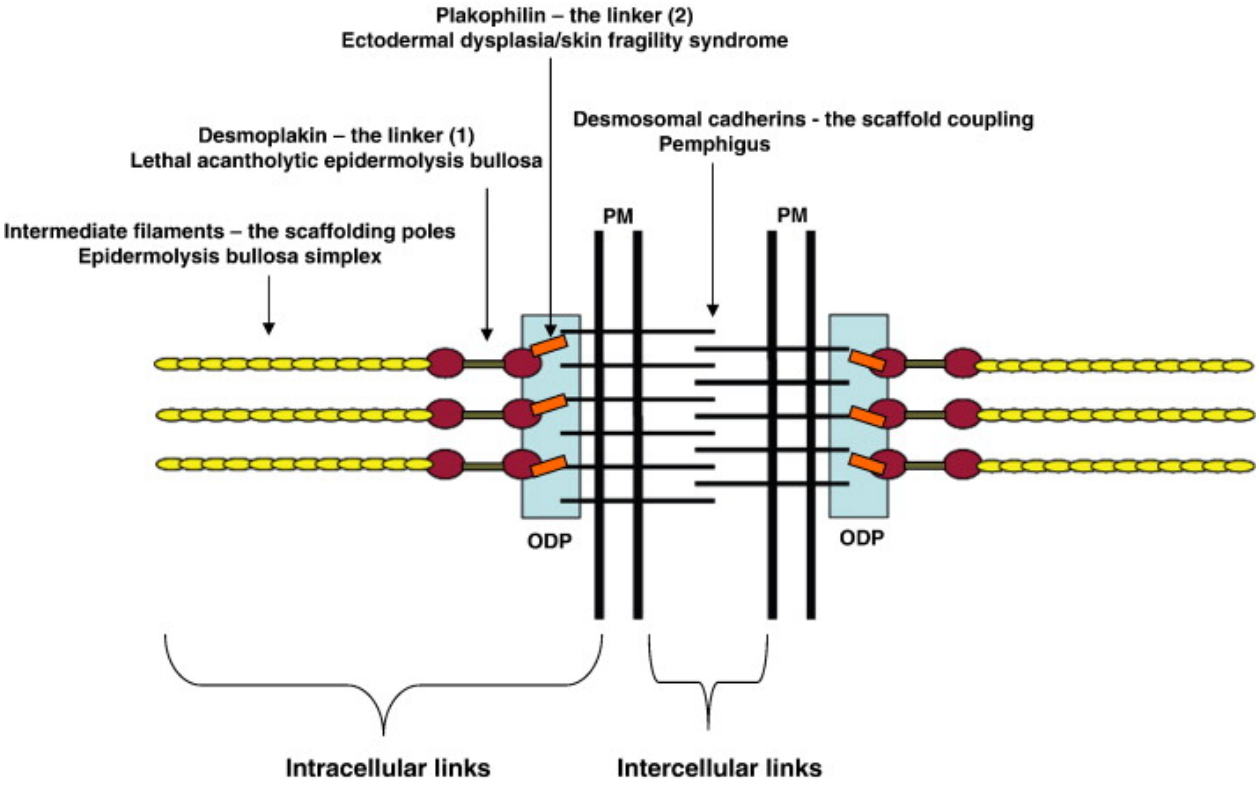

Figure 1-1 Desmosomal Structure.

Desmosomes are complex structures mediating cell-cell adhesion. Desmoglein-2, a primary focus of this dissertation, is involved in the intercellular space connecting the cell. Other protein families are involved in anchoring, intermediate filament scaffolding, and other roles. *Adapted from (19).*

1.3 Formation of Junction Barriers for Tumor Resistance

Solid epithelial tumors use multiple strategies to avoid immune detection and chemotherapeutics, eventually resulting in tumor resistance and persistence. Tumors are supported by a highly complex and dense stroma, a fundamental component of the tumor microenvironment mediating tumor proliferation, invasion, metastasis, and cell adherence. Another key function is to suppress immune function near these sites by the secretion of immunosuppressive cytokines or attraction of regulatory cells such as Tregs (20). These stroma are comprised of connective tissue, fibroblasts, osteoblasts, chondrocytes, and elastic

extracellular matrix (ECM)(21), and present a difficult barrier to breach for effector immune cells and chemotherapeutics.

Potential causes of drug resistance in solid tumors include genetically and epigenetically determined factors expressed in individual cells and those related to the solid tumor environment. The latter include tumor stroma cells, proteins that form a dense matrix, and the aforementioned junctions that seal the space between tumor cells (22). To be effective, drugs must diffuse throughout the tumor to achieve a lethal concentration in all the tumor cells. However, most drugs, and in particular nanoparticle- or liposome-based drugs (diameters ~/>100nm), do not diffuse more than a few cell layers from blood vessels implying that more distant tumor cells receive only sub-therapeutic drug exposure (22-24). Furthermore, several studies have shown that the upregulation of epithelial junction proteins correlated with increased resistance to therapy, including therapy with the two major classes of cancer drugs - monoclonal antibodies and chemotherapeutics (25-27). In summary, the epithelial phenotype of ovarian cancer cells and their ability to form physical barriers protect the tumor cells from attacks by the host immune system or from elimination by cancer therapeutics (28).

1.4 Overview of Adenoviruses

Adenoviruses are a diverse family of double-stranded DNA, unenveloped viruses, of which there are over 60 distinct serotypes (29). They were named for their initial isolation in human adenoids in 1953 (30). Adenoviruses tend to be around 90-100 nm in size and their genome sizes vary widely, ranging from 26 Kbp to 48 Kbp (31). They are known to cause mild respiratory disease in most affected subjects, with symptoms including cold-like illness, sore throat, diarrhea, and pneumonia. Severe symptoms tend to manifest in the very young or immunocompromised (32). Besides their capability to cause disease, the viruses' ability to

efficiently deliver genes to target cells, replicating or non-replicating, have made them appealing for gene therapy as a vector, and several subtypes have already been investigated as potential delivery vectors (33). Adenoviral vectors have been extensively used as treatments in gene delivery, accounting for up to 20% of gene therapy clinical trials worldwide (34). Vectors targeting monogenic disorders (e.g. cystic fibrosis, X-linked SCID, etc) and oncolytic viruses have been employed in previous trials. The primary issue with adenoviral vectors seems to be the immunogenicity of the capsid, and immune responses to it dampening the viruses' efficacy (35). To circumvent this, "gutless" adenoviruses (Also referred to as high-capacity adenoviral vectors or helper-dependent adenoviral vectors), which eliminate certain viral coding sequences, have been developed to increase the delivered gene capacity (36). The use of adenovirus as a gene delivery vector will be contingent on effective control of the innate and adaptive immune response; this is complicated by pre-existing immunity to some of the commonly used adenoviruses such as Ad5, where 37-100% of certain populations already have neutralizing antibodies(37-39).

Adenoviruses present in an icosahedral shape which contains the nucleocapsid. The capsid, which serves as protection but is also the most immunogenic component, is itself comprised of three types of major proteins: fiber, penton, and hexon (31). The knob fiber protein, which interacts with a cellular receptor, is anchored to the capsid by the penton capsomere, formed of five pentons. The diverse family of viruses have a group of human entry receptors, and several of the knob proteins have been investigated for their ability to bind and potentially disable their cell receptor targets (40). The prominent adenovirus receptor is the Coxsackie and Adenovirus receptor (CAR); group B adenoviruses bind CD46 and Ads3,7,11,14 bind DSG2(40-

42). The ability of adenoviruses to bind junction proteins to gain entry into cells has generated research into manipulating the junction protein interactions to take advantage of in solid tumors.

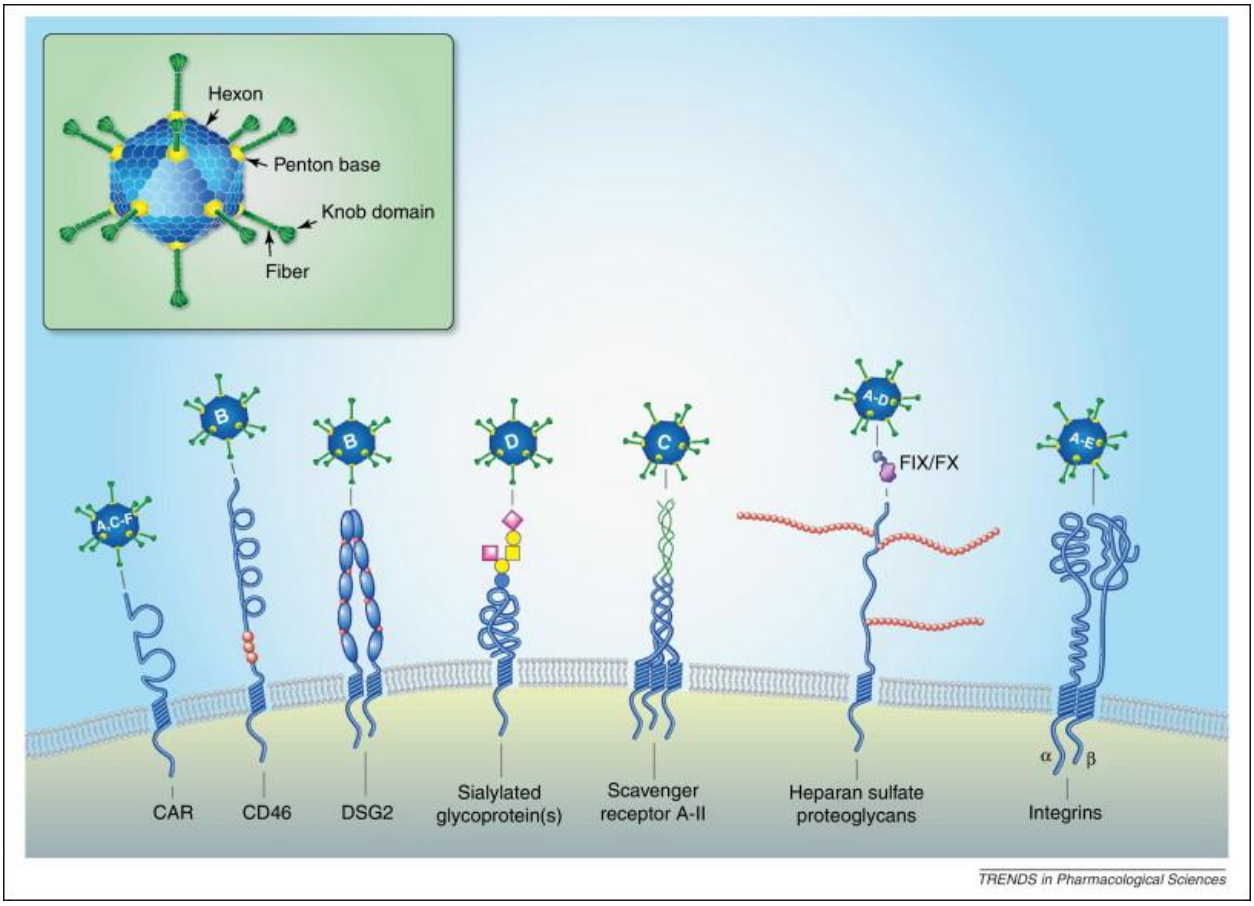

Figure 1-2 Adenovirus structure and receptor interaction.

Adenoviruses are a diverse family of viruses that are able to bind a variety of human cellular receptors. The dominant receptors are CAR and CD46, but various members can bind other cellular receptors including DSG2. *Adapted from* (43).

1.5 Adenovirus 3 and Desmoglein-2

Ad3 infection is particularly prevalent in pediatric populations, causing symptoms including respiratory illness, keratoconjunctivitis, fever, and gastroenteritis (44). In recent years Ad3 has been noted as a significant source of pediatric acute respiratory infections worldwide, accounting for an estimated 15 to 87 % of adenoviral respiratory infections, a definite increase from the 1960-1970s indicating 13% of all adenoviral respiratory infections (45). Ad3's human receptor has only been recently elucidated as desmoglein-2 (40), a desmosomal protein highly expressed in epithelium or cardiomyocytes.

Adenovirus subtype 3 binds DSG2 as its cellular receptor (40). DSG2 is a member of the desmosomal cadherin family (46), and plays a crucial role in the formation of desmosomes which form tight epithelial junctions and keep intercellular structure intact (19). Taking advantage of these very effective means of forming tight junctions, epithelial tumors often display upregulated expression of DSG2. This overexpression varies across multiple types of epithelial tumors including colorectal (47), skin carcinomas (48), prostate (49). Desmosomes are thought to play a role in precluding entry of large molecules of over 500 Da in size, which includes many forms of cancer therapies in use today(50, 51); e.g. liposomal form of doxorubicin, Doxil®, monoclonal antibodies, and cellular therapies. Thus, the upregulation of DSG2 and hijacking of the desmosome junctions seems to be one mechanism by which the tumor becomes resistant to multiple forms of modern anti-tumor treatments.

The DSG2 protein is 122 kDa in molecular mass and 1118 amino acids long. It acts as a calcium-binding transmembrane protein in the region of the intercellular space of the desmosome, mediating cell-to-cell adhesion and contact (52). It plays a particularly important role in cardiomyocytes, in which it seems to be the only member of the desmoglein family

expressed; thus, mutations and dysfunction of DSG2 adversely affect cardiac function, leading to conditions such as arrhythmogenic right ventricular cardiomyopathy and dilated cardiomyopathy (53-55). DSG2 is also upregulated in several epithelial cancers, presumably as a means of ensuring a physical barrier capable of occluding therapeutics or immune cells.

1.6 Development of the Junction-Opener Protein

Among DSG2-targeting viruses is serotype 3 (Ad3). Ad3 is able to efficiently breach the epithelial barrier in the airway tract and infect airway epithelial cells. This is achieved by the binding of Ad3 to DSG2, and subsequent intracellular signaling that results in transient opening of tight junctions between epithelial cells. To capitalize on this mechanism, the knob protein was stripped down to a recombinant protein that contains the minimal structural domains from Ad3 that are required to open the intercellular junctions in epithelial tumors. As a group these proteins are called "junction openers" ("JO") (56-59). The protein is a self-multimerizing recombinant protein derived from the Ad3 fiber protein (59). The C-terminal fiber protein domain, the so-called fiber knob, was modified to increase its affinity to DSG2. JO can be easily produced as a functional protein from *E. coli* cultures and purified by affinity chromatography. JO binds with picomolar affinity to DSG2 and causes clustering of several DSG2 molecules on the cell membrane. Binding of JO to DSG2 activates mitogen-activated protein kinases (MAPKs), which in turn activate a matrix-metalloproteinase (ADAM17) in tumor cells. ADAM17 cleaves within the extracellular domain of DSG2 thereby breaking the DSG2 dimers that link two neighboring epithelial cells together, leading to junction opening (60). JO-triggered junction opening has been visualized by electron microscopy of epithelial cells. The cleaved extracellular domain of DSG2 is shed and can be measured in culture supernatant by ELISA. JO-mediated DSG2 shedding is also detected *in vitro* and *in vivo* in the serum of mice with established ovarian cancer xenograft

tumors (60). During adenovirus replication, viral protein complexes (PtDd) similar to JO are released from infected cells, open the junctions between neighboring cells and thus allow *de novo* produced virus to spread in epithelial tumors (61). This indicates that JO can facilitate its own tumor penetration in a positive feed-forward manner. Additionally, experiments in over 25 xenograft models that the intravenous injection of JO increased the efficacy of cancer therapies, including many different monoclonal antibodies and chemotherapy drugs, in a broad range of epithelial tumors (56, 57). Further studies have shown that the effective doses of chemotherapy can be reduced when the chemotherapy drugs are combined with JO. Furthermore, studies have demonstrated that combining JO with chemotherapy drugs markedly reduced the toxic side effects of chemotherapy in mouse tumor models (56). The application of JO was safe and well-tolerated in toxicology studies carried out in human DSG2-transgenic mice and macaques (57, 62, 63).

Preliminary research with JO has indicated an increased efficacy in combination with conventional therapeutics such as paclitaxel, the anti-Her2/neu trastuzumab, and pegylated liposomal doxorubicin (64) in multiple animal models of solid tumors. The combination of JO and the monoclonal antibodies resulted in slower tumor growth and safety has been demonstrated in non-human primates, with no major adverse effects or immunogenicity being noted (65).

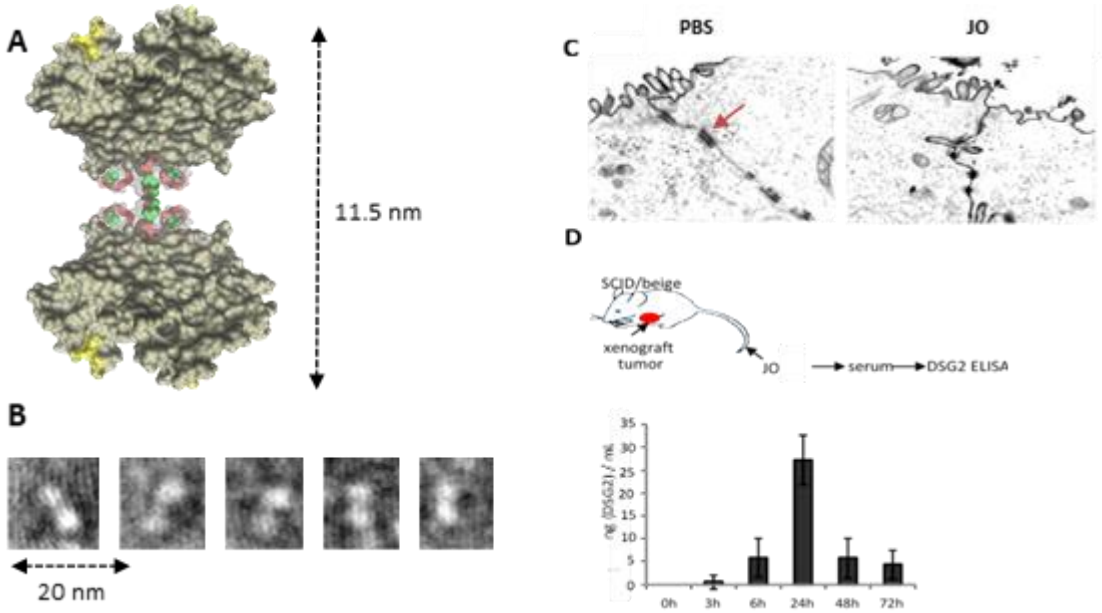

Figure 1-3 JO, a molecule that cleaves DSG2 and opens tight junctions.

A) Model structure of JOC trimers containing a cysteine for dimerization (green) on a flexible linker, one fiber shaft motif (red), and the affinity-enhanced (yellow surface) Ad3 fiber knob domain (tan surface). JO forms trimers which are then dimerized through the C-terminal cysteines. JO is produced from *E. coli* cultures and currently yields ~70mg/L. B) Electron micrograph of JO. The barbell structure the model predicts is seen in the micrograph and the distances correspond well to the model (black arrows in A and B). C) Transmission electron microscopy of junctional areas in polarized colon cancer T84 cells. Cells were either treated with PBS (left panel) or JO (right panel) for 1h on ice, washed, and then incubated for 1h at 37°C. The electron-dense dye ruthenium red (66) was then added together with the fixative. If tight junctions (above the desmosomes, marked by an arrow) are closed, the dye only stains the apical membrane (black line). If tight junctions are open, the dye penetrates between the cells and stains the basolateral membrane. Magnification is 40,000×. D) JO-mediated DSG2 shedding in mice with tumors derived from the human ovarian cancer cell line SKOV3. Immunodeficient CB17

SCID/beige mice with established subcutaneous SKOV3 tumors (~500mm^3) were injected intravenously with JO (2mg/kg). Pre-injection serum samples ("0h") and samples harvested 3, 6, 24, 48, and 72 hours after JO injection were analyzed by ELISA for DSG2 concentrations (N=5).

1.7 Ovarian Cancer Diagnostics and Biomarkers

Ovarian cancer diagnosis involves a combination of examinations and biomarker testing. As with most other cancers, a physical examination is the first step in confirming diagnosis. A pelvic or rectovaginal examination looks for ascites or enlarged masses indicative of a tumor. This is followed up by imaging with transvaginal ultrasound, computed tomography (CT) scanning, or magnetic resonance imaging (MRI) to ascertain the extent of the tumor and prepare for surgery if needed. Symptoms in ovarian cancer often manifest only in later stages (III/IV) and rarely therefore this malady is rarely diagnosed early (67). Tissue biopsies are also taken and inspected by pathologists to ascertain staging and cell origins (68). A definitive diagnosis requires surgical procedure into the abdominal cavity, and visual confirmation or removal of suspected tissue for histopathological analysis are carried out to confirm the presence of malignant tumor and its progression (69).

Biomarkers in ovarian cancer have a long history, with the first biomarker, carcinoembryonic antigen (CEA) approved specifically for ovarian cancer in 1976. Multiple serum biomarkers or panels followed: cancer antigen 125 (CA125, 1981), human epididymis protein (HE4, 2008), Ova1 (2009), ROMA (2010), and Overa (2016) (70). These biomarkers have become progressively more intricate, with the more recent approvals from the FDA involving a panel of protein screens and algorithms to ascertain likelihood of tumor presence. However, using these biomarkers as diagnostics independent of other methods remains difficult. CA125, the preeminent serum ovarian cancer marker, is about 50-60% sensitive; when combined

with HE4, this increases to 73%. The HE4+CA125 (the two protein panel ROMA) combination fares poorer with early detection, with a sensitivity of only 46% when detecting stage I ovarian cancer (71). Accordingly, these tests and panels cannot be used independently of other diagnostic mechanisms, and are primarily used as “triage” or “referral” tests, used only after a mass or tumor has been confirmed via surgery or imaging. Thus, the current use of biomarkers and molecular tests is relegated to auxiliary purposes.

Despite these diagnostic techniques being widely available in the developed world, only 31% of all ovarian cancers are diagnosed at earlier stages (I/II) and 60% at later stages (III/IV) in the United States, with the stage of diagnosis being a critical factor in a positive prognosis and survival (72). This highlights the dire need for diagnostics and biomarkers in ovarian cancer to ensure early diagnosis and longer survival.

1.8 Liposomal Doxorubicin in Ovarian Cancer, and its combination with JO

PEGylated liposomal doxorubicin (PLD) is a PEGylated, liposome-encapsulated form of doxorubicin. The effective size of the liposome is ~100nm. PLD has a central role in the treatment of ovarian cancer. PLD is an FDA approved for treatment of advanced ovarian cancer patients failing first line platinum therapy and is a preferred agent in this setting. When used as a monotherapy, objective response rates from 10%-26% have been reported (73-75). In a randomized phase III trial, PLD therapy demonstrated improved Progression-Free Survival (PFS) and Overall Survival (OS) compared with therapy using topotecan in patients with platinum sensitive disease (76). PLD has also been investigated in combination therapy with carboplatin. Results from the Phase III CALYPSO trial confirmed that carboplatin-PLD (CD) is non-inferior to carboplatin-paclitaxel (CP) in patients with platinum sensitive recurrent ovarian cancer. In the first line setting CD therapy achieves similar response rates, PFS and OS to CP

(77, 78). At the FDA-recommended dose of 50mg/m^2, monotherapy with PLD is associated with grade 3 or worse toxicity in 30% of patients with hand-foot syndrome and stomatitis / mucositis being the most common side effects. Doses must be reduced to as low as 30mg/m^2 in combination regimens which may be limiting efficacy.

Several lines of evidence suggest that PLD is an ideal agent for use in combination with JO. The large size of the PLD complex limits penetration of the drug into tumors. Studies using radio- or immuno-labeled liposomes in mouse xenograft tumor models demonstrate following extravasation from leaky tumor vessels that doxorubicin liposomes localize to the perivascular space and extra-cellular matrix (79, 80) with minimal tumor cell uptake (81). Unlike other chemotherapy drugs (*e.g.* camptothecins), doxorubicin does not form small metabolites that are capable of tumor penetration. Studies have confirmed poor intratumoral penetration of PLD in xenograft tumor models (56) and that when combined with JO, PLD tumor penetration is enhanced, toxicity is reduced, and efficacy is maintained at lower systemic doses of PLD. This raises the possibility that in addition to improving the anti-tumor effects of PLD monotherapy, JO co-therapy may also salvage the effectiveness of PLD in combination chemotherapy regimens for ovarian cancer where the PLD dose has to be reduced below the generally accepted effective dose of 40mg/m^2. Ovarian cancer cells surviving PLD therapy undergo a unique phenotypic transformation that includes upregulation of MHC-1 and Fas expression which increases the susceptibility of surviving tumor cells to immune mediated cell death (82). As demonstrated in preliminary work in ovarian cancer mouse models, JO reduces intra-tumoral regulatory T-cells and enhances anti-tumor CD8 T-cell response, properties which are likely to complement the phenotypic changes and enhance immune mediated death mechanisms for tumor cells surviving PLD therapy.

1.9 Dissertation Aims

This dissertation involves research investigating a combination of various interventions targeting ovarian cancers, with the potential to broadly address a variety of solid epithelial cancers. First, a novel protein biomarker of ovarian cancer, DSG2, is investigated for its association with survival and/or chemoresistance. A protein therapeutic which is transiently able to open tumor junctions and targets DSG2, the Junction-Opener protein has already been investigated thoroughly as a co-therapeutic administered in solid tumor models in combination with monoclonal antibodies and chemotherapeutics and presents a promising clinical candidate for ovarian cancer cases expressing high levels of DSG2. The dissertation explores the possibility of conjugating therapeutic payloads to the JO protein, to form a bioconjugate with the advantages of one-time administration, dose sparing, and decreased side effects. Finally, to investigate JO's suitability as a clinical candidate to move forward in humans, the research explores the pharmacokinetic, toxicology, and immunogenic profiles of JO and liposomal doxorubicin in rhesus macaques. Through this series of studies, the dissertation aims to explore the use of JO as an ovarian cancer targeting co-therapeutic and new modes of administration and use.

Chapter 2 USE OF DESMOGLEIN-2 AS AN OVARIAN CANCER BIOMARKER AND DIAGNOSTIC

This chapter has been submitted for publication in Cancer Biology and Therapy (2020).

2.1 Abstract

Greater than 80% of all cancer cases are carcinomas, formed by the malignant transformation of epithelial cells. One of the key features of epithelial tumors is the presence of intercellular junctions, which link cells to one another and act as barriers to the penetration of molecules.

Purpose: This study assessed the expression of desmoglein-2, an epithelial junction protein, as a prognostic and diagnostic biomarker for ovarian cancer.

Experimental Design: Ovarian cancer sections were stained for DSG2 and signal intensity was correlated to cancer type and grade. DSG2 immunohistochemistry signals and mRNA levels were analyzed in chemo-resistant and chemo-sensitive cases. Ovarian cancer patient serum levels of shed DSG2 were correlated to disease free and overall survival. Primary ovarian cancer cells were used to study DSG2 levels as they changed in response to cisplatin treatment.

Results: DSG2 expression was found to be positively correlated with cancer grade. Ovarian cancer patients with high serum levels of shed DSG2 fared significantly worse in both progression-free survival (median survival of 16 months vs. 26 months, $p=0.0023$) and general survival (median survival of 37 months vs. undefined, $p<0.0001$). A subgroup of primary chemotherapy resistant cases had stronger DSG2 IHC/Western signals and higher DSG2 mRNA levels. Furthermore, our *in vitro* studies indicate that non-cytotoxic doses of cisplatin can enhance DSG2 expression, which, in turn, can contribute to chemo-resistance.

Conclusions: We suggest that DSG2 can be used in stratifying patients, deciding on where to use aggressive treatment strategies, predicting chemoresistance, and as a companion diagnostic for treatments targeting DSG2.

2.2 Introduction

Although incidence rates of ovarian cancer have been falling over the last few decades, it still ranks as the most deadly of any cancer in the female reproductive tract. An estimated 22,530 new diagnoses and 13,980 deaths will occur in the United States in 2019(83), representing a significant burden in women's health. When diagnosed, the overall 5-year survival rate in the US is 45%. The main histological types of epithelial ovarian cancer are high-grade serous carcinoma (~70%), clear cell carcinoma (~10%), endometroid carcinoma (~10%), low-grade-serous carcinoma (<5%), and mucinous carcinoma (<5%). Disease stages are stage 1 (cancer is confined to one or both ovaries), stage 2 (cancer spreads within the pelvic region), stage 3 (cancer spreads to other body parts within the abdomen or retroperitoneal lymph nodes), and stage 4 (cancer spreads beyond the abdomen or directly involves the spleen).

A persistent problem in solid tumor therapy is the presence of physical barriers, which may act to prevent drug entry and penetration(84). Epithelial junctions are of particular interest in physical barrier formation, as the structure of a tight junction can exclude entry of molecules as small as 400 Daltons (85). These junctions are involved in the regulation of ion transport across epithelia, preservation of structural integrity and exclude entry of microbes, or - in the case of malignant tumors - therapeutics. Epithelial junctions include tight junctions, desmosomes, gap junctions, and adherens junctions. Tight junctions, also called zonula occludens, are often found in locations where impermeability of soluble molecules is required, such as in the gastro-intestinal or airway

tracts (86). Several pathogens subvert the tight junctions as means of entry, including enteropathogenic *E. coli*, and *Salmonella* (87). Several types of adenoviruses target multiple receptors involved in the formation of epithelial junctions including the CAR, the coxsackievirus receptor, and DSG2, the adenovirus receptor (62, 88).

DSG2 is a calcium-binding transmembrane glycoprotein belonging to the cadherin protein family. It is a key component of desmosomal junctions responsible for forming cell-to-cell junctions and as an anchor for intermediate filaments (89). It has been reported that epidermal growth factor receptor (EGFR) activation triggers tyrosine phosphorylation of DSG2 and subsequent modulation of cell-cell interaction, in part through the activation of matrix metalloprotease (MMP) cleavage of DSG2 homodimers between neighboring epithelial cells (90). This cleavage results in shedding of the extracellular domain of DSG2. In xenograft tumor models, shed DSG2 can be detected in the serum (91).

DSG2 has been observed to be overexpressed and predictor of poor prognosis in multiple types of cancer, including skin (92, 93), non-small cell lung cancer(94), lung adenocarcinoma(95, 96), hepatocellular carcinoma (97), and gastric cancer (98), indicating that tumors take advantage of DSG2 overexpression as a means of forming tight physical barriers and contributing to resistance against chemotherapeutics. This makes DSG2 an appealing target: compromising it in solid tumors would result in enhanced permeation or penetration of therapeutics and immune cells. We have previously explored this option using an engineered form of the adenovirus subtype 3 fiber knob protein, which mediates binding to the DSG2 protein, its cleavage/downregulation and transient opening of epithelial junctions (56, 57, 59, 62, 91, 99, 100).

In the context of ovarian cancer, several studies have found preliminary evidence of DSG2 overexpression. A proteome analysis of ovarian cancer ascites found DSG2 upregulated and suggested it as potential biomarker for ovarian cancer (101). mRNA profiling using the TCGA data set found that upregulated DSG2 expression correlated with worse high-grade serous ovarian cancer (HGSC) prognosis among platinum-sensitive patients (102).

Here we specifically investigated DSG2, including shed serum DSG2, as a potential ovarian cancer biomarker. We found significant correlation of DSG2 overexpression with shorter progression-free survival, overall survival, and chemoresistance. The outcome of this study is also relevant for an upcoming clinical trial: We have generated a small recombinant protein (JO) that binds to desmoglein 2 (DSG2), a junction protein that is overexpressed in ovarian cancer. Binding of JO to DSG2 triggers signaling pathways that result in the transient opening of tight junctions in epithelial tumors, including ovarian cancer xenografts (62, 91). The goal of our planned trial is the clinical translation of JO in combination with PEGylated liposomal doxorubicin (PLD) / Doxil® for ovarian cancer therapy (63). In this context, we plan to measure DSG2 levels in patient biopsies and serum and correlate these data with treatment outcome.

Our study is also relevant for DSG2 targeting oncolytic adenoviruses are being used clinically, including Ad5/3 and Ad3-based vectors (62, 103-105).

2.3 Methods and Materials

Cells: Ovc316 cells are primary ovarian cancer cells derived from a patient biopsy, specifically one of high-grade serous ovarian cancer(106). Work with patient derived tumors cells was approved by the Fred Hutchinson Cancer Research Center Institutional Review Board (protocol:

6289 “Secondary use of human cells”). Primary ovarian cancer cells were cultured in MEGM (MEBM containing 3µg/L hEGF, 5µg/L insulin, 5 mg/L hydrocortisone, 26 mg/L bovine pituitary extract, 25 mg/L amphotericin B) (Lonza, Basel, Switzerland), supplemented with 10% FBS (Gibco, Waltham, MA), 100 I.U. penicillin, 100mg/L streptomycin. Xenograft tumors were established by injection of $2x10^6$ ovc316 cells (1:1 with Matrigel) into the mammary fad pat on immunodeficient CB17 mice.

Immunohistochemistry staining for DSG2. Paraffin sections of ovarian biopsies were obtained from the Translational Outcomes Research (TOR) Repository, Fred Hutchinson Cancer Research Center. The ovarian tissue array was obtained from Biomax Inc (Rockville, MD, USA, Part Number OV208a). The array contains 207 core sections from 69 cases as well as information on TNM, clinical stage and pathology grade as classified according to WHO 1999 Classifications by a certified pathologist. Slides were deparaffinized and hydrated through immersion in xylene, decreasing concentrations of ethanol (100%-95%-80%-70%), and water. Slides were then immersed in 0.3% hydrogen peroxide, followed by an additional rinse of water to eliminate endogenous peroxidase. Slides were then placed in 1% Unmasking solution (Vector Labs, Burlingame, CA) and placed in a miniature autoclave (at up to 125°C for 1 hour) for antigen retrieval. Slides were incubated in 2.5% normal horse serum (NHS) blocking solution (Vector Labs, Burlingame, CA) for 20 minutes at room temperature, followed by incubation with the primary antibody (goat anti-human DSG2, Abcam, Cambridge, UK) (diluted 1:200 in PBS/1% NHS) overnight at 4°C. Following an additional wash in PBS, 4 drops of ImmPRESS Reagent Kit anti-goat Ig (Vector Labs, Burlingame, CA) were added and slides were incubated for 30min. After washing, 2 drops of Polink-2 HRP Kit with DAB Chromogen (Golden Bridge International, Inc)

were added and allowed to develop for around 5 minutes before washing with water. Sections were counterstained with Mayer's Hematoxylin (Sigma-Aldrich, St. Louis, MO) for 5 to 10 seconds and washed with water. After the slides dried, 3-5 drops of VectaMount (Vector Labs, Burlingame, CA) were added to the slide with a cover slip placed on top. Images were taken with a Leica DMLB microscope (Wetzlar, Germany), using Leica DFC300 FX Digital camera and Leica Application Suite Version 2.4.1 R1 software.

For quantitation, tissue microarray slides were scanned in brightfield with a 20× objective using a NanoZoomer Digital Pathology System (Hamamatsu City, Japan). The digital image was then imported into Visiopharm software (Hoersholm, Denmark) for analysis. Using the Visiopharm Image Analysis module, regions of interests (ROI) were manually drawn around each tissue core. By converting the initial digital image into grayscale values using two features, RGB - B and RGB – R, the Visiopharm software was trained to label positive staining, DSG2, and background tissue counterstain, hematoxylin, using a project specific configuration based on a threshold of pixel values based on the difference in intensity between normal tissue and cancerous tissue. ROIs were manually designated to exclude non-epithelial tissue. The ROIs were processed in batch mode using this configuration to generate the desired per area outputs and analyzed at 100%.

DSG2 Immunofluorescence staining on sections of ovc316 xenograft tumors. Cryosections of xenograft tumors were fixed in 4% paraformaldehyde for 15 minutes at room temperature then rinsed with PBS three times. The slide was then placed in blocking buffer (2% non-fat milk in PBS) for 60 minutes at room temperature. Primary antibodies mouse anti-DSG2 (6D8, Abcam, UK) and rabbit anti-Claudin7 (ab27487, Abcam, UK) were prepared at a 1:50 dilution. Blocking

solution was removed and slides were incubated with primary antibody overnight at 4°C. After washing, slides were incubated with the secondary antibody mix (FITC-goat-anti-mouse Ab, PE-goat-anti-rabbit Ab) for 1 hour at room temperature in the dark. Slides were washed with PBS before mounting with Vectashield Antifade Mounting Medium + DAPI (Vector Labs, Burlingame, CA) and were viewed under a Leica microscope as described above.

Western Blot. Mini-PROTEAN precast gels (BIO-RAD, Hercules, CA) with 4-15% gradient polyacrylamide were used. A total of 1 µg protein diluted 1:1 in 2 × loading buffer (10 mM Tris-HCl, pH = 6.8, 200 mM DTT, 4% SDS, 20% glycerol, 0.2% bromophenol blue) was loaded per lane. Samples were boiled for 5 min. The following running buffer was used: 25mM Tris, pH = 8.3, 0.192 M glycine, 0.1% SDS. After electrophoresis, proteins were transferred to nitrocellulose and incubated with the anti-DSG2 antibody 6D8 as described previously and a secondary anti-mouse IgG HRP conjugate (62). Selected Western blots were scanned and quantified using the ImageJ 1.32 software (National Institutes of Health, Bethesda, MD).

DSG2 ELISA. **The** ELISA was performed using a rabbit polyclonal anti-human desmoglein-2 antibody (R&D System, Catalog # AF947) as a capture antibody at a concentration of 2µg/ml in 0.1 M Na-carbonate, pH = 9.6 buffer. Plates were washed with TBS-T (Tris-buffered saline + 0.05% Tween-20) before blocking with Starting Block™ (PBS) Blocking Buffer (Thermo Scientific, Prod #37538). For detection, the mouse monoclonal antibody 6D8 directed against ECD3 (AbD Serotec, Raleigh, NC) was used at a 1:100 dilution. After three washes, goat anti-mouse IgG-HRP peroxidase (BD Pharmingen, San Jose, CA) was added at a 1:1000 dilution in blocking buffer. 1-Step™ Ultra TMB-ELISA (Thermo Scientific) was used as substrate.

Recombinant human DSG2 protein used for the standard curve was from Leinco Technologies, Inc. (St. Louis, MO). The detection limit of the DSG2 ELISA was 0.5 ng/ml.

mRNA quantification. Clinical biopsy samples from ovarian cancer patients were used for RNAseq. RNA was extracted from samples using RNeasy Plus Mini or AllPrep RNA/DNA kits (QIAGEN). The quality of the RNA was assessed on an Agilent 2100 Bioanalyzer. Samples with RNA integrity number (RIN) greater than 7 were diluted to 50 ng/mL for sequencing library preparation using TruSeq Sample Preparation Kit (Illumina, CA). Starting with approximately 1 µg of total RNA, mRNA was isolated with oligo-dT capture beads, then fragmented and converted to cDNA with random hexamer-primed reverse transcription and second-strand synthesis. Resulting cDNAs were fragmented by sonication and size-selected for molecules of ~300 bp. Ligation of barcoded sequencing adapters was then performed according to manufacturer's recommendations. The cDNA samples underwent multiplex sequencing, with one to four samples per lane, on the Illumina HiSeq 2000 to yield 50 bp paired-end sequences. This process yielded between 54.6 M and 367.0 M sequences passing the default Illumina quality control filters. RNA-seq data analysis was performed as described elsewhere (107).

Clinical Samples and Statistical Analyses. Ovarian cancer biopsies and sections were provided by the Pacific Ovarian Cancer Research Consortium (POCRC) Specimen Repository without any confidential information which would serve to identify a patient (Fred Hutchinson Cancer Research Center, IRB protocol # 6289). Statistical analyses were carried out using Graphpad Prism (San Diego, CA, USA).

2.4 Results

DSG2 is overexpressed in ovarian cancer primary and metastatic tissue. A series of ovarian cancer tissue slides were stained for DSG2. Ovarian primary cancer tissue of serous, clear cell, and endometroid origin showed localization of the highest DSG2 expression at the cell-cell junctions, as expected, although a scattered distribution of DSG2 staining was present along the cell membrane (Figures 2-1 and 2-S1). Metastatic tissue showed similar expression patterns toward the periphery of the lesion with relatively more uniform distribution throughout the core of the tumor (Figure 2-1B). Immunofluorescent staining of an ovarian cancer primary cell line, ovc316, showed abundant levels of DSG2 at the edges of the tissue co-localizing with claudin-7, another key junction protein (Figure 2-1C). This indicated that ovarian cancer tissue of primary, metastatic, and cell line origins have irregular expression where DSG2 is not exclusively trapped in junctions and accessible to potential ligands.

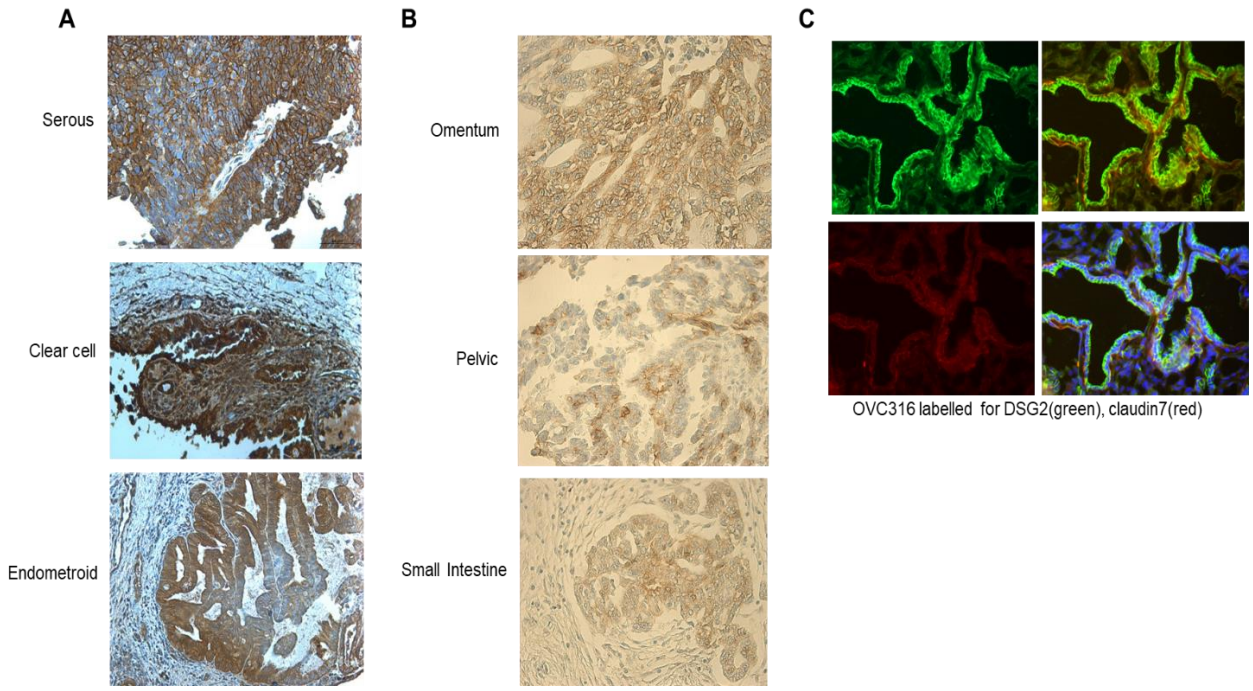

Figure 2-1 DSG2 is differentially expressed in ovarian primary, metastatic tumors and cell lines.

A) Representative clinical samples of serous (n=21), clear cell (n=11), and endometroid tumors (n=10). Paraffin sections were stained for DSG2 (brown) and counterstained with hematoxylin/eosin. **B)** Representative clinical samples of metastases at the omentum (n=12), pelvis (n=7), and small intestine (n=4) of ovarian origin stained for DSG2 with hematoxylin/eosin counterstain. **C)** Xenograft tumor derived from injected ovc316 cells, a primary ovarian cancer cell line. Cryosections were stained for DSG2 and claudin7 with secondary antibodies conjugated to FITC (DSG2-green) or PE (claudin 7-red). Cell nuclei were stained with DAPI (blue).

DSG2 is differentially expressed by class and grade of ovarian cancer. To obtain more quantitative data, an ovarian cancer tissue array was stained for DSG2 using identical antibodies to those used for the clinical samples above. The tissue array contained a variety of ovarian cancer tissues ranging in grades from 1 to 3, and classified as mucinous, serous, metastatic, or normal (See Supplementary Table 1 for patient information). Initial DSG2 staining showed progressive increases in DSG2 staining intensity with higher grades, seen throughout the entire section with concentration near cell-cell junctions (Figure 2-2A). Analysis of DSG2 signals using Visiopharm software allowed for estimation of the ratio of $DSG2^+$ regions (as defined by a threshold of pixel intensity values) compared to total area of the tissue section. Using this measure, a comparison of $DSG2^+$ ratios between grades found significant differences between normal non-malignant tissues, grade 1, and grade 2 tissues, and a trend between grades 2 and 3 (Figure 2-2B). A linear regression using the histopathological grading resulted in significance differences associated with grades 2 and 3 when compared to normal tissue (Figure 2-2D). Strikingly, when grade 1 alone was compared to grades 2+3 together, mean DSG2+ ratios were 0.199 and 0.451 respectively ($p<0.0001$). When analyzed by histological subtype or location (primary vs metastatic), serous ovarian cancer showed the highest DSG2 staining, followed by mucinous and metastatic tissues (Figure 2-2C). All cancerous tissue, including metastatic lesions still showed elevated DSG2 staining in comparison to normal tissue. Thus, DSG2 is increasingly expressed on higher grade ovarian cancers and is differentially expressed in varied presentations of ovarian cancer.

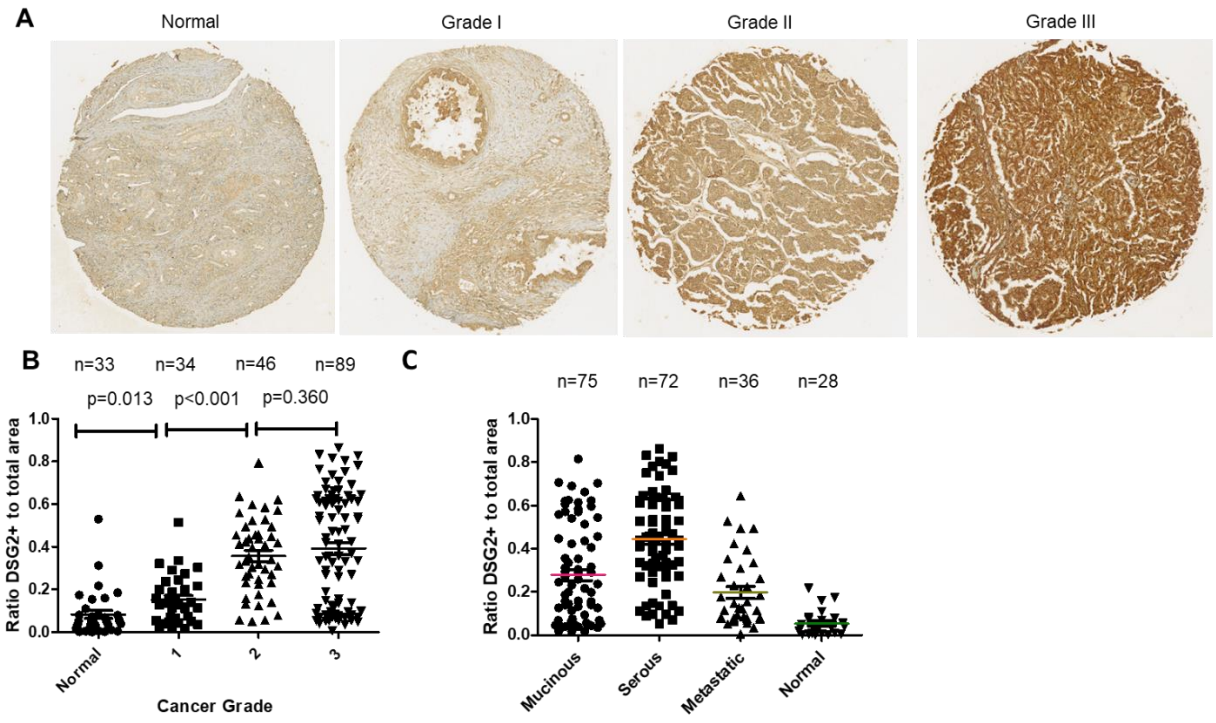

D

	Coefficient	P-value
Intercept	0.0830	0.0204
Grade 1	0.0694	0.1660
Grade 2	0.2739	1.71×10^{-8}
Grade 3	0.3087	3.37×10^{-12}

Figure 2-2 DSG2 is differentially expressed in ovarian cancers by grade and pathologic classification (localization).

Commercially available ovarian cancer tissue panels were stained for DSG2 and analyzed for staining intensity. **A)** Representative DSG2 stains of different ovarian cancer tissue classified by grade, from normal to grade 3 (40× magnification). **B)** Representative DSG2 stains of different ovarian tissues classified by grade, from normal tissue (not malignant or benign) to cancerous grades 1-3 (20× magnification). DSG2 staining intensity was quantified using Visiopharm software, with analysis parameters outlined in the Materials and Methods Section. *P* values

represent statistical significance determined with pairwise comparisons using the Student's t-test. Error bars indicate 95% confidence intervals. **C)** Numerical comparison of DSG2 signals by histological classification. "mucinous": mucinous primary tumor; "serous": serous primary tumor; "Metastases": metastatic lesion derived from serous ovarian cancer. Error bars indicate 95% confidence intervals. **D)** Coefficient and *P* values for linear regression modelling of DSG2+ ratio by grade, using normal grade as base. Coefficient and *P* value with null hypothesis of coefficient = 0 is shown.

DSG2 is differentially expressed in chemo-resistant relative vs chemo-sensitive ovarian cancer. Considering the fact that epithelial junctions represent physical barriers to intratumoral penetration of chemotherapeutic drugs, we hypothesized that DSG2 expression and presence in epithelial junctions would correlate with resistance to chemotherapy. We therefore focused on ovarian cancer biopsies from patients that were classified as chemo-resistant and chemo-sensitive. Chemo-resistant cases were defined as follows: *i)* progression through or persistence at completion of primary chemotherapy and *ii)* complete response to primary platinum combination chemotherapy but disease recurrence within 6 months. Chemo-sensitive cases were defined as patients with complete response to primary chemotherapy and a progression-free interval (PFI) of at least 24 months (108).

Staining of DSG2 on chemo-resistant ovarian cancer sections demonstrated stronger DSG2 signals in the cell membranes (Fig. 2-3A, left panels). In contrast, DSG2 staining was less membrane-localized on chemo-sensitive cases (Fig. 2-3A right panels).

In another set of ovarian cancer biopsy samples (25 chemo-resistant and 24 chemo-sensitive cases), we measured DSG2 mRNA by RNA-Seq. Samples from chemo-resistant patients showed significantly higher reads of DSG2 mRNA when compared to chemo-sensitive cases (Fig. 2-3B). Interestingly, even within the chemo-resistant DSG2-high population a clustering of two distinct populations occurred, indicating high DSG2 expression as a partially associated, but not solely responsible factor with chemo-resistance. A similar expression pattern was observed by Western blot analysis of ovarian cancer lysates using DSG2 specific antibodies (Fig. 2-3C).

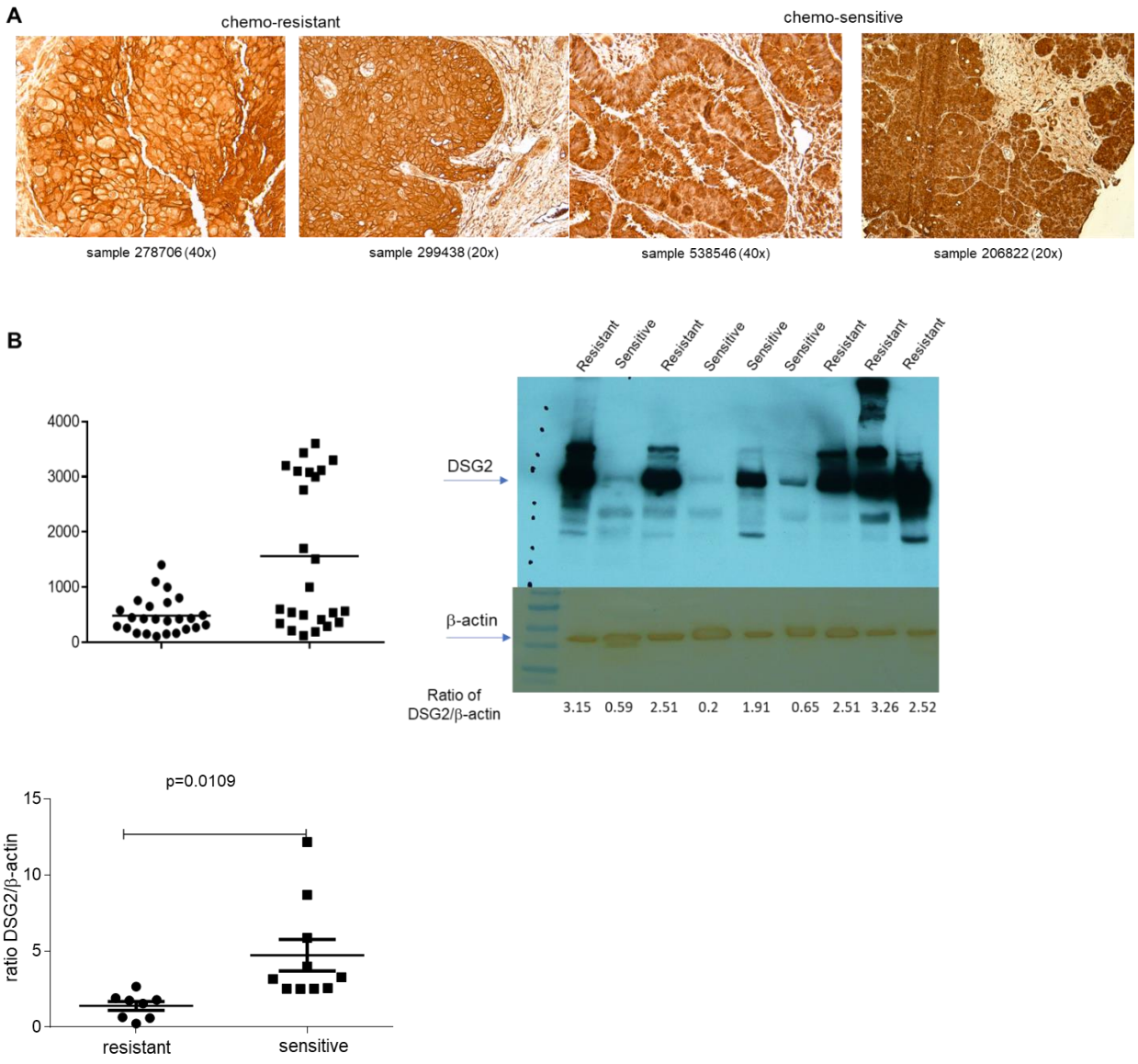

Figure 2-3 DSG2 expression in chemo-resistant and chemo-sensitive tumors.

A) Representative tumor sections from patients classified as chemo-resistant or chemo-sensitive were stained for DSG2 (brown). **B)** DSG2 mRNA levels in cohorts of chemo-sensitive and chemo-resistant ovarian cancer patients (n=49). Shown are DSG2 mRNA reads as detected by RNAseq. **C)** DSG2 Western blot of biopsy lysates from chemo-resistant or chemo-sensitive patients. Right panel: A set of representative samples are shown. Left panel: Normalized DSG2 Western blot signals. Each symbol represents an individual patient.

Serum DSG2 levels are associated with ovarian cancer survival. To further explore the differential DSG2 expression in ovarian cancer patients, we measured shed DSG2 in serum samples of 23 patients with advanced stage ovarian/fallopian tube cancer (109). Blood was drawn after front line surgery and chemotherapy treatment and at 3 months intervals thereafter. Twenty patients developed recurrent disease and were used for marker evaluation. All patients received six cycles of a carboplatin-taxane combination therapy. Patients were classified as DSG2-high (>828 ng/ml of DSG2) or DSG2-low (<828 ng/ml). The DSG2 threshold reflected the mean DSG2 concentration of the cohort.

DSG2-high patients had a significantly shorter progression free survival ($p=0.0096$) and overall survival ($p=0.0003$) (Figure 2-4). The average time until progression was markedly different in the groups, with the DSG2-high population averaging a progression-free survival (PFS) of only 16 months vs 26 months in the DSG2-low population. The drastic difference in survival and progression in ovarian cancer patients may highlight the importance of DSG2 in mediating chemoresistance and faster progression and the potential of DSG2 to be used as a prognostic marker to predict patient outcomes.

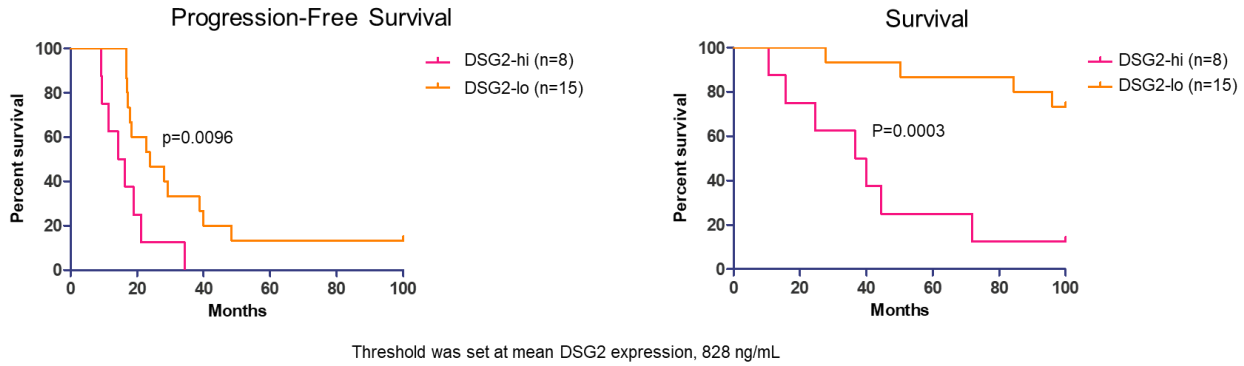

Figure 2-4 DSG2 expression correlates with ovarian cancer progression-free survival (PFS) and general survival.

A cohort of ovarian cancer patients from the Fred Hutchinson Cancer Center were placed into DSG-high or DSG-low expressing groups as defined by a threshold mean serum DSG2 concentration of 828 ng/mL, Analyses were done for months of PFS and general survival, using the Log-Rank (Mantel-Cox) tests for comparisons between populations. *P* values are results of the Log-Rank test for comparison of survival between populations

DSG2 levels increase in tumor cells treated with chemotherapy. The most probable explanation for the upregulation of DSG2 in cancers is to enforce the epithelial barriers which preclude entry of chemotherapeutics. This could be a process that is triggered in cells that were exposed to non-cytotoxic doses of chemotherapeutic drugs, e.g. tumor cells distant to blood vessels (23, 24). To support this hypothesis, we exposed primary ovarian cancer cells (ovc316) to cisplatin at a non-cytotoxic dose (2.5µM (110)) for six days (Figure 2-5). Starting from day 2, significantly more full-length and cleaved DSG2 was detected by Western blot in samples treated with cisplatin compared to mock-treated samples. At day 6, the differences between the two settings was greater than 10-fold. These results indicate that DSG2 is upregulated in response to cisplatin treatment, which may represent an autocatalytic mechanism to initiate or enhance chemo-resistance. Clearly, this finding has to be validated using clinical samples and animal models, including human-DSG2 transgenic mice with syngeneic tumors (58, 91). Again, considering the higher mutation rate and genomic instability higher in high-grade serous ovarian cancer, chemotherapy might select for tumor cell clones with higher DSG2 expression (111).

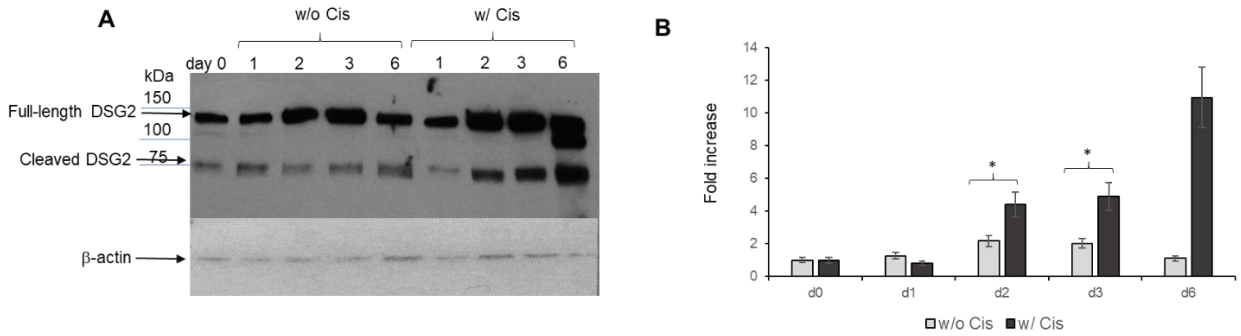

Figure 2-5 DSG2 expression in a primary ovarian cancer cell line (ovc316) is upregulated in response to cisplatin.

A) Ovc316 cells were cultured with or without cisplatin added to medium. Cells were harvested before adding cisplatin ("day 0") and at days, 1, 2, 3, and 6 in the absence or presence of 2µM cisplatin. Cell lysates were analyzed by Western Blot. The full-size DSG2 band at around 120-130 kDa and the cleaved extracellular domain (~80kDa) are indicated. The right panel shows normalized DSG2 Western blot signals. The average of both experiments is shown as fold increase over pre-treatment ("day 0") levels.

2.5 Discussion

While over 80% of advanced stage ovarian epithelial cancer patients attain clinical remission with standard platinum/paclitaxel-based chemotherapy, the vast majority of them will relapse within two to five years (112, 113). It has become standard clinical practice to include CA125 testing in patient surveillance. Elevation in CA125 often precedes clinical evidence of relapse by imaging or physical exam (114). Data from a large randomized clinical trial, however, demonstrate no survival advantage from CA125 screening (115).

HE4 can predict ovarian cancer recurrence earlier than CA125 and it can be elevated in patients that do not express CA125 at sufficient levels to make a clinical decision (109).

Our findings that DSG2 is upregulated in ovarian cancer are in line with reports on other cancers. Proteomics analysis of ascites from ovarian cancer patients identified DSG2 as one of the top hits of upregulated proteins (101). Moreover, survival of HCC patients with high DSG2 mRNA and protein expression was shorter (97). However, there are studies with melanoma, pancreatic, and colon cancer cell lines and xenograft tumor models indicating enhanced metastasis and aggressiveness upon suppression or loss of DSG2 expression (97, 116, 117). Furthermore, low DSG2 expression has been associated with poor clinical outcomes in certain types of cancer such as prostate (49) and gastric (118) cancers. This was explained by the observation that loss of epithelial junctions and downregulation of epithelial proteins such as DSG2 is associated with epithelial-to-mesenchymal transition (EMT), a central mechanism for cancer cell mobility and metastasis (119). However, this assumption does not consider that following invasion or metastasis, cells that have undergone the process of EMT can also revert to a well-differentiated epithelial phenotype (28). In support, there exist numerous examples of advanced carcinomas

showing that mesenchymal cells can regain characteristics of epithelial cells or undergo mesenchymal to epithelial transition (MET) (28). Of note, a DSG2-targeting therapeutic which triggers DSG2 shedding, the junction-opener protein, does not enhance metastasis in cancer models (64).

Our study indicates DSG2 can be used as a potential biomarker for ovarian cancer that correlates with grade, chemoresistance, progression-free survival, and general survival. The observation of progressively higher DSG2 expression with higher cancer grade classification was notable, although the differences between grades 2 and 3 did not reach statistical significance. Particularly striking was the difference in PFS and general survival between DSG2-low and DSG2-high expressing populations, seen in two separate cohorts which lends further credence to the use of DSG2 expression levels as a prognostic indicator for ovarian cancer patients' survival.

While our finding might help to better understand mechanistic aspects of chemoresistance, they have direct practical implication for our upcoming clinical trial with our recombinant junction opener JO in combination with Doxil® in patients with progressive, persistent or recurrent ovarian/fallopian tube cancer, who have previously received standard therapies. DSG2 as a tumor marker and target also holds implications for oncolytic adenovirus therapy, and indeed Ad5/3 oncolytic constructs show increased efficacy on ovarian cancer cells with increased DSG2 RNA expression (120, 121).

Based on the data reported here we suggest that DSG2 may be useful in stratifying ovarian cancer patients, predicting chemoresistance, and as a companion diagnostic for treatments targeting DSG2.

We intend to investigate the role of DSG2 in other tumors – especially difficult to treat cancers like pancreatic cancer.

2.6 Acknowledgements

Peter Beidler assisted with histopathological tissue processing and staining. University of Washington Pathology assisted with setting up the software for quantitating DSG2+ areas. Cohort and survival data were provided by the Fred Hutch, Human Biology Division.

2.7 Supplemental Figures

Supplementary Table 1. Patient information of samples in the ovarian cancer tissue array. Patient information of tumor section arrays, for a total of 69 patients. Classified by type and histopathological staging.

Characteristic	Number
Case	
Mucinous	25
Serous	23
Metastatic	12
Normal	9
Stage	
I	28
II	8
III	10
IV	2
Average Age	47.5

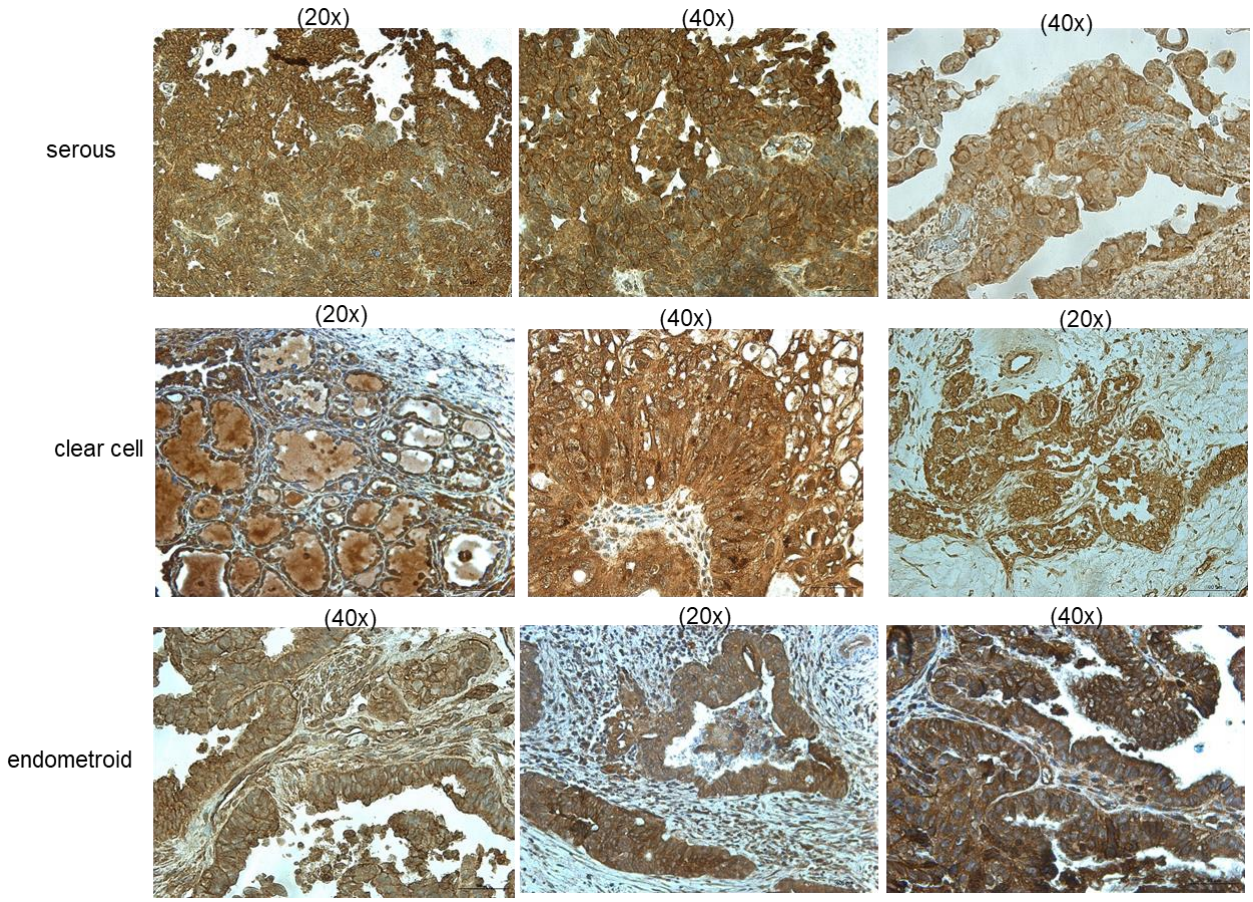

Figure 2-S1. Additional clinical samples of serous, clear cell, and endometroid tumors.

Paraffin sections were stained for DSG2 (brown) and counterstained with hematoxylin/eosin. Magnification is indicated above the photos.

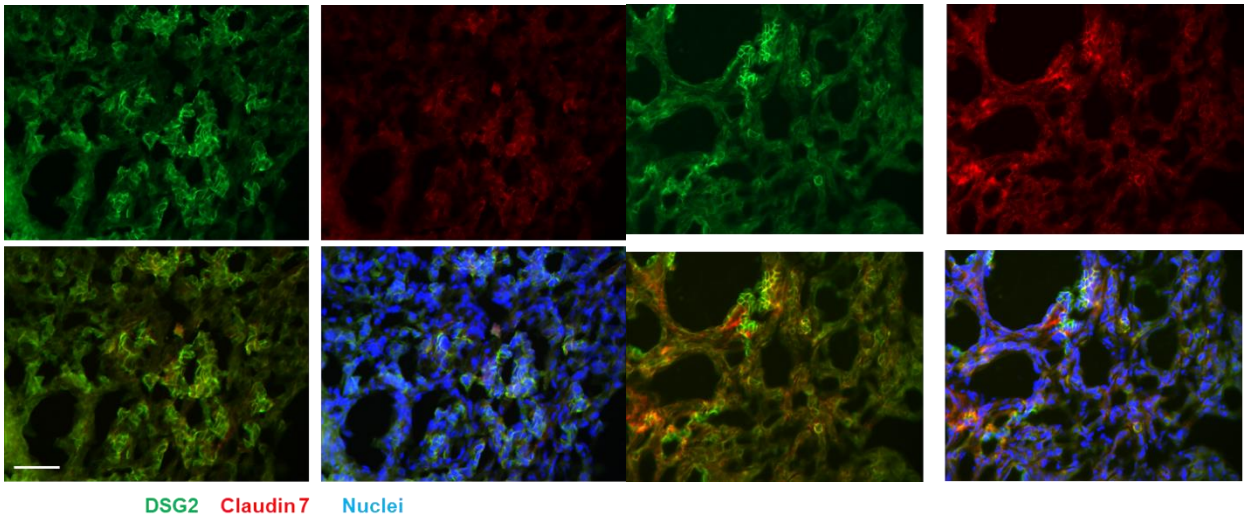

Figure 2-S2. Cryosections from xenograft tumor derived from injected ovc316 cells. Ovc316 cells were injected into the mammary fat pad. Tumors were harvested when they reached 500mm^3 and cryo-sectioned. Sections were stained for DSG2 and claudin7 with secondary antibodies conjugated to FITC (DSG2-green) or PE (claudin7-red). Cell nuclei were stained with DAPI (blue). The scale bar is 20mm.

Chapter 3 DEVELOPMENT AND OPTIMIZATION OF A CONJUGABLE FORM OF THE JUNCTION-OPENER PROTEIN

The content of this chapter is modified from J. Kim et al., "Structure-based Design of JOC-x, a Conjugatable Tumor Tight Junction Opener to Enhance Cancer Therapy", published in Scientific Reports 2020.

3.1 Abstract

Disorganized intercellular junctions are critical for maintaining the integrity of solid epithelial tumors and prevent the infiltration of oncological therapies into the bulk of the malignancy. We have developed small, recombinant proteins which bind a critical junction protein, desmoglein 2, triggering the transient and specific opening of tumor tight junctions allowing for infiltration of the tumor with immune cells, oncolytic viruses, drugs, and other therapeutics. Our new molecule, JOC-x, is a promising candidate for a new class of tumor-targeting agents that accumulate both around and within tumors and remodel the tumor microenvironment. Native cysteines were removed from the parental protein, JO-4, followed by addition of a single cysteine to allow for convenient attachment of various payloads that can be targeted directly to the tumor. Our tumor-targeting protein exhibits high avidity, minimal aggregation, and is easily purified at good yields from E. coli. For proof of concept, we demonstrate effective conjugation to biotin as a model for flexible co-targeting, addition of metal ion chelators as models for imaging and radiotherapy, and linkage of the TLR3 agonist poly(I:C) as a model immune-oncologic agent. This second-generation cancer co-therapeutic protein is optimized for activity and primed for cGMP manufacture in preparation for upcoming clinical studies.

3.2 Introduction

There are physical barriers to tumor penetration by cancer drugs. One of the key features of epithelial tumors is the presence of intercellular junctions that link cells to one another and act as barriers to the penetration of molecules with molecular masses greater than four hundred Daltons (122-124). Several studies have shown that up-regulation of epithelial junction proteins correlate with increased resistance to treatment - including with therapies using monoclonal antibodies and chemotherapeutics (25-27). One of these junction proteins, desmoglein 2 (DSG2), is a membrane glycoprotein which participates in the formation of tight junctions. Many epithelial cancers are known to highly upregulate the production of DSG2 resulting in formation of a network of cellular "staples" reminiscent of poorly organized junctions that render the tumors resistant to permeation by immune cells and cancer treatments. Higher levels of DSG2 were found in all of the 60 primary and metastatic breast cancer biopsies analyzed (56). Moreover, mRNA profiling of ovarian cancer biopsies revealed overexpression of *dsg2* message in at least 50 samples analyzed (data not shown). It is thought that the epithelial phenotype of cancer cells and their ability to form physical barriers provides protection from the host immune system and/or elimination by cancer therapeutics (28).

Junction Opener 1 (JO-1) is a protein that binds to DSG2 and preferentially opens tumor tight junctions (56) (Figure 1). JO-1 was derived from the C-terminal knob domain of protein fibers on Adenovirus serotype 3 (Ad3) capsids, which in nature mediates binding of the virus to DSG2 within the tight junctions. Ad3 binding to DSG2 initiates a cascade of events within the host cell leading to DSG2 shedding and eventual opening of tight junctions, thus allowing for translocation of the virus between epithelial cells through the basolateral intercellular space (61). This phenomenon of opening tight junctions provided the basis for developing a co-therapeutic

protein to enhance entry of biologics and chemotherapeutic agents such as Doxorubicin, Abraxane, or Irinotecan into tumors. In healthy cells, DSG2 is sequestered to the lateral cell junctions and is minimally available for binding. However, depolarization of tumor cells during epithelial to mesenchymal transition (EMT) coupled with increased DSG2 expression provide an attractive target for our junction openers.

Early attempts at exploiting this property of Ad3 included recombinant expression of the fiber knob domains responsible for DSG2 binding. However, these proteins did not produce the desired tight-junction opening effects possibly due to inability of the knob protein to form active higher-order quaternary structures (59, 125). To overcome this obstacle, a dimerization domain (DD) was added to facilitate multimerization (59). This domain, a K-coil, is comprised of 5 repeats of 7 amino acids (shown in blue in Fig. 1a). Upon addition of the DD to the knob protein derived from Ad3, the resulting recombinant protein (JO-1) was able to form multimers, bind DSG2 *in vitro*, and inhibit Ad3 virus entry into HeLa cells. The JO-1 protein has since been extensively characterized, including the solved crystal structure of the active trimer (Figures 1b and 1c). The trimeric form of the protein is the minimal conformation which will bind DSG2, although with low affinity (125). However, for junction-opening activity, higher-order multimers are required, including the trimer-dimer, which has been described as a barbell structure (59, 125).

Mutagenic libraries of Ad3 fiber knobs identified a panel of mutations conferring higher affinities to DSG2 and enhancing viral inhibition in a functional assay (125). DSG2 binding by select mutants was measured by surface plasmon resonance (SPR) to determine if the affinity increase was due to faster association rates or more stable dissociation rates. One mutation, substituting the native valine to an aspartic acid at position 239 (V239D), resulted in a nearly

1000-fold increase in affinity as measured by a shift of the dissociation constant (K_D) from 10.8 μM for the original JO-1 to 11.4 nM for the V239D mutant (designated JO-4) (125). The JO-4 V239D mutation is localized to a region of the knob corresponding to a prominent loop (E-G) known to be critical for stabilizing DSG2 binding (indicated with red arrows in Fig. 1c). An additional eight Ad3 fiber knob mutations in three key regions (C-D loop, F-G loop, and H-I loop) were identified that reduced or ablated DSG2 binding (125). In this study, we focused on one of these mutations, E299V, which is localized to the H-I loop region and was shown to reduce DSG2 binding in the mutant by 80% (125).

Preliminary studies in mice have shown these junction openers to be effective at enhancing cancer therapy and very well tolerated even at high doses in non-human primates (NHPs) (63). The promising *in vivo* data has resulted in an application as an investigative new drug (IND) for co-therapeutic treatment of certain types of tumors (63). While co-administration of the JO-4 and effector molecules is an attractive model with substantial scientific support, the ability to produce a conjugatable junction opener with a specific site for covalent attachment to effector molecules would confer further production and deployment advantages. We envision that tumor targeting and effector-coupling with the new designer junction openers would enable nanoparticle delivery, targeting to DSG2 positive cancers, and chimeric antigen receptor (CAR) T-cell targeting. The depolarized nature during EMT and upregulation in DSG2 expression in tumors relative to normal tissues makes for an attractive target for our designer junction openers.

Our lead JO-4 derivative, termed JOC-*x* (for Junction Opener Conjugated to *x*), could be directly attached to effector molecules capable of imaging tumors, such as Europium, or further conjugated with radionuclides for direct ionization of the tumor microenvironment. We investigated direct conjugation of polyriboinosinic:polyribocytidylic acid “poly(I:C)” to JOC-*x*

for targeting and activating TLR3 and MDA5 receptors. By targeting poly(I:C) directly to the tumor-resident dendritic cells (DC), we would mimic natural infection by dsRNA viruses and initiate a robust inflammatory response typified by recruitment and activation of CD8+ T cells. Activation of TLR3 on tumor cells can also lead to tumor killing by initiating apoptosis, as has been demonstrated with the HPV vaccines BiVax and TriVax (126, 127). Moreover, numerous cancers are characterized by upregulation of TLR3, a receptor for poly(I:C), and in most of these cancers this TLR3 positivity is predictive of a favorable outcome if poly(I:C) is used as an immune therapeutic (126-131). Given the ability of JOC-*x* to specifically localize to tumors overexpressing DSG2, and the known anti-tumor effects of poly(I:C), we envision that the JOC-poly(I:C) conjugate would exhibit enhanced targeting of tumors, increased potency, and overall less toxicity due to reduced binding to healthy tissues expressing TLR3 receptors.

We report here development, characterization, and *in vitro* validation of a new junction opening molecule, JOC-*x*. Preliminary characterization of JOC-*x* reveals many attractive features for production, manufacture, co-administration, and conjugated targeting making it a promising candidate to move towards human trials.

3.3 Materials and Methods

Cloning and production of JO-1 derivatives. All genes used for this study were designed *in silico* using the software Serial Cloner v2.4.1. First generation JO derivatives, designated GB1-10, were based on the original JO-1 sequence as described previously (56, 57). The plasmid pET29a (Novagen) was linearized for Gibson cloning using outward facing primers pET29a_GB_UB (5'-TCCTCTCATATGTATATCTCCTTC) and pET29_GB_DT (5'-CTTAATTAGCTGAAATCACTAGT) using a 1/10000 dilution of plasmid as template in the PCR reaction. GB sequences were appended with nucleotides corresponding to the overlap

regions of pET29a entry vector and were synthesized as gBlocks™ by Integrated DNA Technologies (Coralville, IA). Gibson cloning of gBlocks into the pET29a entry vector was performed using the Gibson Cloning Master Mix (New England Biolabs, Ipswich, MA) per manufacturer's instructions. Cloned GBs were sequence confirmed (Genewiz, South Plainfield, NJ) and produced in *E. coli* Rosetta BL21 (DE3) (EMD Millipore, Darmstadt, Germany).

rhDSG2 binding Western blot. One microgram of junction opener proteins or derivatives were resolved by non-reduced and non-boiled SDS-PAGE using 4-20% Tris-glycine gradient gels. Proteins were transferred to a polyvinylidene fluoride (PVDF) membrane and blocked with blocking buffer [1× TBS supplemented with 0.05% Tween-20 (TBST) and 10% nonfat dry milk (NFDM)] for 2h at RT. Membranes were incubated with a 0.75 µg/mL solution of rhDSG2 (Leinco Technologies, Inc., Fenton, MO) in blocking buffer for 1h at RT. Following three 10 min washes with TBST, the membrane was incubated with a 1/2000 dilution of murine anti-human DSG2 monoclonal Antibody 6D8 (Bio-Rad, Hercules, CA) in blocking buffer for 1 hr at RT. For detection, the membrane was incubated with a 1/2000 dilution of goat-anti-mouse conjugated to horseradish peroxidase (Southern Biotech, Birmingham, AL) in blocking buffer for 1h at RT. After three washes with TBST and three washes with diH2O, bound HRP was detected using TMB Stabilized Substrate for Horseradish Peroxidase (Promega, Madison, WI).

Viral inhibition assay. HeLa cell suspensions were confirmed to be >98% viable, their concentration adjusted to 1×10^5 cells/ml, and then plated in 96 well plates with 200 µL per well (Corning, Inc., Corning, NY). Following 18h incubation at 37°C, 5% CO_2, growth media was discarded and replaced with 62.5 µL of protein in complete DMEM. A total of 11 half-log

dilutions were tested in quadruplicate for each protein. Following 1h incubation, 50 µL of Ad3-GFP virus in complete DMEM was added at a Multiplicity of Infection (MOI) of 100. Two hours later, media was removed and replaced with fresh DMEM, and the plates incubated at 37°C and 5% CO_2. The following day, GFP fluorescence was measured from the bottom read orientation at 475 nm Excitation and 505 nm Emission using a SpectraMax i3x plate reader (Molecular Devices, Inc., Sunnyvale, CA). Data were plotted using Graphpad Prizm (GraphPad Software, Inc., La Jolla, CA) and the IC_{50} determined using a 5-parameter non-linear fit of the sigmoidal curves in Softmax Pro software (Molecular Devices).

SPR analysis of binding affinities to rhDSG2. SPR analysis was performed at 25°C using a Biacore 3000 instrument (GE Healthcare, Pittsburgh, PA). For immobilization of DSG2, rhDSG2 (10 µg/ml) was captured on a CM5 sensor chip using amine coupling chemistry until a coupling level of 6000 RU was obtained. $GB7_{V239D}$ and $GB3_{V239D}$ binding were measured in 10 mM HEPES, 150 mM NaCl, 0.005% surfactant P20, 2 mM $CaCl_2$ pH 7.4 at a flow rate of 15 µl/min. A total of three dilutions of $GB7_{V239D}$, ranging from 19 nM to 9.5 nM, and 4 dilutions of $GB3_{V239D}$, ranging from 8.3 nM to 0.83 nM, were tested. For immobilization of junction opener proteins, JO-4 and $GB7_{V239D}$ were diluted to 10 µg/ml in 10 mM sodium acetate pH 4.5 and immobilized on a CM5 sensor chip (approximately 6000 RU) by standard amine coupling chemistry. Human rhDSG2 binding was measured in 10 mM HEPES, 150 mM NaCl, 0.005% surfactant P20, 2 mM $CaCl_2$ pH 7.4 at a flow rate of 15 µl/min. A total of 5 dilutions of rhDSG2, ranging from 17.4 nM to 0.87 nM, were tested in triplicate. The surfaces were regenerated by pulse injection of 5 mM EDTA. The signal recorded on a reference flow cell without protein was subtracted from those signals obtained on protein. For association data, proteins were injected at

a flow rate of 15 μL/min for 180 seconds. Following the association phase, buffer was flowed at 15 μL/min for an additional 150 seconds to measure dissociation. Binding curves were analyzed using BIAEvaluation software (GE Healthcare) and data was fit to a 1:1 Langmuir interaction model. Affinities were mathematically derived by dividing the dissociation rate by the association rate.

Size-exclusion chromatography and multi-angle light scattering analysis (SEC-MALS). Size-exclusion chromatography was performed on an Agilent 1200 HPLC system (Agilent Technologies, Santa Clara, CA) with GE HealthCare Superdex 200 Increase 10/300 GL prepacked column and 1X TBS at 1 mL/min. JO-4, $GB3_{V239D}$, and $GB7_{V239D}$ were at concentrations of 2.5 mg/mL, 2.8 mg/mL, and 2.5 mg/mL in PBS with 5% glycerol, respectively, with 100 μL of each injected. Protein was measured via UV absorbance at 280 nm and sizes determined based on multi-angle light scattering (MALS), with concentration determined using differential refractive index. Analyses were performed using a miniDAWN TREOS MALS detector and Optilab T-rEX differential refractometer using ASTRA software (Wyatt Technology Corporation, Santa Barbara, CA), with the weighted average of the molecular weight reported in g/mol (Mw). For reduction of proteins, DTT was added to an initial concentration of 1.6 mM, proteins were incubated at 50°C for 10 min, and then an additional 1.6 mM DTT was added to maintain the reduced conformations throughout the SEC-MALS analysis.

Transmission Electron Microscopy. Recombinant GB proteins were visualized by negative-stain electron microscopy. Standard mica-carbon preparations were used with protein at 0.1

mg/ml. Samples were stained using 2% (wt/vol) uranyl acetate and visualized on a JEOL (JEM-1200EXII) electron microscope at 100 kV. Images were acquired and analyzed by digital micrograph software (Gatan).

Conjugation of JOC-*x* to PEG-biotin, DOTA, and labeling with europium. JOC-*x* was conjugated to both PEG_2-biotin and PEG_{11}-biotin using the EZLink™ Maleimide-PEG2-Biotin and EZLink™ Maleimide-PEG11-Biotin kits respectively (ThermoFisher Scientific, Waltham, MA, USA). JOC-x protein was first reduced by adding dithiothreitol (DTT) at a concentration of 10 mM and incubated at 37C for 1 hour. DTT was then removed by running the solution through Zeba desalting columns (ThermoFisher Scientific, Waltham, MA, USA). The maleimide-$PEG_{2/11}$-Biotin was then added at a molar ratio of 20:1 (biotin:JOC-*x*) and allowed to react, rotating at 24 hours at room temperature. Excess $PEG_{2/11}$-Biotin was then removed, again by Zeba desalting columns. Confirmation of biotin conjugation was subsequently carried out by SDS-PAGE analysis. LanthaScreen™ Eu-Streptavidin (ThermoFisher Scientific, Waltham, MA, USA) was used as the streptavidin-europium (SA-Eu) payload. JOC-Biotin and the SA-Eu were mixed at a molar ratio of 1:1 in solution, allowed to bind at room temperature for 30 minutes, and then were subsequently run on a SDS-PAGE gel. The gel was then transferred to a PVDF membrane and imaged using the SpectraMax i3x imager (Molecular Devices, San Jose, CA, USA), at an emission wavelength of 616 nm.

For DOTA conjugation to JOC-*x*, JOC-*x* was reduced by adding DTT at a concentration of 0.1 µg/mL and incubated at 37 °C for 1 hour. DTT was then removed by running the solution through Zeba desalting columns. Maleimido-mono-amide-DOTA (Macrocyclics, Dallas, TX, USA) was then added to JOC-x at a molar ratio of 10:1 (DOTA:JOC-x), and allowed to react at

room temperature overnight. Confirmation of DOTA conjugation to JOC-x was carried out by SDS-PAGE and mass spectrometry. Europium ions were sourced from $EuCl_2 \cdot 6H_2O$ (Sigma-Aldrich, St. Louis, MO, USA). The JOC-DOTA was buffer exchanged into an ammonium acetate buffer at pH 5.8 to promote chelation of Eu. $EuCl_2 \cdot 6H_2O$ was then added at a molar ratio of 10:1 ($EuCl_2 \cdot 6H_2O$:JOC-DOTA) and allowed to react at 37 °C for 1 hour and left at room temperature for 24 hours. 10 × molar excess (of Eu added) of ethylenediaminetetraacetic acid (EDTA) was then added to chelate and remove free Eu. This was followed by running the solution through a Zeba desalting column (ThermoFisher Scientific, Waltham, MA, USA) to eliminate residual europium and to restore the protein buffer to a phosphate pH 7.0 buffer. Confirmation of Eu chelation was done by the direct dot blot, where 10 µg of the protein was blotted onto PVDF membrane, and imaged by the SpectraMax i3X (Molecular Devices, San Jose, CA, USA) at an emission wavelength of 616 nm.

Conjugation of JOC-x to poly(I:C) and measurement of TLR3 signaling. Low molecular weight (LMW) poly(I:C) (Invivogen) was resuspended to a final concentration of 10 mg/mL in 10 mM sodium phosphate, 150 mM NaCl, 10 mM EDTA, pH 7.2. Seven hundred and fifty microliters of LMW poly(I:C) was then mixed with 125 mg of 1-ethyl-3-(3-dimethylaminopropyl)carbodiimide (EDC) in a 15-mL Falcon tube. Next, 0.5 mL of 250 mM ethylenediamine in 100 mM imidazole was added to the poly(I:C), thoroughly vortexed, and 2 mL of 100 mM imidazole was added and allowed to react overnight at RT. The following day, unreacted EDC and ethylenediamine were removed from the poly(I:C)-NH2 by two passes through a 5 mL 7k MWCO Zeba™ Spin Desalting Columns (Thermo Scientific) that were equilibrated with 100 mM sodium phosphate, 150 mM NaCl, 5 mM EDTA, pH 7.2. Purified

poly(I:C)-NH2 was then incubated with a 100-fold molar excess of sulfosuccinimidyl 4-(N-maleimidophenyl)butyrate (sulfo-SMPB) (Thermo Scientific) for 1 hour at RT before removing excess sulfo-SMPB with two passes through ZebaTM columns as described above. Simultaneously, JOC-*x* was incubated with 5 mM tris(2-carboxyethyl)phosphine (TCEP) for 30 minutes at RT before removing excess TCEP with two passes through Zeba^{TM} columns. Finally, poly(I:C)-NH2 was incubated with JOC-*x* at a 1:2 molar ratio at RT overnight. Conjugation was confirmed by nucleic acid gel electrophoresis, SDS-PAGE, and Western blot.

TLR3 signaling was measured using a commercial HEK-Blue™ hTLR3 Assay (Invivogen, San Diego, CA) according to manufacturer's specifications. TLR3 activation resulted in NFκB- and AP1-induced production of the reporter gene Secreted Embryonic Alkaline Phosphatase (SEAP).

3.4 Results

Generation of a protein without internal cysteines and with a free cysteine for conjugation. JO-1 has two native cysteinyl residues (amino acids 80 and 255) which, based on the crystal structure, are spatially distant and unlikely to form intramolecular disulfide bridges (Figure 3-1a). A total of ten JO-1 derivatives (termed GB1-10) were generated, six containing the dimerization domain and four in which the dimerization domain was eliminated to interrogate the effects on multimerization and DSG2 binding activity (Table 3-1). GB1 is an identical protein to JO-1 which was codon optimized to maximize expression in *E. coli.* GB2 was constructed by mutating the native internal cysteines of GB1 to serinyl residues to limit oxidation and covalent aggregation. Next, we reintroduced a single cysteine to act as a designer sulfhydryl-based site for targeted conjugation at various locations within the proteins as follows: in GB3 the cysteine was added at the C-terminus following a flexible glycine serine linker [$(G_4S)_3$]; in GB4 and GB10, the single cysteinyl residue was added at the N-terminus either before (GB4) or immediately following (GB10) the His tag; and for GB6, the cysteine was introduced proximal to the E299V within the H-I loop (PE<u>C</u>TT, underlined in Fig. 3-1a), one of 3 key regions of the protein required for stabilization of DSG2 binding.

The free cysteine functions as a covalent mediator of multimerization. The DD contains 5 repeats of seven amino acids, with each repeat containing two lysines, which we predicted could potentially result in ribosomal stalling during translation and lower protein yields. Addition of the DD, with its predicted isoelectric point (*p*I) of ~10.91, to the Ad3 knob results in an increase in predicted *p*I from ~7.32 (Ad3 knob) to ~8.65 (JO-1). We therefore hypothesized that removal of the DD would likely 1) lower aggregation beyond the levels observed with the cysteine-

deleted GBs, 2) enhance protein expression levels, and 3) return the protein to a neutral *p*I leading to lower residual endotoxins following purification. To test this hypothesis, GB5, GB7, GB8 and GB9 were designed without the DD and a single cysteine inserted as follows: GB5 contained no cysteine; GB7 was constructed similar to GB3 with the C-terminal $(G_4S)_3$ followed by a terminal cysteine residue; GB8 contained a cysteine immediately following the His tag; and GB9 was similar to GB6 with a cysteine in the H-I loop (Fig. 3-1a and Table 3-1).

Elimination of the dimerization domain confers multiple production advantages. Nine of the 10 GB proteins were produced in *E. coli.* The exception, GB6, failed to express stable protein and was eliminated from further analysis. Expression levels of GBs containing the DD were ranged from 0.5-5 mg/L, similar to JO-1, whereas clones without the DD were 4-10-fold higher ranging between ~5-20 mg/L. Endotoxin levels of clones containing the DD ranged from 80,000 to ~1,500,000 EU/mg with an average of 691,300 EU/mg as determined using the Limulus Amebocyte Lysate (PTS-LAL) assay (Charles River Laboratories, Inc., Charleston, SC). In addition, endotoxin was nearly impossible to remove without significant protein losses. In contrast, endotoxin levels of DD-deleted clones were 100- to 1000-fold lower ranging from ~3000-20000 EU/mg. Production chromatography of GB7 (with no DD and a single C-terminal cysteine) resulted in an average endotoxin level of only 2500 EU/mg which was easily reduced to <10 EU/mg following a single pass through an endotoxin removal column.

Functional responses are preserved. The remaining GB proteins migrated according to their expected molecular weight on boiled and reduced SDS-PAGE (Supplementary Figure 3-1a). Previous data had indicated that denatured, improperly folded, or otherwise inactivated JO-1 will

not form higher-order multimers on non-reduced SDS-PAGE, will not bind DSG2, and will not inhibit viral entry (125). We assessed multimerization using samples that were not reduced and not boiled prior to SDS-PAGE (Supplementary Figure 3-1b), which-while not true native analysis-allows this family of proteins to retain multimeric forms even in the presence of SDS detergent. Several multimeric states were observed including monomers (M), trimers (T), trimer-dimers (T-D), and multimers/aggregates (Agg.) at >150kDa. In the non-reducing gel, all nine GB proteins formed higher order multimers, although a significant percentage of GB9 maintained a monomeric state. GB5 appeared to form trimers but did not produce higher MW isoforms such as trimer-dimers.

To confirm the presence of active conformations, the panel was tested for binding to human DSG2 by Western analysis probing with labeled hDSG2 (Supplementary Figure 3-1c). Except for GB5 and GB9, prominent DSG2 binding was visible in the region of the blot corresponding to trimers, timer-dimers, and aggregates, but not at the size corresponding to monomers. This result was not unexpected for GB5 given the lack of higher MW multimers beyond the trimer. GB9, despite forming multiple higher order multimers, failed to bind DSG2 confirming earlier reports on the importance of the H-I loop as one of three key regions required for DSG2 binding by the Ad3 knob (125, 132).

We next assessed the ability of the GBs to bind to DSG2 *in vitro* using HeLa cells in a competition-based viral inhibition assay (VIA) (Supplementary Figure 3-1d) (125). This assay determines the minimum protein concentration required to inhibit 50% entry of a fluorescent Ad3 reporter virus and is a robust predictor of *in vivo* activity. These viral inhibition curves can be fit to a 5-parameter curve from which the concentration at which 50% of viral entry is inhibited (IC_{50}) can be calculated and reported in μg/mL. IC_{50} values for the ten GBs are listed in

Table 3-1. Seven of the nine GBs had binding curves similar to JO-1, with GB5 showing significantly lower and GB9 showing almost no Ad3 virus inhibition.

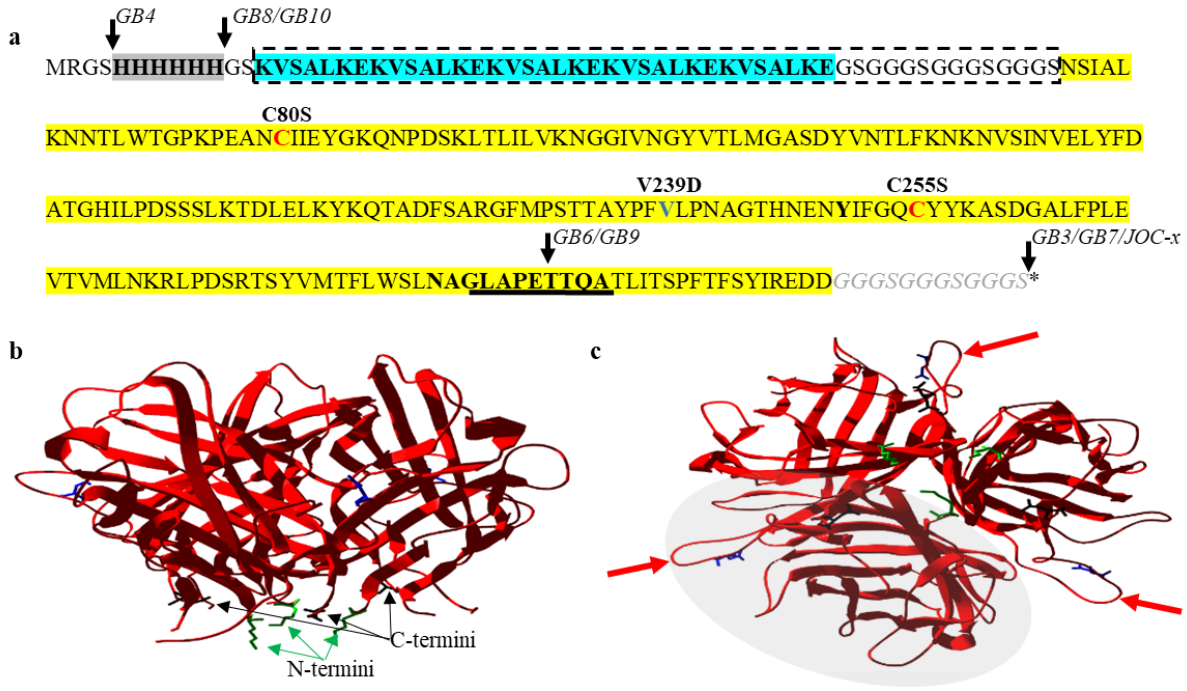

Figure 1. Sequence and structure of JO-1.

Figure 3-1 Sequence and structure of JO-1.

Panel (a) shows the amino acid sequence of JO-1 with the 6×His-tag highlighted in grey, the dimerization domain is shown in bold text and highlighted in light blue, and the Ad3 knob highlighted in yellow. The affinity-enhancing V239D mutation and two internal cysteines at aa80 and 250 are indicated above their respective residue. The H-I loop is underlined. In dimerization domain-deleted mutants, residues deleted are shown by the dashed box. Cysteinyl residues were inserted at locations shown by black arrows in each GB protein indicated next to the arrow. **Panel (b)** represents side view of the JO-4 trimer structure indicating the location of the N- and C-termini. **Panel (c)** shows a top down view of the trimer with red arrows highlighting the DSG2 binding loop in this view. The grey shaded oval approximates one JO-1 monomer. The structures are adapted from that of PDB Accession # 1H7Z_A as reported previously (63, 125).

Protein	DSG-2	VIA IC_{50}	Schematic representation of protein design
JO-4	Yes	0.067	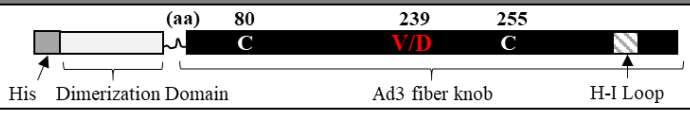
GB1	Yes	0.025	
GB2	Yes	0.030	
GB3	Yes	0.029	
GB4	Yes	0.037	
GB5	Minimal	0.241	
GB6	n/a	n/a	
GB7/JOC-*x*	Yes	0.032	
GB8	Yes	***0.012***	
GB9	No	>10	
GB10	Yes	0.026	

Table 1. Phenotypic and schematic representation of JO-derived protein constructs.

Table 3-1. Phenotypic and schematic representation of JO-derived protein constructs.

Down-selection of next generation conjugatable junction openers. Based on production levels, DSG2 binding, and viral inhibition results, we down-selected GB3 and GB7 for further characterization of multimerization. To improve binding kinetics of GB3 and GB7, we introduced the JO-4 mutation by substituting a valine at position 239 for an aspartic acid resulting in the high affinity versions $GB3_{V239D}$ and $GB7_{V239D}$. We prioritized GB7 over GB8 since having a cysteine at the C-terminus would be advantageous for conjugation of the protein to effector molecules (drugs, antibodies, poly(I:C), or isotopes) as well as delivery systems such as nanoparticles. With respect to GB8, we also hypothesized that conjugation to a cysteine proximal to the 6×his tag could pose steric hindrances which could affect downstream purification efforts.

Domains of DSG2 are cleaved and shed by the action of matrix metalloproteinases in a process that is enhanced by treatment with our junction opener constructs. This shed DSG2 can be quantified using a simple ELISA (91). Over the course of 48 hours, JO-4, $GB3_{V239D}$, or $GB7_{V239D}$ all resulted in increased DSG2 shedding compared to untreated cells (data not shown). For a more accurate measurement of DSG2 binding, we compared the avidities and association/dissociation rates of JO-x derivatives to DSG2. Surface plasmon resonance (SPR) analysis was performed by immobilizing recombinant human DSG2 (rhDSG2) onto a Biacore sensor chip and flowing JO-4 and $GB7_{V239D}$ over the surface. A roughly 20-fold more avid binding of DSG2 was determined for $GB7_{V239D}$ compared to JO-4 (0.58 nM and 11.4 nM, respectively). This apparent higher affinity of $GB7_{V239D}$ appeared to be due to both a faster association rate and slower dissociation rate compared to JO-4 (Table 3-2a). In this format, JO-4 protein appeared to bind to the sensor surface somewhat non-specifically and was more difficult to regenerate from the sensor surface compared to $GB7_{V239D}$. We hypothesized that presence of

positively charged residues within the DD of JO-4 may have resulted in binding to the negatively charged sensor surface and that the greater abundance of multimers and aggregates may have retarded diffusion of JO-4 relative to $GB7_{V239D}$. To address this, we repeated the assay by immobilizing the junction openers- including $GB3_{V239D}$-and flowing DSG2 across the surface (Table 3-2b). In this format, the apparent avidities of JO-4 to DSG2 improved from 11.4 nM to 0.58 nM, while the affinity of $GB7_{V239D}$ for DSG2 was nearly identical with possibly a slight reduction from 0.58 nM to 1.19 nM. Of the three proteins, $GB3_{V239D}$ had the highest affinity of 0.11 nM primarily due to a nearly one log faster association rate of 4.4×10^6 M/s (Table 3-2b).

a. Rates following immobilization of hDSG2 protein

Protein	k_a (M/s)	K_d (1/s)	K_D (nM)
JO4	2.32×10^5	2.64×10^{-3}	11.4
$GB7_{V239D}$	1.4×10^6	8.3×10^{-4}	0.58

b. Rates following immobilization of junction opener proteins

Protein	k_a (M/s)	K_d (1/s)	K_D (nM)
JO4	7.9×10^5	4.6×10^{-4}	0.58
$GB3_{V239D}$	4.4×10^6	5.0×10^{-4}	0.11
$GB7_{V239D}$	6.3×10^5	7.5×10^{-4}	1.19

Table 2. Biacore analysis of binding to hDSG-2

Table 3-2. Biacore analysis of binding to hDSG-2

Characteristic	JO-4	$GB3_{V239D}$	$GB7_{V239D}$
***p*I**	8.91	9.11	7.30
Production level (mg/L)	1-5	1-3	10-15
Ave. endotoxin (EU/mg)	691,300K	80,500	2,500
% aggregated by SEC[A]	90 / 94%	55 / 43%	12 / 4%
Affinity to DSG2 (nM)[B]	0.58	0.11	1.2
DSG2 shedding (fold over PBS treated at 48h)	1.44	1.52	1.39
VIA IC_{50} (μg/mL)	0.067	0.029	0.032

[A]*First value reported is untreated, second value is following reduction with DTT.*
[B]*Reported values are based on immobilization of junction opener proteins.*

Table 3. Summary of key characteristics of JO4-derivatives.

Table 3-3. Summary of key characteristics of JO4-derivatives

Junction openers without the dimerization domain exhibit minimal aggregation. To investigate the quaternary structure of the proteins, we performed SEC-MALS on JO-4, $GB3_{V239D}$, or $GB7_{V239D}$. Each protein was tested in the native (presumably oxidized) form or following treatment with low levels of dithiothreitol (DTT) to reduce disulfide bonds. The UV traces of these analyses are shown in Figure 3-2a whereby the shaded and numbered boxes indicate where the (1) aggregates, (2) multimers, (3) trimer-dimers, (4/5) trimers, and (6/7) monomers eluted based on size determination by the MALS detector.

The MALS analyses - including percentage of each species, molecular weights, and elution times - are summarized in Figure 3-2b. JO-4 presented a dominant peak in the region corresponding to aggregates with a large portion of the protein found as aggregates or high MW multimers. Reduction of JO-4 with DTT did not significantly alter the aggregation phenotype. Removal of internal cysteines in $GB3_{V239D}$ reduced the aggregation phenotype and increased levels of trimers and trimers-dimers relative to wild-type JO-4. In the oxidized state, $GB7_{V239D}$ existed in higher order states which were largely disrupted by reduction leading to a significant increase in free trimers (91%) in the reduced state. This is consistent with the engineered cysteinyl residue performing as expected allowing for targeted multimerization which can be reversed by reduction. None of the 3 proteins could be found in their monomeric form even after reduction. This agrees with non-boiled SDS-PAGE analysis in which almost no visible monomers are observed even in the presence of reducing and denaturing agent.

Further investigation of the quaternary structure was performed using uranyl acetate negative staining of protein smears and imaging by transmission electron microscopy (TEM) (133). As shown in Figure 3-3a, JO-4 exhibited relatively uniform higher order structures approaching 50 nm in diameter (white arrows) that resemble the penton-dodecahedra (Pt-Dd)

described previously (61, 134). Penton-dodecahedra are believed to be made up of 12 pentons of pentameric base and 12 trimers of the fiber knob with a predicted mass of at least 1253 kDa. This is similar to the size measured by SEC-MALS for the JO-4 aggregates, which were estimated at ~1120 kDa in the oxidized state. By TEM, $GB3_{V239D}$ exhibits fewer high MW aggregates compared to JO-4. This phenotype is even more pronounced with $GB7_{V239D}$ as only a few aggregates are observable in the image field. The white specks in the background and prevalent throughout the images were presumed to be trimers and/or trimer-dimers, the latter of which have been described as resembling barbell-like structures. Using the Visual Molecular Dynamics program (VMD, U. of Illinois Urbana-Champaign) (135) and the known x-ray crystallographic coordinates for JO-4, we modeled the trimer-dimer structure shown in Figure 3-3c. Fine resolution enhancement of seven of these white specks from the $GB7_{V239D}$ image in Figure 3-3b revealed structures resembling the barbell-shapes associated with trimer-dimers. In the model, the trimer-dimer is approximately 7 nm wide and 11.5 nm long, consistent with the size observed in the TEM images.

Junction openers with alternate multimerization strategies maintain full viral inhibition.

As mentioned above, SEC-MALS analysis suggested that reduction had almost no impact on JO-4 multimerization and only minimal impact on $GB3_{V239D}$. By contrast, reduction had a significant impact on $GB7_{V239D}$ and resulted in marked transition from aggregates/multimers to the trimeric form. Given the ability of trimers to bind DSG2, but not open tight junctions, we performed the viral inhibition assay on reduced and non-reduced proteins (Supplementary Figure 3-2a). For JO-4, oxidized and reduced inhibition curves were nearly indistinguishable from one another and resulted in nearly identical IC_{50} values. The IC50 values for all 3 junction openers in the oxidized

and reduced state are shown in Supplementary Figure 3-2b. For $GB3_{V239D}$, reduction resulted in an approximately two-fold decrease in viral inhibition likely due to loss of the trimer-dimer band seen in Figure 3-2a. As expected with $GB7_{V239D}$, reduction with DTT resulted in a 5-fold decrease in viral inhibition corresponding to the loss of the trimer-dimer peak in the $GB7_{V239D}$ SEC analysis in Figure 3-2a.

a

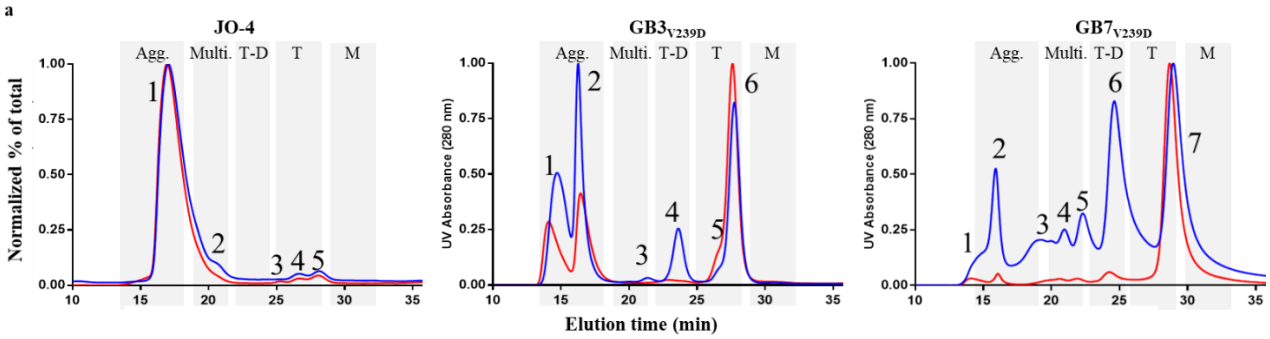

b

Approx. Elution Time (min)	Approx. MW (kDa)	Likely species	% total of each species					
			JO-4		$GB3_{V239D}$		$GB7_{V239D}$	
			Oxidized	Reduced	Oxidized	Reduced	Oxidized	Reduced
13.8-18.2	3000-578	Aggregate (Agg.)	90	94	55	43	12	4
19.2-21.5	334-289	Multimer (Multi.)	4	<0.5	2	<0.5	12	4
22.2-24.6	167-144	Trimer-Dimer (T-D)	<0.5	1	10	3	8	2
25.0-28.3	83-72	Trimer (T)	2	2	33	53	67	89
29.2-32.4	24-28	Monomer (M)	4	3	<0.5	<0.5	<0.5	<0.5

Figure 2. SEC-MALS analysis of protein multimeric states.

Figure 3-2 SEC-MALS analysis of protein multimeric states.

Panel (a) shows SEC plots for JO-4 (left), $GB3_{V239D}$ (middle), and $GB7_{V239D}$ (right). The blue line represents the A280 absorbance for the oxidized protein while the red line represents the reduced protein. The *y*-axis represents the approximate fraction of each peak while the *x*-axis shows the elution time in minutes. The grey shaded boxes indicate the approximate retention time for (1) aggregates, (2) multimers, (3) trimer-dimers, (4) trimers, (5-7) monomeric or transitional based on MALS analysis. **Panel (b)** shows the relative percentages of each species, based on MALS analysis, for the oxidized or reduced proteins with the numbers below the corresponding peak.

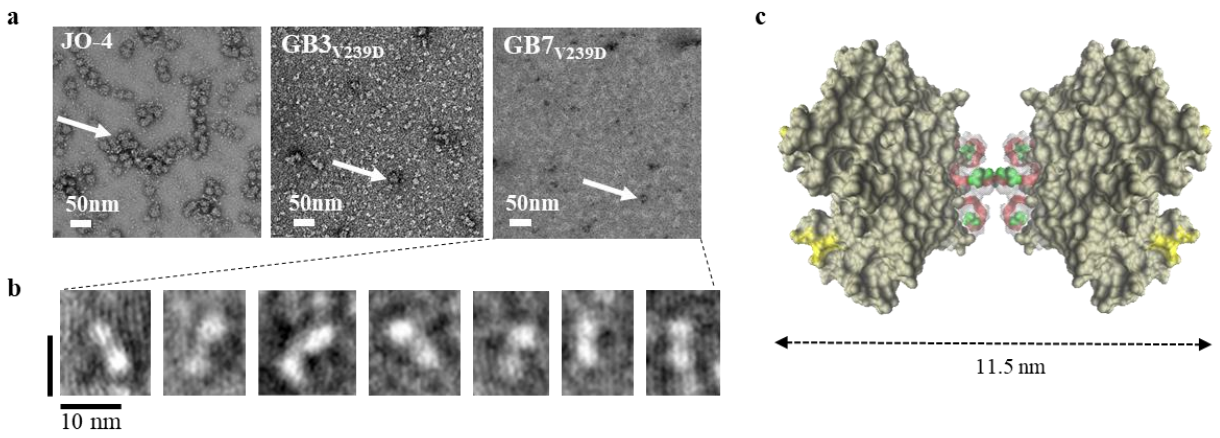

Figure 3. TEM images of protein aggregation and trimer-dimer formation.

Figure 3-3. TEM images of protein aggregation and trimer-dimer formation. Panel (a) shows the uranyl acetate negative staining of protein for JO-4 (left), $GB3_{V239D}$ (middle), and $GB7_{V239D}$ (right). The white arrows indicate aggregates which appear nearly 50 nM in diameter according to the 50nM size bar in white at the lower left of the figure. **Panel (b)** shows fine resolution imaging of white specks seen in the $GB7_{V239D}$ image in panel a. These structures show the typical barbell structure assumed to be the trimer-dimer. **Panel (c)** shows the space-filling model of the trimer-dimer of JO-4 created in VMD using the known x-ray crystallographic coordinates of JO-4. The approximate sizes of the trimer-dimers appear to be consistent size of the structure modeled in VMD (135).

Conjugation of JOC-*x* with novel payloads. Based on the biochemical and biophysical characterization of JO-4, GB3/GB3$_{V239D}$, and GB7/GB7$_{V239D}$, we selected GB7$_{V239D}$ as our lead molecule and renamed it JOC-*x* for Junction Opener Conjugated to *x* to better describe its functional attributes. We then sought to demonstrate the utility of JOC-*x* as a reagent for pre-targeted radioimmunotherapy (PRIT), direct tumor imaging, and immune therapy (136-138). The basis of PRIT involves injection of a biotinylated tumor-targeting molecule, allowing the molecule to bind its target, and then visualization with a second injection of an imaging agent or radionuclide agent conjugated to streptavidin. We biotinylated JOC-*x* at the terminal cysteinyl residue using the EZ Link Maleimide-PEG2 Biotin or PEG11 Biotin kits (Thermo Scientific, Rockford, IL.). The purpose for the PEG2 or PEG11 spacers was to assess whether biotinylation would impair ability of the monomeric protein to form bioactive multimers, and if so, would increasing the linker length reduce steric hindrance and increase multimerization and activity. Following biotinylation, the JOC-*x* and JOC-PEG2/PEG11 conjugates were tested for viral inhibition as described (Figure 3-4a). JOC-PEG2-biotin and JOC-PEG11-biotin both inhibited virus with only slightly impaired IC_{50} values of 0.125 and 0.203 μg/mL, respectively, compared to 0.032 μg/mL for the unconjugated JOC-*x*. As shown in the Coomassie stained panel in Figure 4b, conjugation of either PEG2- or PEG11-biotin did not impair the ability of JOC-*x* to form multimers as evidenced by the formation of the bands in the Trimer (T) and Trimer-Dimer (T-D) range of the unreduced samples. To further functionalize the JOC-PEG-biotin conjugates, we added a streptavidin-europium (SA-Eu) moiety to the conjugate and analyzed their ability to form trimers and trimer-dimers even with the bulky SA-Eu groups attached (Figure 3-4b). Europium is a rare earth metal and was chosen for two reasons: 1) it is often used in *in vivo* imaging due to its phosphorescent properties; and 2) it is a non-radioactive surrogate for

radionuclides that may later be used for direct imaging or irradiation of tumors. The phosphorescent panel in Figure 4b shows that even with successful loading of SA-Eu to both PEG2 and PEG11 biotin conjugated JOC-*x* they were able for form trimers, trimer-dimers, and multimers (indicated by T, T-D, and M on Fig. 3-4b). An inhibition assay with the JOC-PEG-SA-Eu conjugates resulted in atypical curves of viral inhibition that could not be fit with our typical 5-parameter fit (data not shown). This is likely due to multiple binding interactions taking place simultaneously between SA multimers, SA-JOC-PEG-biotin, and JOC-PEG-SA-Eu to the DSG2 on cells. However, we do not consider this problematic given that the full conjugate-payload, JOC-PEG-SA-Eu, would not be directly injected into an animal, but rather would be used stepwise as performed with PRIT. Specifically, JOC-*x* biotin would first be injected and allowed sufficient time to localize to the tumor, then would be followed up by a second injection of streptavidin-*x* (where *x* is europium or radionuclides useful for imaging) to allow the complexes to be formed only at the site of JOC-biotin localization.

A different methodology to generate a directly labeled, less bulky, and more flexible tumor imaging and radiotherapy agent involved conjugation to 1,4,7,10-tetraazacyclododecane-1,4,7,10-tetraacetic acid (DOTA) to the JOC-*x* resulting in JOC-DOTA. DOTA/Eu labeled proteins have been used extensively for *in vivo* imaging (139-141) and also have the advantage of being able to sequester radionuclides, such as yttrium-90, which may be used to irradiate their targets (142-145). Because of the small size of DOTA (526 Da), we used mass spectrometry to confirm that the DOTA molecule was attached to JOC-*x*. Figure 3-4c shows a mixture of unconjugated JOC-*x* and JOC-DOTA with their respective spectra at 24137 Da and 24663 Da, respectively.

The JOC-DOTA was then complexed with Europium ions to form JOC-DOTA (Eu) and successful labeling was demonstrated by reduced and non-reduced SDS-PAGE (Figure 3-4d). Coomassie staining (top gel) showed that JOC-*x*, JOC-DOTA (empty), and JOC-DOTA (Eu) all were able to form trimers in the unreduced analysis. A second, identical gel was transferred to a PVDF membrane and imaged using a Spectramax I3x Imager (lower blot) to capture europium phosphorescence. As shown in Fig. 3-4d, only the JOC-DOTA (Eu) produced phosphorescence at the monomer (M) position in the reduced gel and the trimer (T) position in the unreduced gel. We demonstrated that the DOTA conjugates maintained their ability to bind DSG2 using the viral inhibition assay (Figure 3-4e) with IC_{50} values of 0.055, 0.131, and 0.254 μg/mL for JOC-*x*, JOC-DOTA, and JOC-DOTA (Eu), respectively.

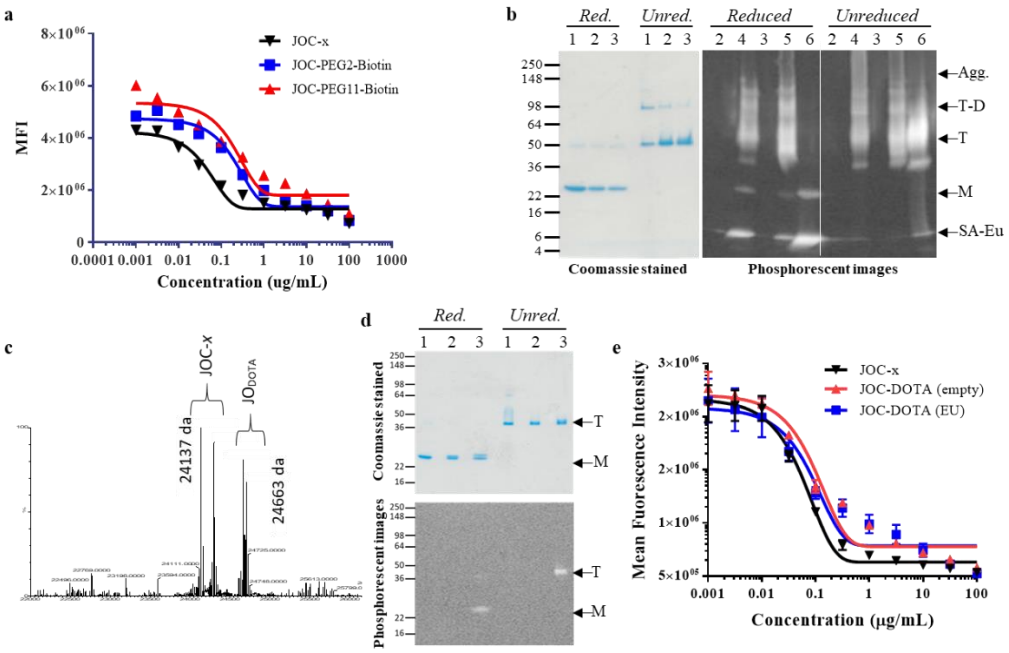

Figure 4. Conjugation of JOC-*x* with PEG-biotin or DOTA-EU

Figure 3-4. Conjugation of JOC-*x* with PEG-biotin or DOTA-EU. Panel (a) Shows the viral inhibition curves for JOC-*x* before and after conjugating to PEG2- or PEG11-biotin. **Panel (b)** JOC-*x* and JOC-Biotin conjugates were mixed with streptavidin-europium (SA-Eu) and resolved by SDS-PAGE with or without boiling or reduction by DTT. One gel was stained with Coomassie to visualize formation of multimers and one gel transferred to a PVDF membrane and imaged using a Spectramax I3x Imager to visualize EU phosphorescence at an emission spectrum of 616 nm. Multimeric forms are indicated to the right of the gel/blot whereby SA-Eu = free streptavidin-europium, M= Monomer, T= Trimers, T-D=, and Agg.= Aggregates/multimers Numbering of lanes is as follows: 1=JOC-*x*, 2=JOC-PEG2-biotin, 3= JOC-PEG11-biotin, 4= JOC-PEG2-biotin-SA-Eu, 5= JOC-PEG11-biotin-SA-EU, 6=SA-Eu alone; **Panel (c)** A mass spectrometry spectrum for JOC-DOTA is shown indicating the position of unconjugated JOC-*x* (24137 Da) and JOC-DOTA (24663 Da). **Panel (d)** Unconjugated JOC-*x* (1), JOC-DOTA (empty) (2), and JOC-DOTA (Eu) (3) were resolved by SDS-PAGE, with or without boiling or

reduction by DTT. One gel was stained with Coomassie (top gel) to visualize formation of multimers and one gel transferred to a PVDF membrane and imaged using a Spectramax I3x Imager (lower blot) as described above. Positions of Trimers “T” and monomers “M” are noted to the right of the gel/blot. **Panel (e)** Viral inhibition curves of JOC-*x*, JOC-DOTA (Empty), and JOC-DOTA (Eu) are shown indicating that DOTA-EU conjugation only minimally reduces DSG2-mediated viral entry.

Viral inhibition and TLR3 signaling following poly(I:C) conjugation to JOC-*x*. A final demonstration of the utility of JOC-*x* was generation of a conjugate that would lead to innate signaling and activation through the viral RNA sensors (TLR3 and MDA5) triggered by the synthetic ligand poly(I:C). Poly(I:C) was conjugated to JOC-*x* using the heterobifunctional crosslinker SMPB [succinimidyl 4-(p-maleimidophenyl) butyrate] linking the free cysteine on JOC-*x* to the amino terminus of poly(I:C). When conjugated to JOC-*x*, the poly(I:C) was expected to add an additional 120 to 600 kDa to JOC-*x* based on the typical size of poly(I:C) which varies between 0.2 to 1.0 kb in length. Successful conjugation of poly(I:C) to JOC-*x* is demonstrated in Panel a of Figure 3-5, in which the black arrows in Lane 4 of the panels identify the JOC-poly(I:C) conjugates which maintain their predictably high molecular weight and conformation even when boiled and reduced (Lane 4). This conjugated form is not visible in either the unconjugated JOC-*x* (Lane 1), unconjugated poly(I:C) (Lane 2), or in the unconjugated mix of JOC-*x* and poly(I:C) (Lane 3). Figure 5b shows the viral inhibition of unconjugated JOC-*x* (green line, triangles), an equimolar mixture of JOC-*x* and poly(I:C) (blue line, diamonds), and the JOC-poly(I:C) conjugate (red line, circles). The unconjugated mixture of JOC-*x* and poly(I:C) was included to measure direct binding of poly(I:C) to HeLa cells given that this cell line has been demonstrated to be TLR3 positive, although TLR3 is primarily found in endosomal compartments and MDA5 in intracellular (146). In the presence of poly(I:C), unconjugated JOC-*x* exhibited a ~3.9-fold loss of viral inhibition suggesting possible binding competition. JOC-poly(I:C) conjugates maintained their ability to bind DSG2 and inhibit viral entry, although the slight shift of the inhibition curve to the right is reflective of an approximately 6.3-fold lower IC_{50} of the conjugate relative to the unconjugated protein (0.032 vs 0.203 μg/mL, respectively). To assess whether the JOC-poly(I:C) could bind to TLR3 receptors and induce cell signaling, we

utilized an *in vitro* HEK-Blue human TLR3 reporter cell line (Invivogen, San Diego, CA). As shown in Figure 3-5c, we demonstrated that JOC-poly(I:C) conjugates were able to bind to TLR3 and induce signaling at significantly lower protein concentrations compared to poly(I:C) alone or a mixture of JOC-*x* and poly(I:C). For example, with poly(I:C) alone (Fig. 3-5c, purple bars) or a mixture of JOC-*x* and poly(I:C) (Fig. 3-5c, green bars), the two highest concentrations (20 and 4 μg/mL) resulted in ~15 to 17-fold upregulation in NF-kB-phosphatase expression, but at the lowest two concentrations (0.0064 and 0.00128 μg/mL) only about a twofold upregulation was seen. Strikingly, at 0.032 μg/mL, the JOC-poly(I:C) conjugates (Fig. 3-5c, red bars) still exhibited ~18-fold upregulation compared to either poly(I:C) alone or unconjugated JOC-*x*. In fact, JOC-poly(I:C) maintained 10- to 18-fold upregulation at every concentration tested down to 0.0064 μg/mL. These results suggest that the JOC-poly(I:C) conjugates may be significantly more potent in stimulating TLR3 signaling than poly(I:C) alone.

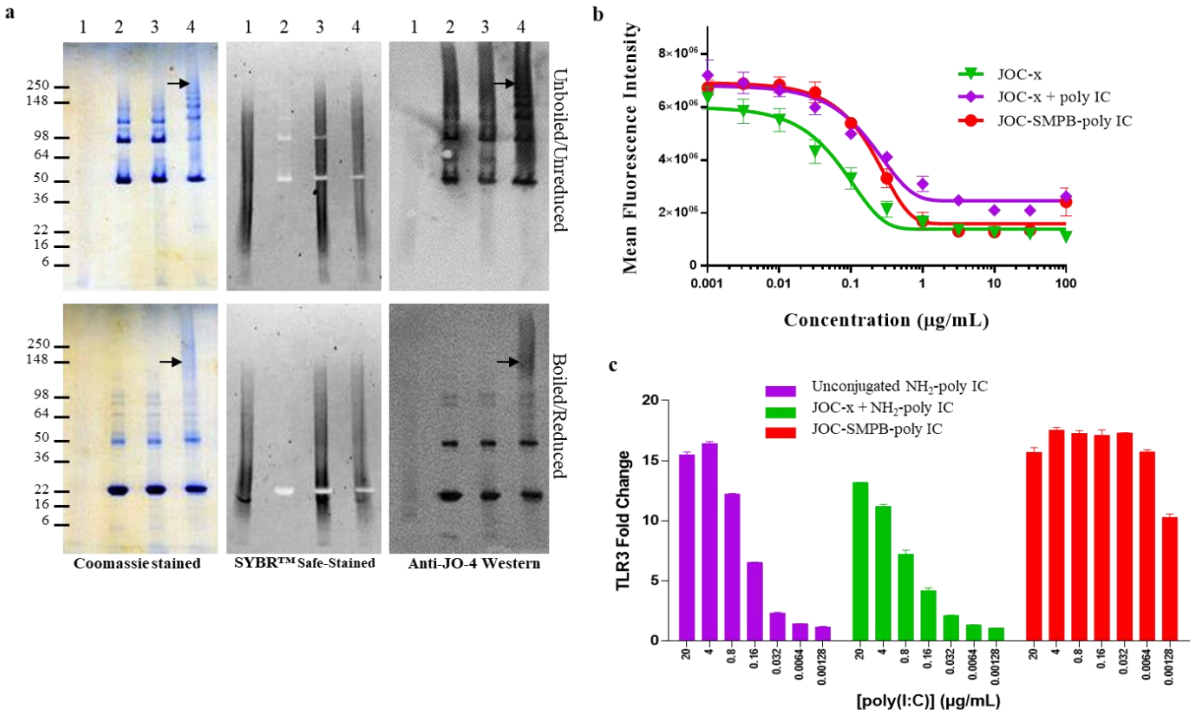

Figure 5. Viral inhibition and TRL3 signaling following poly IC conjugation to JOC-*x*

Figure 3-5. Viral inhibition and TRL3 signaling mediated by JOC-poly(I:C). Panel (a) Unboiled/non-reduced and boiled/reduced SDS-PAGE analysis of 1-unconjugated poly(I:C), 2-unconjugated JOC-*x*, 3-a mixture of unconjugated poly(I:C) and JOC-*x*, and 4-JOC-poly(I:C) are shown following imaging by Coomassie staining (left), staining with the DNA intercalating dye SYBR Safe (middle), or following blotting to PVDF and reacting with anti-JO-4 antibodies by Western blot (right). The black arrow denotes the formation of a high MW complex at around 250 kDa in lane 4 (JOC-poly(I:C) conjugates) of all three panels proving the successful conjugation of poly(I:C) to JOC-*x*. Note that even upon reduction, the high MW conjugates remain intact. Panel (b) viral inhibition curves of unconjugated poly(I:C), a mixture of unconjugated poly(I:C) and JOC-*x*, and the JOC-poly(I:C) conjugate are shown indicating that the JOC-poly(I:C) was able to inhibit DSG2-mediated viral entry, albeit at a slightly lower concentration; Panel (c) shows the fold TLR3 activation mediated by binding of unconjugated NH_4-poly(I:C) (purple bars), a mixture of unconjugated NH_4-poly(I:C) and JOC-*x* (green bars),

or JOC-poly(I:C) (red bars). Cells were incubated with 7 concentrations of agonist ranging from 20 μg/mL down to 0.00128 μg/mL in fivefold increments. It is noteworthy that even at 0.00128 μg/mL, the JOC-poly-IC still induced a >10-fold increase in TLR3 signaling.

3.5 Discussion

Epithelial cancers are characterized by tight junctions that create obstacles to naturally occurring immune cells, antibodies, and drug therapies as well as helping maintain the tumor microenvironment. We have described a new approach to exposing tumors to the action of the immune system and oncological therapy using designer proteins that bind to DSG2 and open tumor tight junctions. Our first generation molecule, JO-1, has been extensively characterized as a co-therapeutic for cancer treatment (56, 57). Binding by JO-1 leads to DSG2 cleavage, shedding, and activation of intracellular signaling pathways which facilitate the opening of junctions. JO-4, a high affinity version of JO-1, has been shown to be well tolerated *in vivo* and is being developed as a cancer co-therapeutic.

While producing a conjugatable version of JO for targeted cancer therapy we enhanced expression levels through codon optimization and removal of the dimerization domain. We mutated the internal cysteines to serines and found that this did not affect - and may even have enhanced – the activity of the protein as determined by DSG2 binding and viral inhibition. Restoration of a single cysteine was generally sufficient to recover DSG2 binding given that GB5, lacking both cysteines and the DD, failed to form higher MW isoforms and did not bind DSG2, yet still inhibited viral entry - albeit at a much lower level. Both GB7 and GB8, which differ from GB5 by only one cysteine, inhibited viral entry at comparable levels relative to JO-1. As expected, perturbation of the H-I loop involved in DSG2 binding ablated activity. We conclude that the single cysteine may lead to at least trimer-dimer formation resulting in recovery of DSG2 binding. We next down-selected GB3 and GB7 for further analysis of multimerization and aggregation, introduced the affinity-enhancing V239D mutation, and confirmed that the next generation clones $GB3_{V239D}$ and $GB7_{V239D}$ had retained comparable

activity relative to JO-4. SPR analysis confirmed the association and dissociation rates and resulting affinities of $GB3_{V239D}$ and $GB7_{V239D}$ were comparable or improved relative to JO-4.

SEC-MALS and TEM analysis of the aggregation state of the proteins revealed that JO-4 exists mainly as higher order structures resembling penton-dodecahedra (Pt-Dd) in both mass and shape. Reduction of JO-4 only minimally disrupted formation of these structures. Removing the cysteines (GB3) and dimerization domains (GB7) changed the aggregation state of the molecule but provided for an active molecule with the potential for directed attachment of therapeutics. We demonstrated that JO-4, $GB3_{V239D}$, and $GB7_{V239D}$ exhibited equivalent viral inhibition in the oxidized state, and that only $GB7_{V239D}$ showed a marked reduction in viral inhibition upon reduction consistent with the idea that multimerization beyond trimers is required for activity and that the added cysteine provides for this ability.

TEM images of $GB7_{V239D}$ revealed very few higher order structures relative to JO-4 as well as the presence of white specks throughout the image. Enhancement of these specks revealed that they were likely trimer-dimers, matching both the shape and predicted size of the trimer-dimers. Presence of these trimer-dimers, combined with the comparable viral inhibition of $GB7_{V239D}$ compared to JO-4 suggest that this protein is still fully able to bind DSG2 and act therapeutically.

Based on physical and biochemical characterization, we down-selected $GB7_{V239D}$ for our conjugation experiments and renamed our lead molecule JOC-*x* to denote that it can open tumor junctions and be conjugated to a payload (*x*). Primary reasons for choosing $GB7_{V239D}$ for our JOC-*x* included high production yields, low endotoxin binding, and controllable defined aggregation all while retaining similar DSG2 binding and viral inhibition relative to JO-4 (outlined in Table 3-3).

As proofs-of-concept for this cancer-targeting platform we first sought to generate a reagent useful for pre-targeted immunotherapy (PRIT) and direct tumor imaging by adding pegylated biotins to JOC-*x*. These JOC-PEG-biotin conjugates were active in the viral inhibition assay and were able to bind to SA-Eu for potential use in PRIT applications.

To make a second radiotherapy molecule, we conjugated a metal chelation molecule, DOTA, to JOC-*x* and demonstrated effective labeling with free europium ions. The JOC-DOTA (Eu) chelates were able to bind DSG2 and inhibit virus *in vitro* suggesting they will bind to tumor cells *in vivo* and the metal chelate can be used to irradiate or mark the tumor for *in vivo* imaging.

Finally, we generated a potent JOC-poly(I:C) conjugate which also bound DSG2, although with a ~6.3-fold lower IC_{50} compared to JOC-*x* alone in our viral inhibition assay. The reason for the lower IC_{50} may be due to either impaired kinetics of the conjugate, possibly due to steric hindrances imposed by the high MW of the poly(I:C), or may be a competitive effect caused by poly(I:C) binding to TLR3 present in the HeLa cells themselves. Despite this lower level of binding in the VIA assay, the JOC-poly(I:C) induced 10- to 18-fold upregulation of TLR3 signaling using a HEK Blue TLR3 reporter cell line at every concentration tested down to 0.00128 μg/mL. In this assay, poly(I:C) alone only resulted in a 6-fold upregulation of TLR3 signaling at a concentration that was 125 times higher (0.16 μg/mL) than the JOC-poly(I:C). These results suggest that the JOC-poly-IC conjugates are significantly more potent in stimulating double stranded RNA sensor signaling than poly(I:C) alone. Given the dual-targeting of JOC-*x* to DSG2, and poly(I:C) to TLR3, we predict our JOC-poly(I:C) may exhibit dose sparing qualities by resulting in less non-specific binding of poly(I:C) to non-tumor TLR3 cells as well as targeting the host-directed therapeutic to tumors.

The goal of this study was to develop novel tumor targeting proteins that could be directly coupled to anti-tumor effector molecules. The lead molecule, JOC-*x*, exhibited enhanced biophysical properties with respect to production yields, aggregation, and low residual endotoxins following purification while maintaining high affinity binding to the target receptor DSG2. To demonstrate the versatility of JOC-*x*, we report here DSG2 binding and viral inhibition following conjugation to pegylated biotin, streptavidin-europium, DOTA-europium, and poly(I:C). We also demonstrated that JOC-poly(I:C) induces potent TLR3 activation by inducing >10-fold upregulation at concentrations that are ~625 fold lower than poly(I:C) alone. This effect is likely due to dual targeting and internalization of the conjugate, that is by JOC targeting the conjugate to the cells via DSG2 and activation of double stranded RNA sensors TLR3 and MDA5. In healthy cells, DSG2 is mainly sequestered to the tight junctions and only minimally available for binding by JOC-*x* whereas tumor cells often exhibit upregulation in DSG2 and disordered junctions making them highly susceptible to DSG2 binding. We hypothesize that *in vivo* our JOC-poly(I:C) would likely exhibit enhanced potency by directing poly(I:C) to the tumor while at the same time minimizing non-specific activation of TLR3 receptors on healthy cells. Our JOC-*x* conjugates are primed for cGMP manufacture and hold much promise for upcoming validation and clinical studies.

3.6 Acknowledgements

Sean Gray assisted with the development of the JOC-x construct, and the biophysical characterizations (SPR, and SEC-MALS). Jenn Bergthold assisted in the set-up of the viral inhibition assay. Transmission electron microscopy was carried out by Pascal Fender. Ragan Pitner explored the JOC-x conjugation to poly(I:C).

3.7 Supplementary Figures

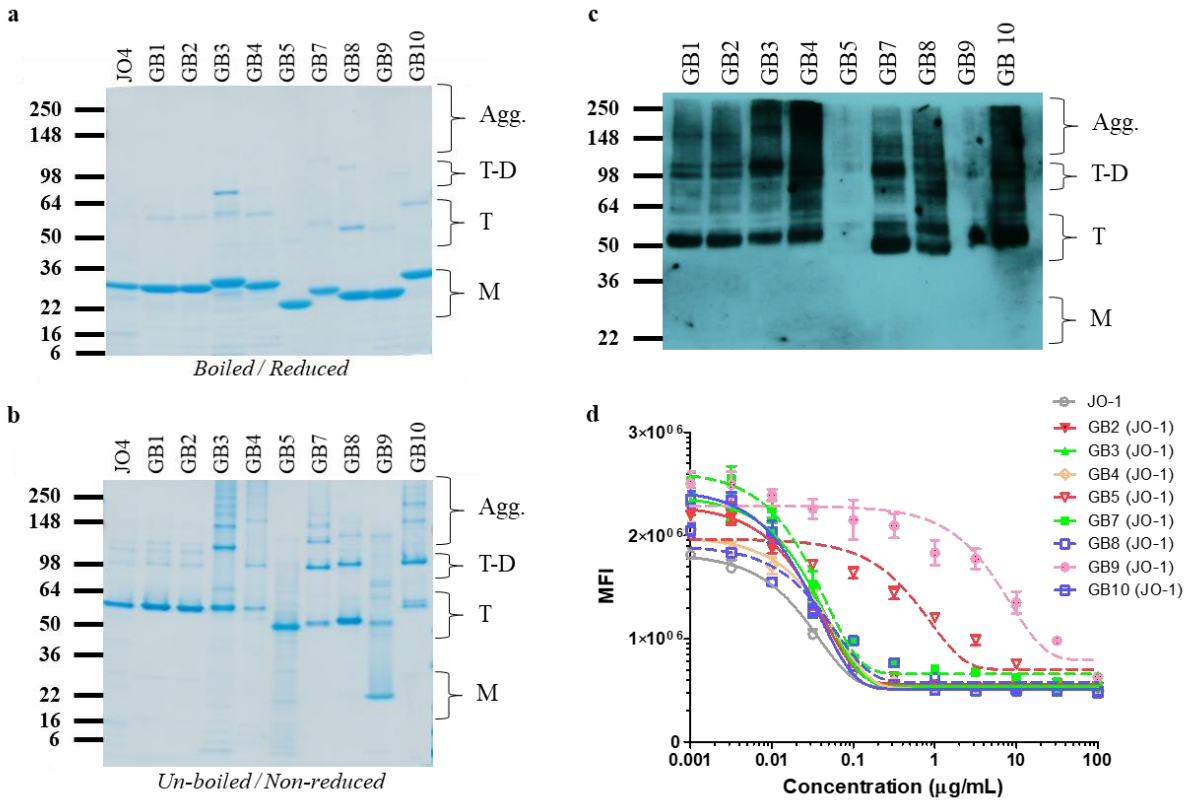

Supplementary Figure 1. Production and characterization of JO-1 derived proteins. Panels (a) shows the boiled and reduced analysis of the GB proteins on Coomassie stained SDS-PAGE. **Panel (b)** shows the non-reduced and un-boiled analysis of the same proteins. **Panel (c)** shows a DSG2 binding Western blot of the GB proteins. In panels a, b, and c the multimeric forms are indicated to the right of the gel/blot whereby M= monomers, T= trimers, T-D= trimer-dimers, and Agg.= aggregates/multimers. **Panel (d)** shows the viral inhibition curves for each protein. The IC_{50} values are shown in Table 1.

a

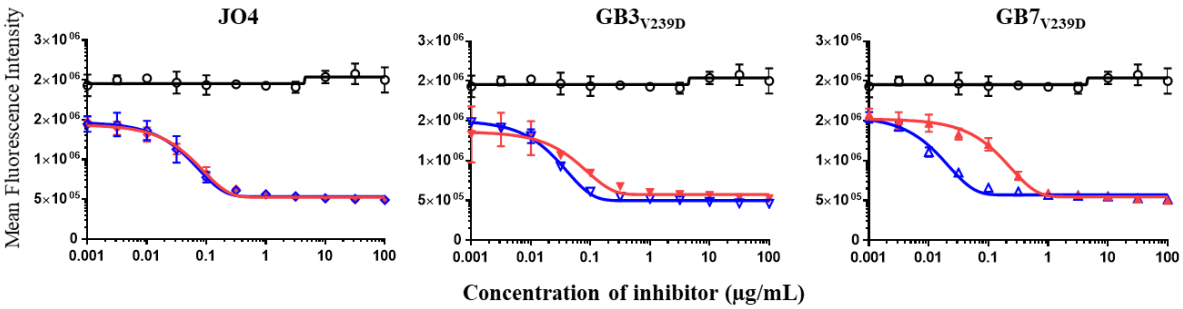

b

Protein	IC_{50} (µg/mL)		Fold lower activity upon reduction
	Oxidized	Reduced	
JO4	0.065	0.054	(0.8)
$GB3_{V239D}$	0.028	0.055	2.0
$GB7_{V239D}$	0.029	0.150	5.0

Supplementary Figure 2. Impact on viral inhibition mediated by reduction of JO-derivatives. **Panel (a)** shows the viral inhibition curves for reduced (red lines) and non-reduced (blue lines) JO-4, $GB3_{V239D}$, and $GB7_{V239D}$ proteins. Black lines show the VIA curves for the BSA control. **Panel (b)** reports the IC_{50} values for each of the VIA curves approximating the fold change in viral inhibition activity following reduction.

Chapter 4 *IN VITRO* AND *IN VIVO* EFFICACY OF A LIPOSOMAL DOXORUBICIN-JO CONJUGATE IN TUMOR MODELS

4.1 Abstract

Although new formulations of chemotherapeutics are continuing to improve outcomes in cancer therapy, side effects due to the lack of proper targeting remain major concerns in treatment. Here, we present a recombinant protein, JOC-x, which targets the tight junction protein desmoglein 2 that is overexpressed in many cancer types and potentially can act as a bait for tumor targeting. Desmoglein 2 (DSG2) is a protein implicated in the formation of tight junctions and is associated with poor outcomes in certain cancers. When bound to DSG2, JOC-x causes its cleavage and opens the junctions between tumor cells to allow efficient penetration of cancer therapeutics. In this report, JOC-x was successfully conjugated to liposomal doxorubicin using maleimide-sulfhydryl chemistry, resulting in targeted chemotherapy construct as verified by an increased nanoparticle size post-conjugation. The conjugate was tested *in vitro* and *in vivo* for its ability to kill tumor cells. The conjugate retained DSG2-binding capability and in vitro tumor cell cytotoxicity. A xenograft mouse model of colon cancer showed increased efficacy, doubling median survival in comparison to controls and increasing efficacy by 33% compared to liposomal doxorubicin alone. Mice did not show the adverse side effects usually attributable to doxorubicin. A combination of a tumor junction-targeting protein and a liposomal chemotherapeutic formulation holds promise in enabling a decreased dose of the chemotherapeutic, alleviating systemic side effects, and increasing efficacy in killing tumors.

4.2 Introduction

While chemotherapeutics have been continuously improved by the use of new formulations, drug delivery methods, and the introduction of new modes of therapy, solid cancers remain a difficult target. Solid tumors are responsible for a large proportion of cancer deaths in the United States (147), and newer modes of therapy such as CAR-T cells or immune checkpoint inhibitors have encountered some difficulty in treating epithelial cancers (148). Improvements to traditional modes of cancer therapy - such as chemotherapy and radiotherapy - are sorely needed to enhance efficacy and quality of life for patients. Modifying and enhancing the targeting of chemotherapeutics represents a promising approach, and several methods have been used including novel formulations such as nanoparticles (149), rational design of small molecules (150), and enhanced drug delivery and targeting (151). Enhanced targeting often involves a receptor or molecule overexpressed on tumor cells relative to normal cells, and well known examples of these include EGFR in melanoma or HER2/*neu* in breast cancer.

Desmoglein-2 (DSG2) is a transmembrane glycoprotein which belongs to the cadherin family and is a key component of desmosomes, a type of cell junction (46). These junctions play a role in excluding the entry of molecules as small as 400 Daltons and are prominently present in tissues requiring a watertight seal such as cardiomyocytes and the gastrointestinal epithelium (152). DSG2 is also known to be targeted downstream of epidermal growth factor (EGFR) activation, which ultimately results in the cleavage of DSG2 homodimers that form the bridge between two cells. The extracellular domain of DSG2 is then shed and can be readily detected in serum (153).

The presence of DSG2 on cancers has been researched and in several solid tumors there is an association of DSG2 expression levels and poor patient outcomes. This has been found in ovarian cancer (154, 155), non-small cell lung cancer (95, 156), melanoma (157), hepatocellular carcinoma

(158), and colorectal cancer. DSG2 overexpression has also been associated with chemoresistance in lung adenocarcinoma (96) and in our previous investigations of ovarian cancer (Data submitted for publication). One hypothesis for this phenomenon is that tumors can take advantage of the DSG2-mediated cell junctions to form tight physical barriers, thus excluding the entry of immune cells, chemotherapeutics, or monoclonal antibodies (159). Thus, DSG2 represents a target for cancer therapeutics, where modulating or decreasing the expression of DSG2 could lead to better prognosis by specific targeting of this overexpressed target on the tumor surface.

We had previously developed a protein targeting DSG2 named "Junction Opener" (JO). JO is derived from an adenovirus subtype 3, which uses DSG2 as its cellular receptor. The fiber knob portion of the adenovirus was engineered to increase affinity, resulting in a K_D of 0.58 nM (160). Upon JO binding to DSG2, the aforementioned pathway downstream of EGFR is activated, and a metalloprotease-mediated cleavage of DSG2 homodimers readily results in DSG2 shedding into the serum (161). Subsequent use of JO in xenograft cancer models in combination with monoclonal antibodies showed enhanced efficacy and slowed tumor growth (64). JO has been safely tested in preclinical studies in mice and rhesus macaques, with no noted major immunogenic or toxic side effects (162, 163) and is currently in clinical development for ovarian cancer.

In an effort to further enhance JO's utility as a cancer co-therapeutic, we generated conjugatable forms of JO (JO Conjugatable to "x" or JOC-x) by the replacement of native cysteinyls with serine residues and the addition of a cysteine residue to the newly engineered construct's C-terminus. The resulting reactive sulfhydryl at the terminus can be conjugated to a variety of moieties, including chemotherapeutics, antibodies, or radioisotope chelators. JOC-x, retained DSG2 binding activity and had the advantages of higher levels of production in *E. coli* with potentially lower residual endotoxins(160). In a further step forward, we present data here regarding the first JOC-

x therapeutic bioconjugate, JOC conjugated to liposomal doxorubicin. The conjugate was successfully prepared, and its efficacy was tested in *in vitro* and *in vivo* experiments.

4.3 Materials and Methods

Producing JOC-x: JOC-x was produced in *E. coli* HMS174 (DE3) (EMD Millipore, Darmstadt, Germany). JOC-x cloning into a pET29a expression vector (Novagen), and plasmid transformation and protein production was carried out as described previously(160). All genes used for this study were designed *in silico* using the software Serial Cloner v2.4.1. Protein molecular weight was confirmed by sodium dodecyl sulfate-polyacrylamide gel electrophoresis (SDS-PAGE) and purity was verified to be >95% by densitometry.

JOC Conjugation to Liposomal Doxorubicin: A maleimide-activated PEGylated liposomal doxorubicin formulation (Immunodox®-maleimide) was obtained from Encapsula Nanosciences (Brentwood, TN, USA). JOC-x was then conjugated to the liposome following the manufacturer's directions: DSPE-PEG(2000)-maleimide lipid tails were dried in a lipid form before hydration in a phosphate buffer solution (PBS) for at least one hour under a stream of nitrogen gas in an oxygen-free chamber. JOC-x was reduced with 0.1 mM tris(2-carboxyethyl)phosphine (TCEP) at 37°C for 1 hour to make the terminal cysteine available for conjugation. JOC-x was then added to the maleimide activated lipids at a molar ratio of 2:1 respectively, under nitrogen gas overnight at room temperature. The reaction was quenched with 2 mM 2-mercaptoethanol for 30 minutes. The JOC-DSPE-PEG(2000) was then added to liposomal doxorubicin and activated at 60°C for 30 minutes. Excess unconjugated JOC-x was then removed via dialysis, using a 300 kDa cut-off Float-a-Lyzer® dialysis cassette (Spectrum Labs/Repligen, Waltham, MA, USA) in 4 L of PBS, pH 7 overnight at 4°C. The resulting final JOC-liposomal doxorubicin was stored at 4°C until use.

Malvern Zetasizer: The final JOC-liposomal doxorubicin product was diluted 1:20 in 100 µL of PBS in a cuvette, and placed into a Malvern Zetasizer (Malvern Panalytical, Malvern, UK). Measures were plotted by intensity.

DSG2-binding Viral Competition Assay: HeLa cell suspensions were confirmed to be >98% viable using an automated cell counter, their concentration adjusted to 1×10^5 cells/ml, and then plated in 96 well plates with 200 µL of complete DMEM media [cDMEM = DMEM supplemented with 10% Fetal Bovine Serum, 2 mM Glutamax, and 100 U/mL penicillin and 100 ug/mL Streptomycin (all components from Gibco)] per well (Corning, Inc., Corning, NY). Following 18 h incubation at 37 °C and in 5% CO_2, the growth media was discarded and replaced with 62.5 µL of JO or JO derivatives in complete Dulbecco's Modified Eagles Medium (cDMEM) [A total of 11 half-log dilutions were tested in quadruplicate for each protein. Following 1 h incubation, 50 µL of Ad3-GFP virus in complete DMEM were added at a Multiplicity of Infection (MOI) of 100. Two hours later, media was removed and replaced with fresh DMEM, and the plates incubated at 37 °C and 5% CO_2. The following day, GFP fluorescence was measured in the "bottom read" orientation at 475 nm Excitation and 505 nm Emission using a SpectraMax i3x plate reader (Molecular Devices, Inc., Sunnyvale, CA). Data were plotted using Graphpad Prism 7 (GraphPad Software, Inc., La Jolla, CA) and IC_{50} values determined using 5-parameter non-linear fits of the sigmoidal curves in Softmax Pro software (Molecular Devices).

Doxorubicin Cell Cytotoxicity Assay: 1×10^4 Human colorectal carcinoma T84 cells were plated in 96-well plates in 200 µL of DMEM:F12 supplemented with 10% Fetal Bovine Serum, 2 mM Glutamax, and 100 U/mL penicillin and 100 µg/mL Streptomycin (all components from Gibco)

per well and incubated at 37°C overnight. Cell growth media was then switched out for complete DMEM:F12 without Phenol Red (190μL). 10 μL of Alamar Blue (Bio-Rad Laboratories, Hercules, CA, USA) were then added to cells and incubated at 37°C. At time intervals as noted thereafter, plates were read for 560 nm Excitation and 590 nm Emission using a SpectraMax i3x plate reader (Molecular Devices Inc, Sunnyvale, CA, USA) and fluorescence values were again plotted using Graphpad Prism 7 (GraphPad Software Inc, La Jolla, CA, USA).

In vivo tumor xenograft studies: Female immunodeficient CB17-scid mice were obtained from Taconic Biosciences (Rensselaer, NY, USA). T84 cells were cultured in F12:DMEM media as above in the DSG2-binding viral competition assay section and resuspended at a concentration of 1×10^5 cells/mL in F12:DMEM media without serum supplement. The cells were then mixed at a 1:1 ratio with Matrigel® (Corning Inc, Corning, NY, USA) and stored at 4°C prior to injection. Mice were then injected with 100 μL of the cell:Matrigel® mixture subcutaneously in the mammary fat pad, receiving a total of 5×10^4 T84 cells as determined by optimizing for tumor growth kinetics. Mice were monitored twice a week for changes in tumor size, measured as Volume (mm^3 as calculated using length x latitude^2). Upon reaching an average tumor size of 100 mm^3, mice were injected retro-orbitally with combinations of JO, Doxil®, or JOC-liposomal doxorubicin at doses of 2 mg/kg, 1 mg/kg, and 1 mg/kg doxorubicin equivalent respectively. Mice continued to be measured twice a week for tumor size and weight, until reaching a tumor volume of 1000 mm^3 when they were sacrificed. Tumor growth and survival data were plotted using Graphpad Prism 7 (Graphpad Software Inc, La Jolla, CA, USA).

4.4 Results

JOC-x can be successfully conjugated to liposomal doxorubicin

A conjugatable form of the junction-opener protein, JOC-x, was produced by removing native cysteines and adding a cysteine at the C-terminus. This allows for a sulfhydryl group available for a maleimide-mediated linkage, and the protein retains its DSG2-binding properties(160). JOC-x was chemically linked to a maleimide-DSPE lipid before its addition of the micellar mixture to the liposomal doxorubicin formulation. The resulting mixture, JOC-liposomal doxorubicin ("JOC-LD") had a doxorubicin concentration of 1.38 mg/mL as measured by doxorubicin fluorescence. A dynamic light scattering (DLS) measurement of nanoparticle size showed that the liposomal doxorubicin formulation had increased from an average size of 105.2 nm to 120.8 nm, which is in range of the expected size increase as each unit of JOC is expected to be about 5.5 nm in length, adding circa 11 nm total (Figure 1a). The JOC-LD formulation was also run on SDS-PAGE, and the JOC protein remained conjugated after presumed destruction of the liposome with heating/boiling and SDS detergent (Figure 4-1b), and was present in the multimeric forms as expected of the active form of JOC-x. Thus, JOC-x was successfully conjugated onto the liposomal doxorubicin formulation as confirmed by the expected biophysical/biochemical changes.

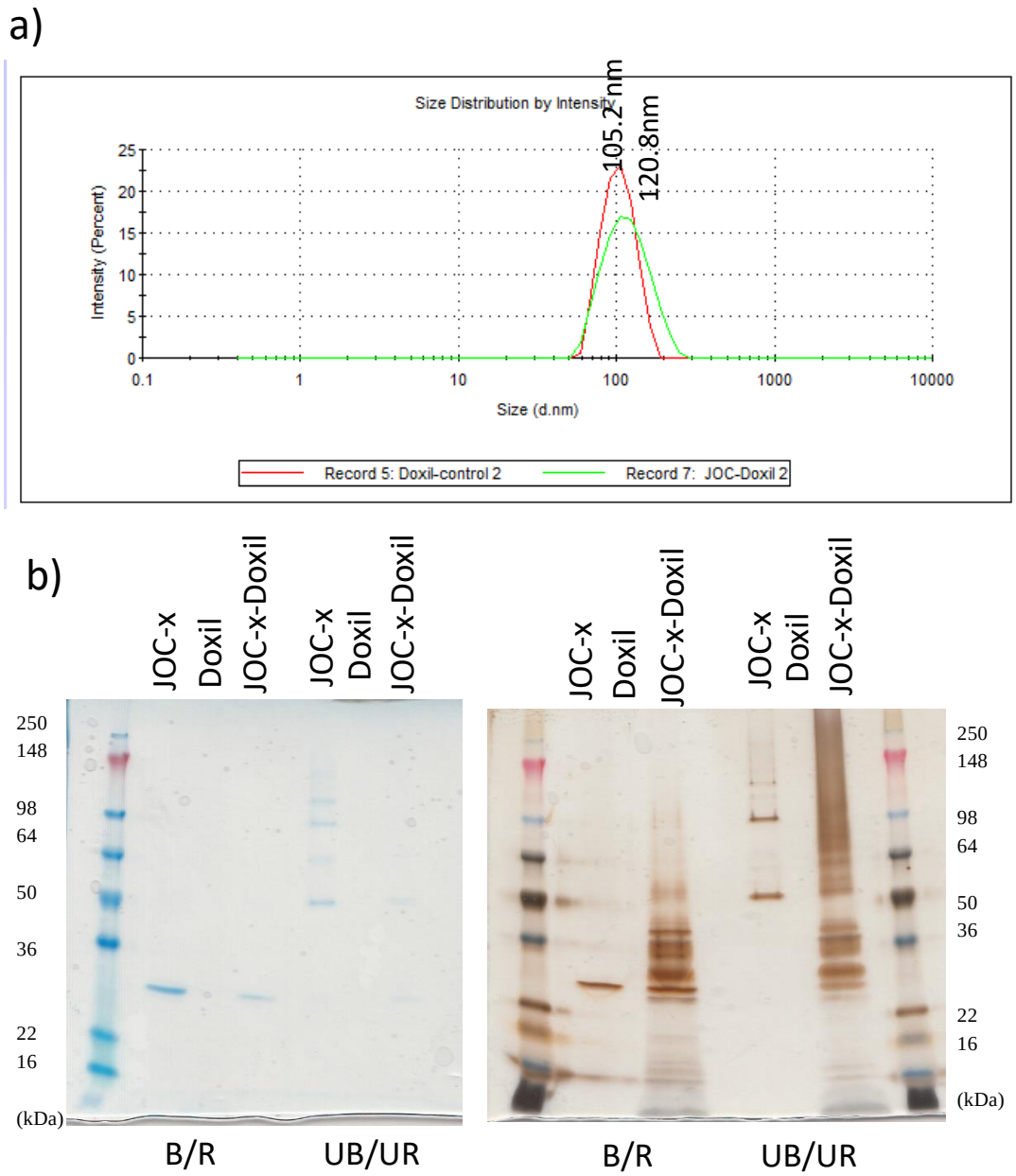

Figure 4-1 Biophysical characterization of JOC-LD conjugate

a) After conjugation of JOC to PLD, nanoparticle size was measured using dynamic light scattering, indicating size in nm when measured by intensity. **b)** JOC-LD conjugate was run on an SDS-PAGE gel with (B/R) or without (UB/UR) boiling and reduction, stained with Coomassie blue and silver stain.

JOC-LD retains DSG2-binding and cytotoxic capabilities of its components

To test whether the JOC-LD conjugate retained properties unique to each of its components - DSG2 binding for JOC-x and cytotoxicity for liposomal doxorubicin - we started by using a viral competition assay to measure DSG2 binding. This viral competition assay tests whether a JO or JO derivative protein is able to compete with native adenovirus-3 for surface DSG2 binding by co-incubating JOC-x with a GFP-expressing adenovirus 3 in HeLa cells. JOC-x was able to prevent entry of GFP-Ad3 and suppress GFP levels consistent with the ability to efficiently bind DSG2(160). Upon incubation of JOC-LD with GFP-Ad3, a decrease in GFP expression was observed, although at higher concentrations compared to JOC-x indicating slightly less efficient binding possibly due to steric hindrance caused by the association with large liposomes (Figure 2a).

To test the efficacy of the doxorubicin component which should kill tumor cells, an alamar blue cytotoxicity assay was used: JOC-LD was incubated with T84 cells, a colon adenocarcinoma-derived cell line that also maintains tight junctions, to look for inhibition of cell growth over time. JOC-LD retained cytotoxicity at similar levels as doxorubicin, resulting in decreased fluorescence of the reduced alamar blue product being seen with higher concentrations of JOC-LD (Figure 4-2b), at a comparable concentration compared to doxorubicin alone. This potentially is due to the ability of the JO component to sensitize the cells to doxorubicin by disrupting the tumor tight junctions in this model.

a)

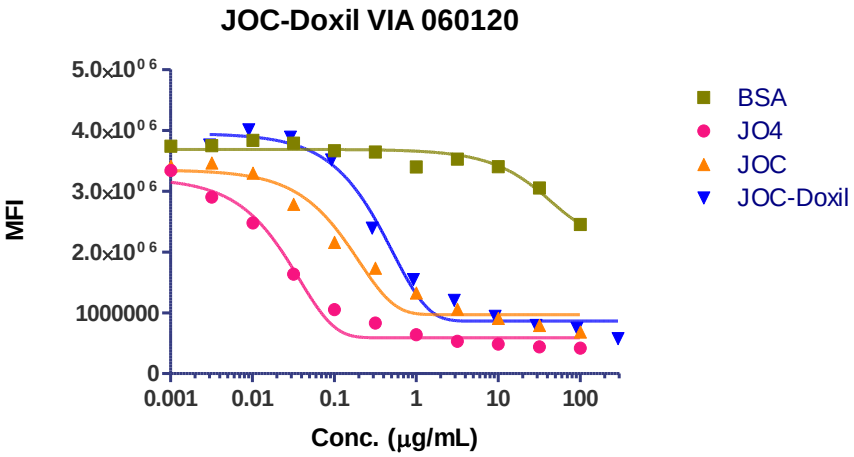

	EC50 (ug/mL)
JO4	0.02
BSA	5.41E+16
JOC	0.197
JOC-Doxil	0.339

b)

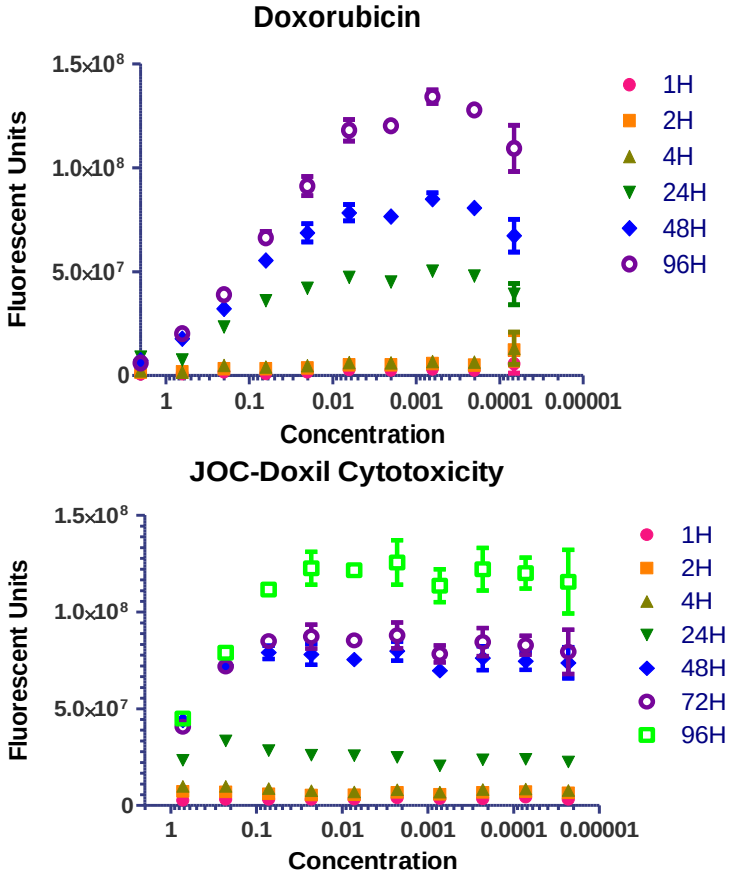

Figure 4-2 DSG2-binding and cytotoxic properties of JOC-LD conjugate.

a) JOC-LD conjugate was measured for DSG2 binding by competition with native Ad3 in a viral inhibition/competition assay in HeLa cells. EC50 values of inhibitory concentrations are shown in the table. **b)** JOC-LD and small molecule doxorubicin were used in cell cytotoxicity assays using Alamar Blue in T84 cells. Fluorescence measurements were taken at the indicated time points, where increasing fluorescence means increased cell survival and proliferation.

Localization of JOC-Doxil conjugate in tissue

To investigate where the JOC-LD localizes to in tissue, DSG2-trangenic mice were injected with JOC-LD and tissues of note were taken for histopathological analysis. In previous studies, JO was noted to concentrate in the liver, kidneys, and lungs. Immunofluorescent staining for JO and DSG2 showed presence of JO in lungs, kidneys, spleen, and liver. JO co-localized with DSG2 in the lungs, liver and kidney, while DSG2 was sparsely expressed in the liver (Figure 4-3). The detection of JO and its specific homing to DSG2 indicates that the JOC-Doxil retains its targeting to DSG2 *in vivo*, and can be thus expected to have the same properties of JO in targeting DSG2 and opening tight junctions, with the added advantage of a conjugated PLD payload to kill the tumor. This results in more simple administration protocols for the patient, and by enhancing the sensitivity of the tumor and specificity of the therapy should increase safety while also increasing therapeutic efficacy.

DAPI DSG2 JO Overlay

Kidney

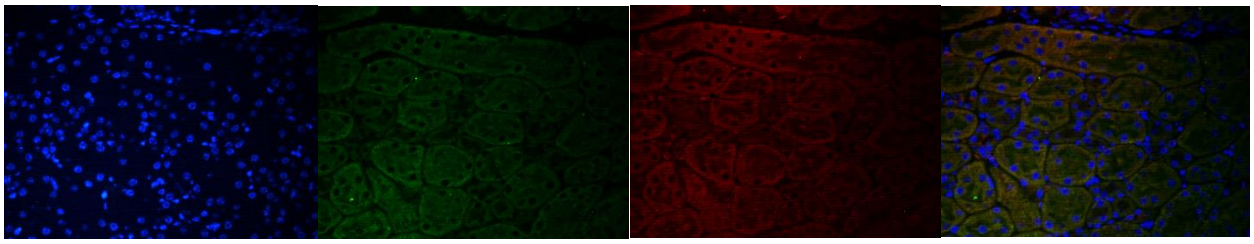

Liver

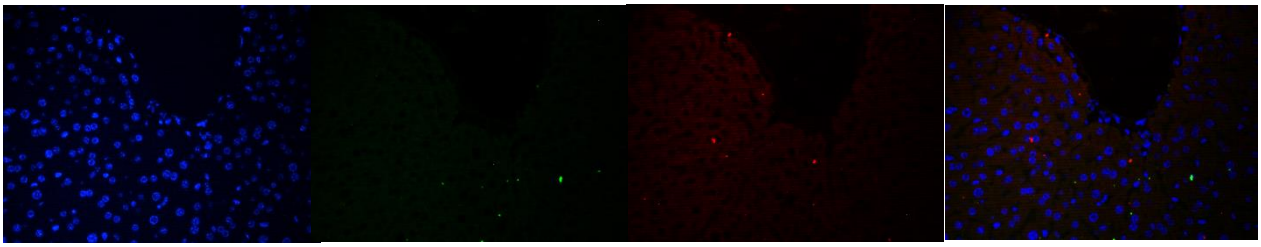

Lung

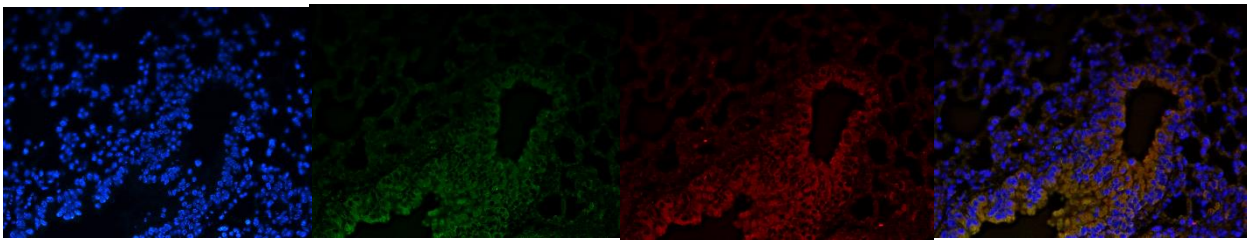

Spleen

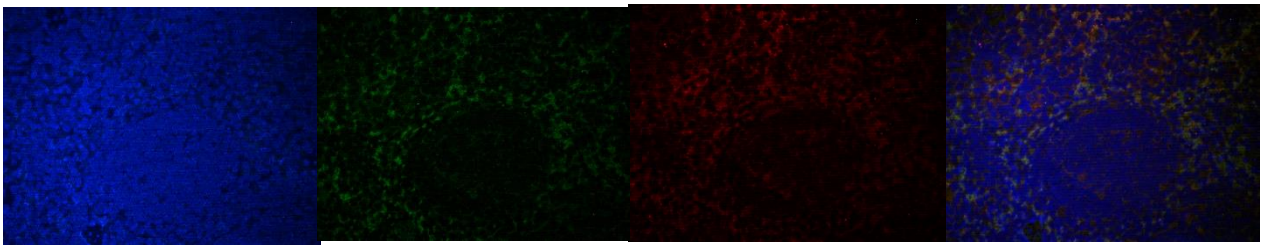

Figure 4-3 Localization of JO in DSG2-transgenic mice tissue

Tissues were taken from DSG2-transgenic mice 24 hours after administration of JOC-LD at 2 mg/kg equivalent of doxorubicin. Tissues were frozen in OCT before sectioning and staining for DSG2 and anti-Ad3 knob. Slides were examined under a Leica DM100 microscope with fluorescent filters.

In vivo efficacy of JOC-LD against xenograft cancer models

JO has already been demonstrated to enhance therapy when co-administered with Doxil® or other therapies such as monoclonal antibodies. To confirm whether JOC-LD could have an enhanced effect over Doxil® alone *in vivo*, we tested the conjugate in a mouse xenograft cancer model. CB17 immunodeficient mice bearing T84 human xenograft colon adenocarcinoma cells were given JOC-LD, Doxil® or separate "JO mixed with Doxil®" administrations upon reaching a tumor size of 100 mm^3, and allowed to grow until 1000 mm^3 when they were sacrificed (Figure 4-4a). Mice that received JOC-LD consistently had the lowest average tumor size, and had a survival which was significantly longer than either the control group or the Doxil® only group ($p<0.0001$ and $p=0.0171$ respectively), and efficacy was comparable with the separate JO+Doxil® administration while superiority there was not clearly established (Figure 4-4b). The JOC-LD group had a median survival of 66 days, compared to 33 and 50 for control and Doxil® ($p<0.0001$ against control, $p=0.0171$ against Doxil®). Of note, 4 out of 10 mice in the JOC-LD were considered cured, with no tumor tissue observed for over 8 weeks whereas none of the other groups involved demonstrated cures (Figure 4-4c).

Thus, JOC-LD shows superior efficacy in a xenograft cancer model in mice compared to Doxil® alone, and comparable efficacy as the separate combination of JO and Doxil®.

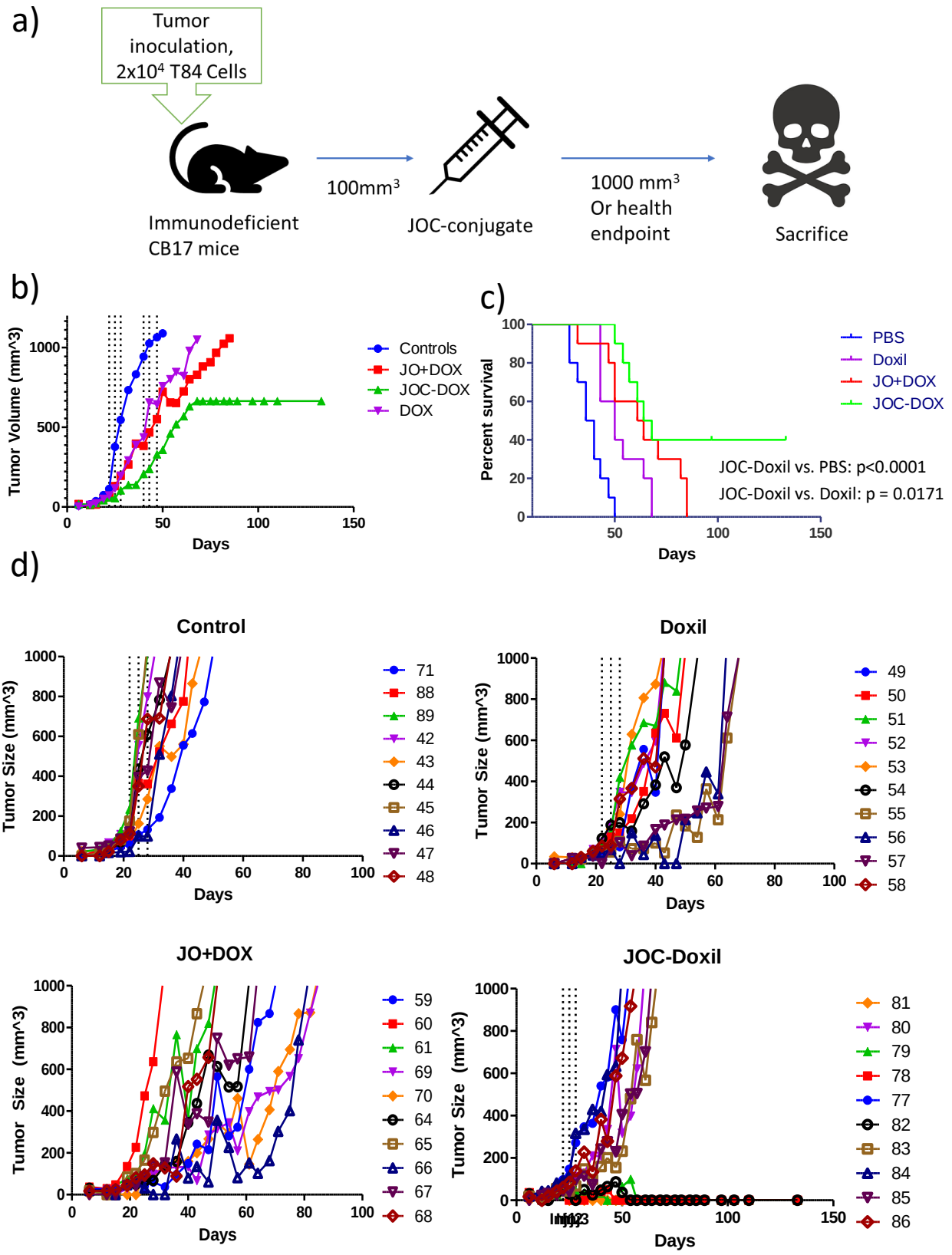
a)
Tumor inoculation, 2x10⁴ T84 Cells
Immunodeficient CB17 mice
100mm³
JOC-conjugate
1000 mm³ Or health endpoint
Sacrifice
b)
Tumor Volume (mm^3)
Days
Controls
JO+DOX
JOC-DOX
DOX
c)
Percent survival
Days
PBS
Doxil
JO+DOX
JOC-DOX
JOC-Doxil vs. PBS: p<0.0001
JOC-Doxil vs. Doxil: p = 0.0171
d)
Control
Doxil
JO+DOX
JOC-Doxil
Tumor Size (mm^3)
Days

Figure 4-4 Xenograft model testing of JOC-LD anti-tumor efficacy in mice

a) *in vivo* experiment plan of T84 cell xenografts. Mice were implanted with tumor cells before injection of JO, Doxil®, JO+Doxil® separate combination, or JOC-LD conjugate. Tumors were allowed to grow to 1000 mm^3 before sacrifice. **b)** average tumor sizes in each treatment group over time **c)** survival curves of each treatment group. **d)** individual tumor sizes of each animal in indicated treatment group are shown.

4.5 Discussion

Epithelial cancers are characterized by the presence of a highly structured milieu which serves the function of feeding and protecting the tumor. One way of protection is the use of physical barriers, and the JO protein aims to address this problem in treatment of solid tumors. JO has already been noted to significantly enhance conventional therapies such as Doxil® and monoclonal antibodies in previous research (64, 161, 162), thus indicating its potential to enhance efficacy and delivery. The JO protein has properties which make it an enticing co-therapeutic: homing to tumor DSG2 and the ability to open tumor tight junctions. The creation of a conjugatable version of JO, JOC-x, opened a new path to increasing efficacy of co-therapeutics by directly conjugating a therapeutic payload to JOC-x.

In this chapter, I explored the conjugation of JOC-x to a chemotherapeutic payload, PEGylated Liposomal Doxorubicin, which was successfully accomplished. The conjugated product, JOC-LD, retained its properties of its individual components JOC-x and PLD: DSG2 binding and tumor cytotoxicity, respectively. The full conjugate had the expected increase in nanoparticle size and retained conjugation of JOC after liposomal destruction. Furthermore, it was noted that the JOC-LD tended to co-localize with DSG2 when administered in DSG2-transgenic mice, thus indicating that overall, JOC-LD is properly able to carry out its functions *in vitro* and *in vivo.* In tumor efficacy *in vivo* tests, JOC-LD resulted in impressive efficacy, resulting in slower growth and survival of mice implanted with xenograft tumors, at a level superior to that of PLD alone and the separate combination of JO + PLD. The 40% cure rate of mice of tumors seen in the JOC-LD group was previously unseen in any mouse tumor trials involving JO, PLD, or a combination thereof, further attesting to the improved efficacy of the whole conjugate in comparison to its constituent components.

The conjugation process of JOC-x to PLD was routine, through the use of a sulfhydryl-maleimide linkage, which is widely in use to conjugate proteins and antibodies (164). The incorporation of such a conjugation mechanism into liposomal formulations is not new, having been used to conjugate PLD (165) and liposomal chelators (166) to targeting molecule, increasing specificity and homing. Another approach to a two-component is pre-targeted therapy making use of bispecific antibodies targeting cancer antigens followed up by therapies (including radiotherapy or conventional therapeutics) (167). JOC-LD in comparison to these has the additional benefit of tight junction and therapeutic penetration, and such a construct has not been previously explored to our knowledge.

Although the successful production of JOC-LD and its efficacy in tumor models remain promising, the further use of JOC-LD in clinical models will require more biophysical characterization and consistent production. The maleimide-activated PLD is readily available and highly standardized to provide consistent reaction with JOC-x, and the reaction mechanism is commonplace in bioconjugate chemistry (168). However, the JOC-LD product may require more characterizations to ensure batch-to-batch consistency, ensuring consistency in parameters such as nanoparticle size, JOC-to-PLD ratio, and DSG2-binding affinity. The *in vivo* efficacy of JOC-LD can be further ascertained in multiple models of cancer by using xenografts of different cell lines, including other solid tumors such as ovarian cancer and lung cancer. As with any new formulations of existing therapeutics (of either JOC-x or PLD), separate pharmacokinetic and pharmacodynamic studies must be carried out to further explore the use of JOC-LD as a therapeutic candidate in human cancer.

Overall, the successful bioconjugation of JOC to PLD poses an exciting prospect, as a new therapeutic formulation that holds multiple advantages in administration and efficacy. Further

exploring the JOC-LD conjugate and testing its potential to enhance existing therapies could eventually result in a powerful therapeutic, to be used against not only colon or ovarian cancers but broadly against solid tumors.

4.6 Acknowledgements

This work was done with assistance from Sean Gray (setting up the Malvern Zetasizer), Sucheol Gil (procuring mice and animal experiments), and Jenn Bergthold (Assisting with the viral inhibition assay setup).

Chapter 5 IMMUNOGENIC AND PHARMACOKINETIC PROFILES OF JO AND DOXIL IN *MACACA FASCICULARIS*

5.1 Abstract

Liposomes are extensively used as amphiphilic nanoparticles capable of delivering a variety of payloads including chemotherapeutics and genetic information. Therapeutic liposomes often contain polyethylene glycol (PEG) on the surface for the purposes of chemical stabilization and cargo conjugation. While traditionally thought to be non-immunogenic, some previous studies indicate the possibility of PEGylated liposomes triggering an immune response and enhanced clearance.

We investigated the immunogenicity and toxicity profiles of Doxil®, a PEGylated nanoparticle containing doxorubicin, in combination with an experimental recombinant adenovirus-3 protein, Junction Opener (JO). JO may offer clinical benefits in cancer patients as it enhances penetration of therapeutics and immune cells into a solid tumor by compromising its tight junctions. The combination of Doxil® and JO was tested in *Macaca fasciularis* in a series of four injections (4 weeks apart) with and without immunosuppression, as immunogenicity may result from both the liposomal formulation and the recombinant adenoviral JO protein. We found that while antibody levels to JO increase upon administration, this does not lead to anaphylactic shock and response is characterized by a transient leukopenia. The anti-JO response was sufficiently suppressed by cyclophosphamide/steroid pre-treatment. As for Doxil®, no detectable IgM or IgG antibodies to PEG were found. The Doxil® clearance half-life was approximately three days. No changes in electrocardiograms were observed in response to Doxil® or JO. No toxic reactions to Doxil® were noted at the dosage (40mg/m^2) used throughout the duration of the experiment. With the widespread use of liposomal formulations of gene and chemotherapeutic delivery, it seems that

PEGylation does not trigger additional immune response. The combination of the Doxil® and JO may be used safely in clinical settings if development of anti-JO4 antibodies is suppressed.

5.2 Introduction

The Junction Opener protein (JO) was developed from adenovirus subtype 3 and has demonstrated transiently opening tight junctions by binding DSG2, a desmosomal junction protein (64). Ad3 binds DSG2 as its cellular receptor, and engineering and enhancement of its fiber knob resulted in a tightly binding JO protein, with the most optimal variant, JO-4, having a K_D of 0.58 nM (160). When co-administered with monoclonal antibodies such as trastuzumab or chemotherapeutics such as PLD, JO shows enhanced efficacy of these drugs in human tumor xenograft mouse models (162). JO also shows efficacy when combined with oncolytic adenoviruses, as demonstrated by the Lieber Lab when oncolytic Ad35 and Ad5 were used in conjunction with JO resulting in longer survival and cure rates up to 80% (161). The use of JO as a co-therapeutic thus holds much promise in the treatment of cancers, and has accordingly been extensively researched for its potential benefits.

Doxorubicin, commonly referred to as Adriamycin, has a history of being used in multiple types of cancer and conditions since its discovery in the 1950s (169). It is currently indicated for cancers of the breast, ovary, prostate, stomach, thyroid, small cell lung cancer, liver, squamous cell cancer, Hodgkins, and numerous other types of cancers (170). The powerful antitumor activity of doxorubicin is attributable to its inhibition of DNA topoisomerase II and DNA intercalation, causing impairing cell replication and triggering apoptosis (171, 172). It is commonly included in major regimens for Non-Hodgkin's Lymphoma (CHOP), Hodgkin's Lymphoma (ABVD), breast cancer (TAC), and platinum-resistant ovarian cancer (CD, Carboplatin and Liposomal Doxorubicin)(173). However, doxorubicin has well-characterized

side effects, prominently featuring cardiotoxicity. Increasing doses of doxorubicin may result in dilated cardiomyopathy, resulting in the heart chambers enlarging, leading to heart failure and death (174).

Liposomal formulations of doxorubicin have been used extensively due to their favorable biodistribution, drug targeting, and decreased side effects (175). PEGylated liposomal doxorubicin (PLD) is marketed under the names Doxil®, Caelyx® or Lipodox®. The liposomal formulation is formed of a polyethylene glycol (PEG) coat on the exterior with an amphipathic liposomal bilayer underneath. The core is comprised of an aqueous solution of doxorubicin for release once the liposome reaches its intended target. The size of the liposome is approximately 100 nm, which precludes it from capillary junctions such as those found in the heart, further decreasing the possibility of cardiotoxicity and fatal side effects (176). As such, PLD has been approved for use in platinum-resistant ovarian cancer, multiple myeloma, and AIDS-associated Kaposi's sarcoma (177). It represents the first generation of nanoparticle-based therapy and is still widely used today, with the liposomal doxorubicin market value at approximately $400 million in the United States as of 2015 (178).

The transition of a treatment candidate from a xenograft mouse model to human clinical trials poses multiple problems, including immunogenicity and toxicity. JO, in its essence, is a viral protein derived from Ad3 and a large population harbors pre-existing immunity to Ad3 (179). However, preliminary evidence suggests that JO does not trigger immunopathological symptoms in animal models(162). PLD has fewer side effects when compared to doxorubicin, but the problem remains nonetheless: hematological side effects such as thrombocytopenia, leukopenia, and anemia can occur in up to 49% of patients. Hand-foot syndrome (Palmar-plantar erythrodysesthesia, PPE) occurs in approximately 18% (180). The immunogenic effects of PLD

are not as clear, especially the potential of its PEG coat to stimulate an immune response. PEG is ubiquitous in society with uses in cosmetics and lubricants; oral consumption occurs through processed foods and drug formulations. PLD-mediated immunogenicity to PEG therefore potentially presents a significant problem to patients receiving therapy.

In this chapter, I explore the potential of JO in combination with PLD to cause critical immunogenicity and/or toxicity in *M. fascicularis*, to ascertain the suitability of JO for ovarian cancer clinical trials in humans. As JO immunogenicity has already been previously noted(163), a common immunosuppression regimen is added to ascertain whether the immune response can be suppressed to acceptable levels. The ability of PLD to cause an immunogenic response to its PEG coat is also assessed. Data obtained suggests that immune response to PEG is undetectable with multiple administrations of PLD. However, antibody responses to JO increase with each subsequent round of injections resulting in immune complexes and the elevation of inflammatory cytokines, but this is suppressed by the immunosuppressive regimen.

5.3 Materials and Methods

Animals. Female *M. fascicularis* were obtained from Altasciences Inc. (Everett, WA, USA) and housed in the Washington National Primate Research Center (WaNPRC) on the University of Washington campus. Animals were housed, fed, and conditioned according to established ethics and protocol, under IACUC Protocol #3108-03. JO and Doxil® were filtered through 0.2 um filters before administration into the arm vein of sedated animals. Upon completion of study, animals were sedated before euthanasia and extraction of organs for histological analysis.

Proteins. JO was produced in *E. coli* and sourced from Gennova Pharmaceuticals Ltd (Pune, India), and confirmed to contain acceptable endotoxin levels (<200 EU/mL). Doxil® was sourced from the University of Washington Medical Center, manufactured by Dr. Reddy's

Laboratories (Hyderabad, India). Methylprednisolone, dexamethasone, ceftazidime, acyclovir, cyclophosphamide (Cytoxan®), and Mesna™ were obtained from the University of Washington Medical Center, in generic forms. JO was injected at the concentration indicated per animal. Doxil® was dosed at 40 mg/m^2, using a conversion factor for surface area in m^2 = (sqrt(Height in cm*Weight in kg))/60. Drugs were diluted in physiological saline immediately prior to administration.

Antibodies. Anti-JO antibodies were raised in rabbits and in mice and polyclonal serum was used to detect specifically against JO. DSG2 antibodies were obtained from Invitrogen (Carlsbad, CA, USA). Anti-PEG antibodies (AGP6, AGP7) were kindly provided by Dr. Steve Roffler (Academica Sinica, Taipei, Taiwan).

Preparation of tissues for ELISA

100 milligrams of tissue or organ in PBS-0.05%Tween20 were homogenized using the TissueRuptor system (Qiagen), sonicated for 20 seconds, and subjected to three freeze-thaw cycles. Cell debris was spun down and supernatants from lysed tissues were used in the JO-4 and Doxil ELISA at 1:5, 1:20, and 1:100 dilutions.

JO Antibodies Detection by ELISA

Animal blood obtained in serum separation tubes (SST) at the indicated time points were centrifuged at 5000 RPM for 10 minutes, after which the supernatant was kept at -20°C before use. ELISA plates were coated with JO protein (0.3 ug per well) at 4°C overnight then blocked with 5% non-fat milk for 1 hour. Serum or tissue homogenate serial dilutions (starting at 1:50, 3x subsequent dilutions) were added for 1 hour. After washing, HRP-conjugated secondary antibodies against NHP IgG or IgM (Invitrogen PA1-84631 and 62-6820 respectively) were plated at 1:10,000 for 1 hour. After wash, Thermo 1-Step Ultra TMB Solution (ThermoFisher

Scientific) was added and the color was allowed to develop for 7 minutes before stopping with 2N sulfuric acid. Absorbance readings at 450 nm were taken with a plate reader. Antibody reactivity curves were plotted with Graphpad Prism with a 4-parameter curve, and EC50 values were accordingly calculated.

JO ELISA

The ELISA consisted of a polyclonal rabbit antibody directed against the Ad3 fiber knob as capture antibody and a mouse monoclonal anti-Ad3 fiber knob antibody (clone 2-1) or a monoclonal mouse anti-JO antibody as detection antibody, using the common ELISA protocol as stated above, incorporating a standard curve using the JO protein at concentrations ranging from 100 ng/mL to 0.0064 ng/mL. The sensitivity of the ELISA was 0.5 ng/ml.

Detection of Doxil Concentration in Serum by ELISA

For Doxil detection, plates were coated with anti-PEG antibodies (AGP6, 250ng per well) overnight at 4°C. Plates were then blocked with 5% non-fat milk for 1 hour, and serum dilutions were added after washing (starting at 1:10, 10x subsequent dilutions) and incubated at room temperature for 1 hour. This was followed up by another, different specificity anti-PEG antibody (15-2B-Biotin) and incubated for 1 hour. After wash, HRP-streptavidin (Jackson ImmunoResearch #016-030-084, West Grove, PA, USA) was added to wells at 0.5 mg/mL and incubated for 1 hour. Plates were developed by adding Thermo 1-Step Ultra TMB Solution (ThermoFisher Scientific) and color was allowed to develop for 15 minutes before stopping with 2N hydrochloric acid. Doxil standard concentration curves were generated using a 4-parameter curve with GraphPad Prism and were used as comparison to determine Doxil concentrations in serum.

DSG2 Immunofluorescence

Organs were placed in optimal cutting temperature compound (OCT, Sakura Finetek, Torrance, CA, USA) and flash frozen in liquid nitrogen. Sections were sliced at 6 μm thickness at the Histology Unit at the University of Washington. OCT sections were thawed and fixed in 5% paraformaldehyde at room temperature for 15 minutes. Slides were then blocked and permeabilized in 5% non-fat milk in 0.05% Tween-20 PBS overnight at 4°C. After washing, the slides were incubated in the primary antibody diluted in 2% non-fat milk/PBS for 1 hour, followed by the secondary antibody diluted in 2% non-fat milk/PBS for 1 hour. Slides were then mounted using VECTASHIELD Antifade Mounting Medium with DAPI (Vector Labs, Burlingame, CA, USA) before visualization using fluorescent filters under a Leica xx microscope. Images were overlaid using ImageJ software (NIH, Bethesda, MD, USA).

The following antibodies were used on 4% para-formaldehyde-fixed OCT sections of monkey organ/tissue: anti-HAdV3 fiber knob mAb- clone 2-1; goat-α-human DSG2 (AF947, R&D Systems), mouse-α-CD163 (Biolegend #333602) with the secondaries as follows: Alexa-Fluor 594 conjugated chicken anti-rabbit IgG (Invitrogen A-21442), Alexa Fluor 488-conjugated donkey anti-goat IgG (Abcam #6881), and Alexa Fluor 488-conjugated goat anti-mouse IgG (Biolegend #405319).

Cytokine Flow Cytometry Panel

Animal serum was taken and were assessed for inflammatory cytokines (Th1/Th2) using the Non-human Primate Th1/2 cytokine kit, Cytometric Bead Array (CBA) (BD Biosciences, San Jose, CA, USA). Flow data were obtained using a BD LSR II flow cytometer. Results were quantified using BD CBA FCAP Array Software.

5.4 Results

Junction Opener and medication are well tolerated

Two *M. fascicularis* were given administration of medication and doses as outlined in Figure 5-1, receiving medication over a span of 16 weeks before euthanasia. The primary difference between the two regimens were that one animal (Animal #1) received immunosuppression in the form of cyclophosphamide and steroids prior to JO and Doxil® administration, while the other did not (Animal #2). Doxil® and JO administrations were given at days 0, 28, 62, and 84, and cyclophosphamide was administered 2 days before each of the JO+Doxil® injections (Table 5-1). Both animals tolerated medication well and did not show overt symptoms of distress or serious discomfort throughout the procedure. Minor nausea and vomiting were noted during the injections, but the macaques were in good health overall and did not display significant weight loss. Daily monitoring of food intake, infusion site appearance, feces/urine, food and water did not show any abnormalities. Electrocardiograms (ECG) were taken prior to each injection of JO+Doxil and results were normal (results not shown).

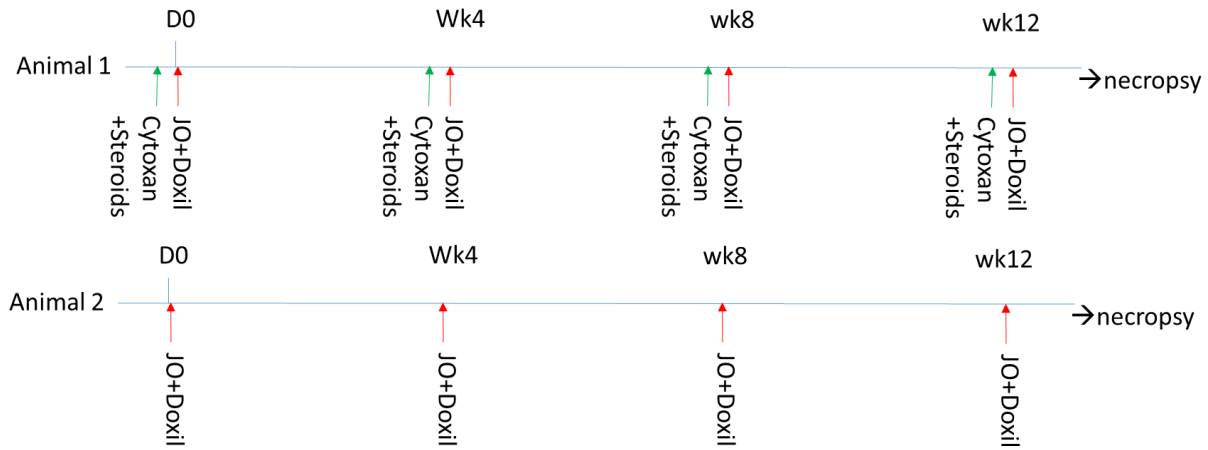

Figure 5-1 Medication regimen plans for 2 *M. fascicularis macaques.*

Experimental monkey (#1) was given Cytoxan 2 days before JO+Doxil® injection, followed shortly by steroids, in the form of methylprednisolone and dexamethasone. Control animal (#2) was given only JO and Doxil. Dosages: JO, 2 mg/kg, Doxil, 40 mg/m^2. Animals were consistently monitored for toxicity or adverse changes in health.

Table 5-1 Drug Administration Regimen of Animal #1

N.B. Animal #2 received only the JO and Doxil® administrations as indicated.

Day, Hour	Drug	Dosage
-2	Cytoxan	50.2 mg/kg
0, -0.5 H	Methylprednisolone	5.2 mg/kg
	Dexamethasone	2 mg/kg
0	JO	2 mg/kg
0, 1 H	Doxil®	40 mg/m^2
26	Cytoxan	50.2 mg/kg
28, -0.5 H	Methylprednisolone	5.2 mg/kg
	Dexamethasone	2 mg/kg
28	JO	2 mg/kg
28, 1H	Doxil®	40 mg/m^2
60	Cytoxan	50.2 mg/kg
62, -0.5H	Methylprednisolone	2 mg/kg
	Dexamethasone	2 mg/kg
62	JO	2 mg/kg
62, 1H	Doxil	40 mg/m^2
82	Cytoxan	50.2 mg/kg
84, -0.5H	Methylprednisolone	2 mg/kg
	Dexamethasone	2 mg/kg
84	JO	2 mg/kg
84, 1H	Doxil	40 mg/m^2
84, 4H	***Euthanasia***	

JO Pharmacokinetics

Of primary interest was the pharmacokinetics of JO and its clearance from serum after injection. JO kinetics were assessed through an ELISA. At the first injection, JO reached a serum concentration of around 800 ng/mL in both animals when detected by rabbit anti-Ad3 knob, or 500-2000 ng/mL when detected by mouse anti-JO (Figure 5-2a, b). JO was quickly cleared from serum with concentrations becoming undetectable (<50 ng/mL) by about 6 hours after injection (Figure 5-2c). With subsequent injections, the peak concentrations gradually decreased, at approximately 50 ng/mL at 1 hour post-injection. Half-life of JO in serum was calculated to be around 5 hours for both animals (Table 5-2), and clearance was 0.325 L/h/kg and 0.338 L/h/kg for animals #1 and #2 respectively. No significant differences in these parameters between animals #1 and #2 were noted, indicating the immunosuppression did not seem to have a discernible effect on JO persistence in serum and clearance. The pharmacokinetics of JO indicated a faster-than-expected clearance, with serum concentration becoming undetectable within a day. JO was detected in urine at necropsy, 2 hours after the last administration of JO+Doxil®, at a concentration of 1.15 ng/mL and 1.37 ng/mL for animals #1 and #2 respectively.

a)

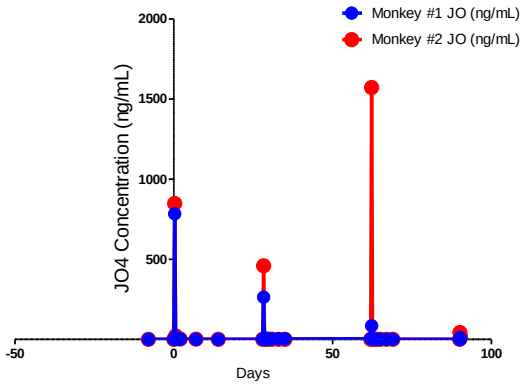
Monkey #1 JO (ng/mL)
Monkey #2 JO (ng/mL)
JO4 Concentration (ng/mL)
2000
1500
1000
500
-50
0
50
100
Days

b)

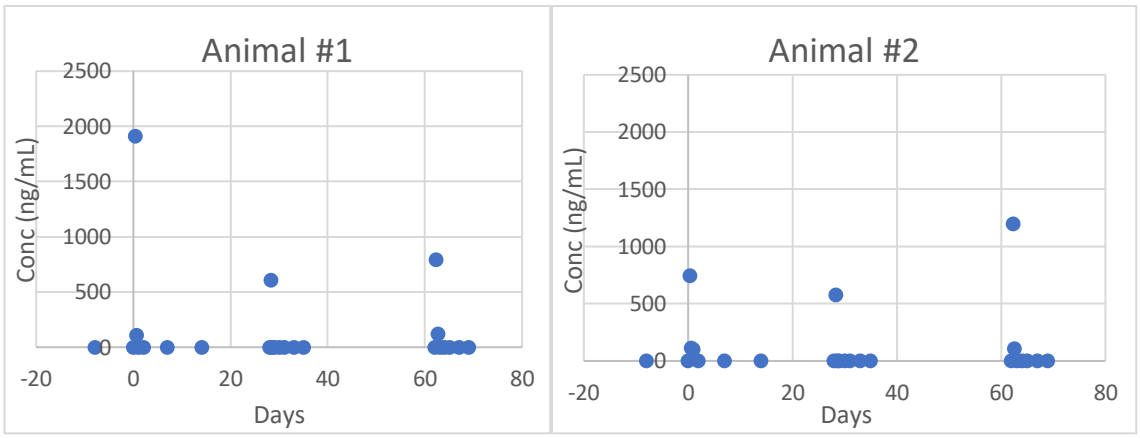
Animal #1
Conc (ng/mL)
2500
2000
1500
1000
500
0
-20
0
20
40
60
80
Days
Animal #2
Conc (ng/mL)
2500
2000
1500
1000
500
0
-20
0
20
40
60
80
Days

c)

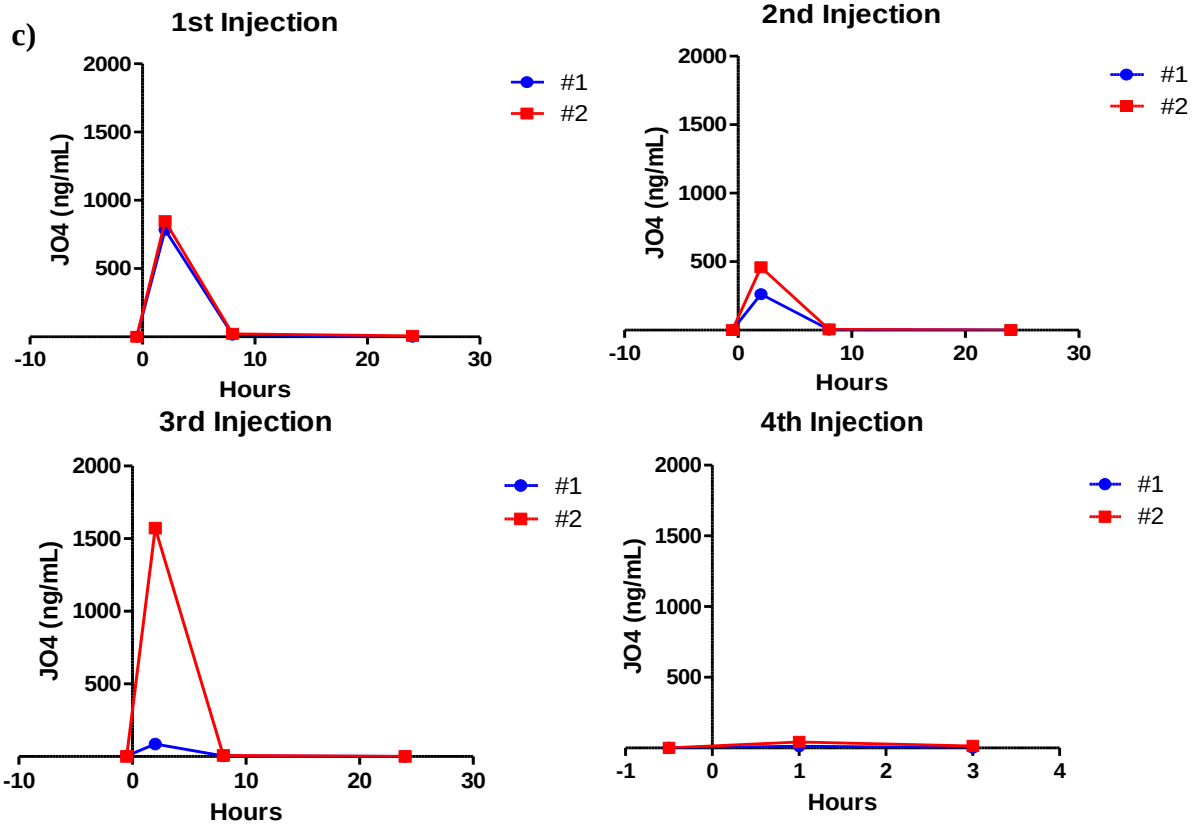
1st Injection
JO4 (ng/mL)
2000
1500
1000
500
-10
0
10
20
30
Hours
#1
#2
2nd Injection
JO4 (ng/mL)
2000
1500
1000
500
-10
0
10
20
30
Hours
#1
#2
3rd Injection
JO4 (ng/mL)
2000
1500
1000
500
-10
0
10
20
30
Hours
#1
#2
4th Injection
JO4 (ng/mL)
2000
1500
1000
500
-1
0
1
2
3
4
Hours
#1
#2

Figure 5-2 Pharmacokinetics of JO in monkey serum detected by ELISA.

Monkey serum was taken at selected time points and JO concentration was determined using **a)** an anti-Ad3 knob rabbit polyclonal antibody and an HRP-conjugated anti-rabbit secondary. **b)** a different pair of antibodies, an anti-JO mouse antibody and HRP-conjugated anti-mouse secondary was used to determine JO4 concentration. The fourth injection was not analyzed using the anti-JO antibody due to reagent shortage. **c)** zoomed in JO4 concentration at each injection round from the results using rabbit anti-Ad3k, in hours. Injection #4 was followed by necropsy within 3 hours, which was the last time point at which serum was taken and processed.

Table 5-2. Pharmacokinetic parameters of JO in macaque serum, 1st cycle

Value	Animal #1	Animal #2
Peak concentration (1st peak)	784 ng/mL	848 ng/mL
Clearance	0.324 L/h/kg	0.338 L/h/kg
$t_{1/2}$ (1st peak)	5.46 hours	4.83 hours
Steady-state volume of distribution	2.551 L/kg	2.358 L/kg
Animal weight at 1st injection	3.2 kg	3.6 kg

Antibodies against JO

Due to the faster-than-expected clearance of JO from serum and the increasing speed of clearance with successive injections, we suspected antibody-mediated clearance could be behind JO elimination from serum. Antibodies against JO were detected by ELISA, and baseline IgM against JO seemed to be present, thus indicating some pre-existing immunity, likely to Ad3. Antibody titers spiked according to the injection dates, with titers becoming greater and greater with each subsequent injection (Figure 5-3). As expected, IgM titers increased the fastest, with spikes occurring as early as a few days after the first injection of JO and Doxil ®. IgG peaks occurred later, at about 14 days after the first injection. The antibody spiked higher with subsequent injections, and animal #2 which received no immunosuppression had a higher level of antibodies (both IgG and IgM) than animal #1 which had received an additional immunosuppressive regimen. By the 4th injection, animal #1 started to have comparable antibody spikes to animal #2, suggesting that the antibody levels sequentially increased. However, with the 4-dose regimen that was used in this study, the Cytoxan and steroid immunosuppressive regimen successfully suppressed anti-JO antibody levels compared to the control animal.

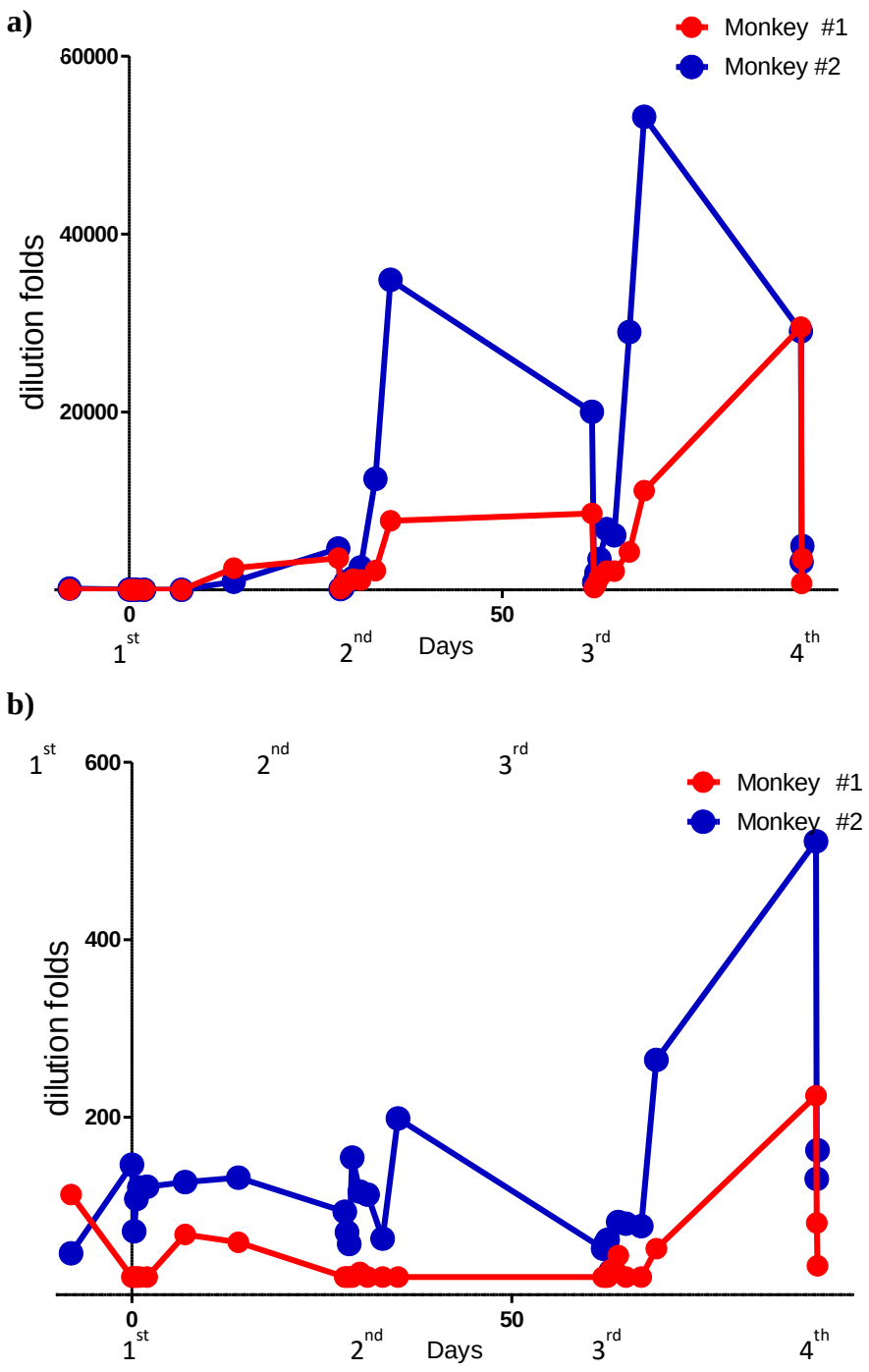

Figure 5-3 Antibody responses against JO in macaque serum.

Anti-JO4 antibody responses were detected by ELISA in monkey serum at indicated time points. Data points indicate EC50 of dilution titers as calculated through a 4-parameter non-parametric curve. **a)** IgG titers, **b)** IgM titers

Distribution of JO in tissues

Protein therapeutics tend to aggregate in the liver and adrenals, as found previously in an *in vivo* study investigating the biodistribution of a previous version of JO. Organs from necropsy of the animals were taken for detection of JO through ELISA and histopathology. Tissue lysates showed detectable JO in multiple organs, with highest levels being detected in the spleen and liver (Figure 5-4). Smaller amounts were detected in the adrenals, kidneys and lungs, lining up with previous results from another preclinical monkey study of JO (63).

Immunofluorescent detection of JO on tissues/organs where JO was detected indicated a general co-localization of JO with DSG2 expression when overlaid (Figure 5-5a). Of note was that DSG2+ cells in the bone marrow co-localized with JO, indicating a specific homing of JO to DSG2+ hematopoietic progenitor cells in the bone marrow. We found that JO in the liver did not seem to co-localize with DSG2; we thus suspected JO take-up by macrophages or Kupffer cells. Upon staining for JO and CD163, a macrophage marker, we found that JO could be detected to co-localize with CD163 (Figure 5-5b), thus indicating that in the liver, JO seems to mostly aggregate in macrophages or Kupffer cells, while in other organs, it homes to DSG2+ cells as expected.

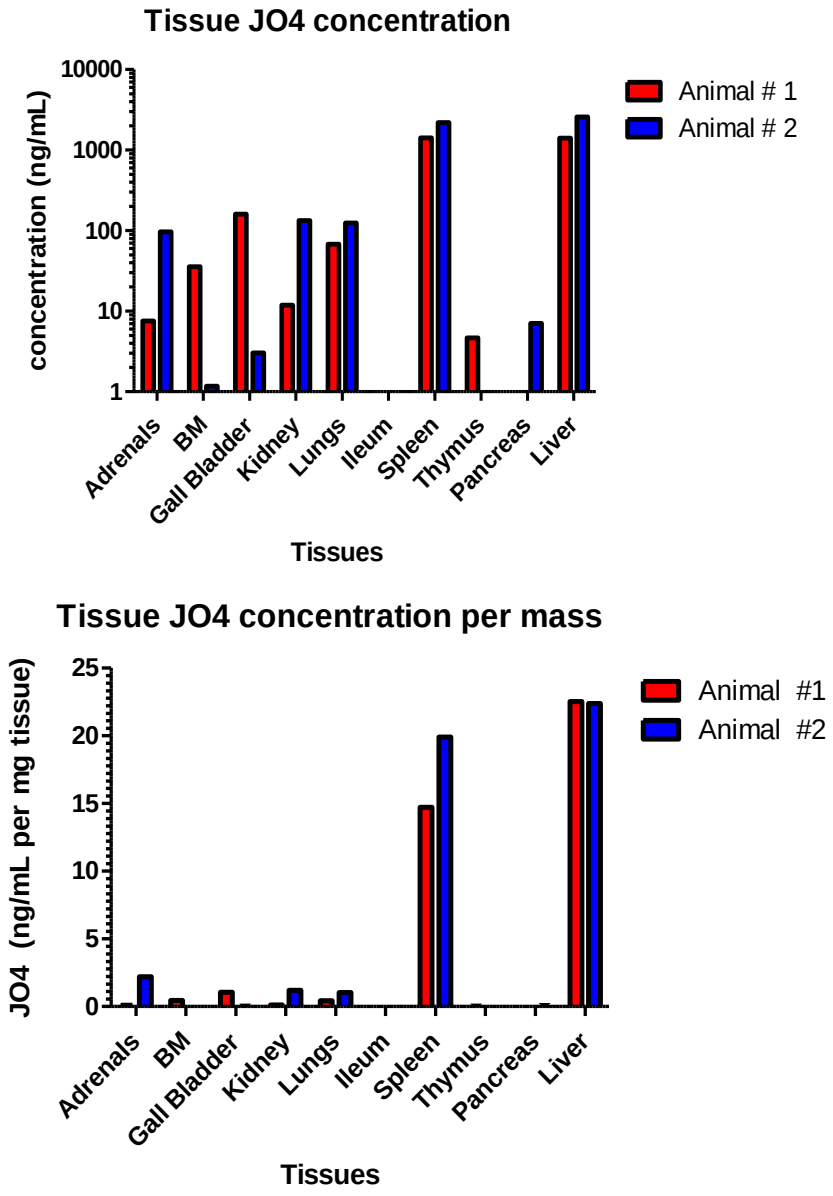

Figure 5-4 Presence of JO in macaque tissue.

Approximately 100 mg of tissue were ground into lysate for use in a JO ELISA. A total of 34 organs and tissues were analyzed for JO concentration. Only organs showing detectable levels of JO are shown in figure. Concentration of JO is shown as **a)** raw values or **b)** standardized by the mass of the tissue taken for lysate.

a)

DAPI DSG2 JO Overlay

Bone Marrow

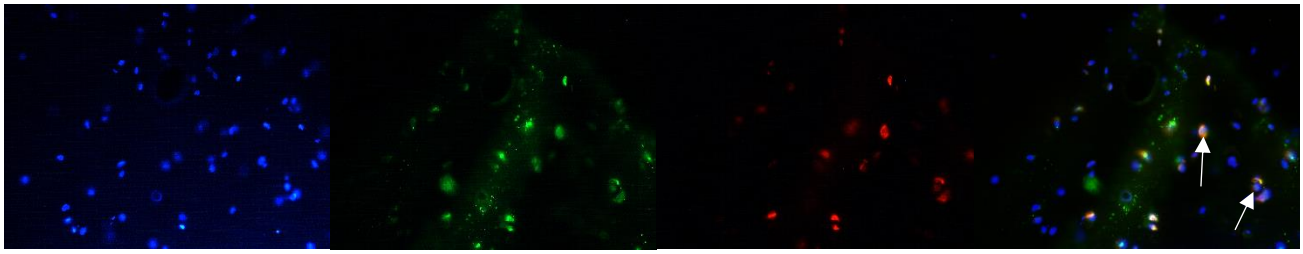

Liver

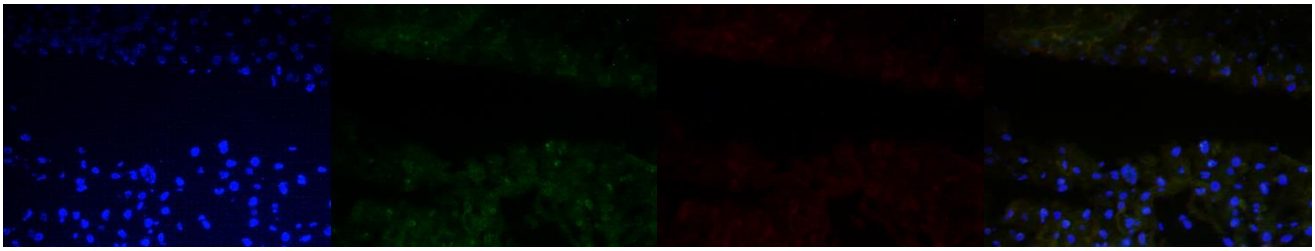

Lungs

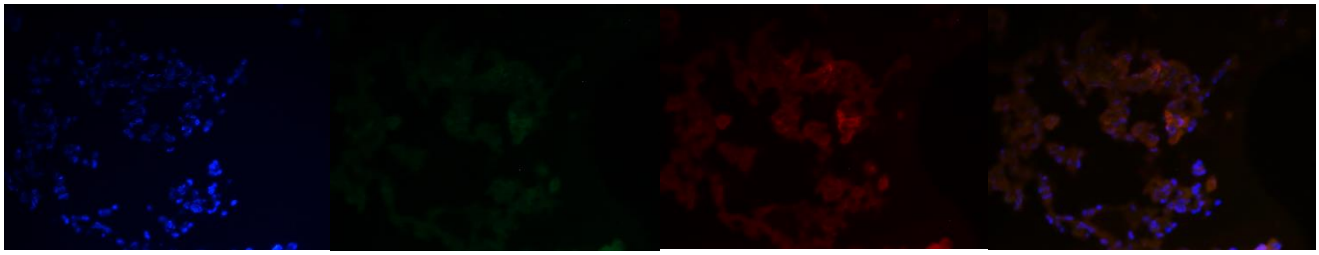

b)

DAPI CD163 JO Overlay

Liver

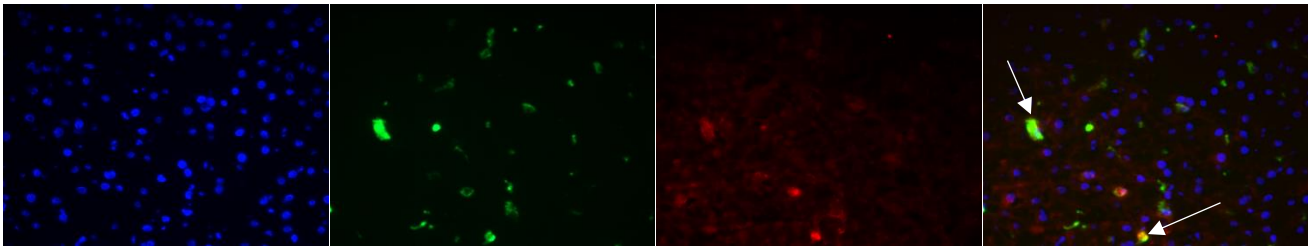

Lungs

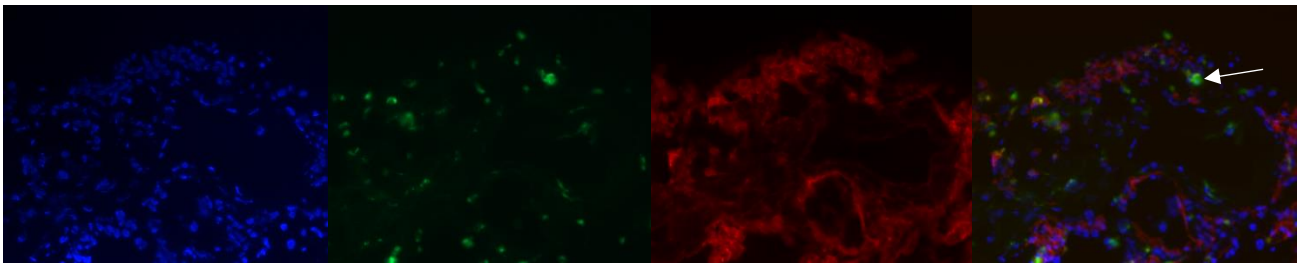

Figure 5-5 Immunofluorescent detection of JO in macaque tissue.

Organs and tissues were embedded in OCT before sectioning and staining for selected markers **a)** tissues stained for JO, DSG2, and overlay and **b)** stained for JO, CD163 (a macrophage marker), and overlay. Blue Filter: DAPI, VECTAmount reagent; Green Filter: Alexa Fluor 488 – conjugated secondaries, Red Filter: Alexa Fluor 594 – conjugated secondary antibodies. Overlays were generated using ImageJ.

Doxil® concentration and antibody response

The PLD administration was well tolerated at the clinically relevant dosage (40 mg/m^2). Doxil® concentration in serum was measured using an ELISA, making use of anti-PEG antibodies. Pharmacokinetics of the Doxil® in serum followed a typical peak within 2 hours of administration, declining until about day 14 when it was no longer detectable (Figure 5-6). There were no discernible differences between animal #1 and animal #2 in Doxil® kinetics, suggesting that the immunosuppression had no significant effect on the clearance of Doxil® from serum. Also, subsequent administrations did not increase clearance or decrease the peak concentration in serum, in a contrast to what has been seen with JO administration. Half-life of Doxil® in the serum was calculated to be 2.08 and 2.36 days for animal #1 and animal #2 respectively on the first administration. AUC were 10956 mg*h/L and 12557.87 mg*h/L for animal #1 and #2 respectively, averaging three curves (Table 5-3). When compared to publicly available parameters for Doxil®, clearance is a magnitude lower than in human patients (approximately 0.04 L/h/m^2). Peak concentration is also greater than in human clinical trial data, although this is expected as the Doxil® dosage used in macaques was different compared to the initial safety clinical data on its FDA label, which used doses of 10 mg/m^2 and 20 mg/m^2 for its preliminary studies (181), although the clinical doses of up to 50 mg/m^2 are now routinely used.

Notably, antibody responses against PEG were not detected in serum in either animal, thus suggesting that the administration of PLD does not trigger a humoral immune response and that PEG is well tolerated in an intravenous injection context.

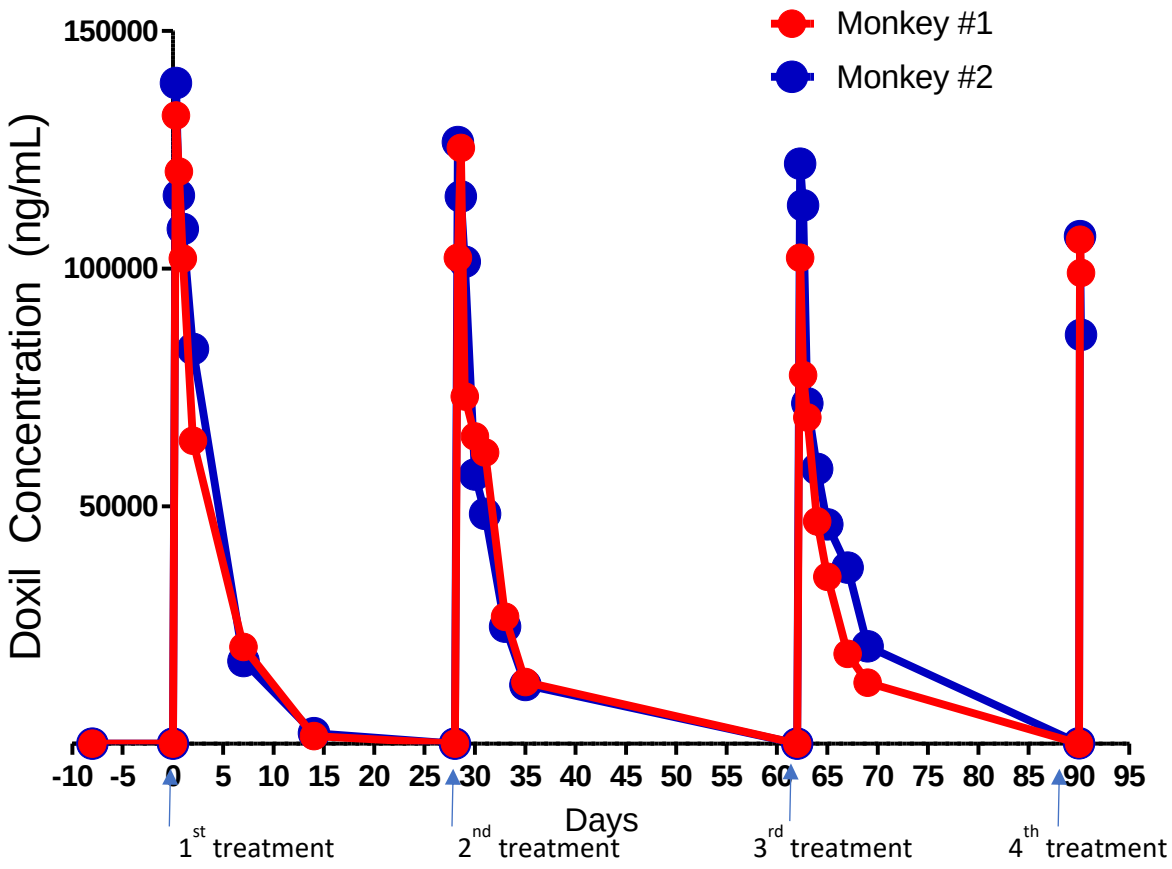

Figure 5-6 Doxil® concentration in macaque serum after receiving JO and Doxil®

Macaque serum was taken at indicated time points and an ELISA was performed for presence of Doxil® in serum. The ELISA involved coating with an anti-PEG antibody, followed by serum, and an HRP-conjugated alternate anti-PEG antibody for final detection. Concentration of Doxil® is given in ng/mL for both animals.

Table 5-3. Pharmacokinetic values of Doxil® in monkey serum, 1st cycle

Value	Animal #1	Animal #2
Peak concentration (1st peak)	132.17 ug/mL	138.99 ug/mL
Clearance	0.0042 L/h/m^2	0.0035 L/h/m^2
AUC (Average of Peaks)	10 956 mg*h/L	12 558 mg*h/L
$t_{1/2}$ (1st peak)	2.08 days	2.36 days
Steady-state volume of distribution	0.303 L/m^2	0.287 L/m^2

Hematological and Cytokine Profiles of Macaques

The primary concern with the administration of a viral protein JO and the chemotherapeutic Doxil® is the possibility of immunogenicity and toxicity causing significant adverse effects. With the possibility of immune complexes now abundantly clear, it was necessary to examine the potential effects of complexes on immune responses such as activation of complement, inflammation and cytokine storm. Externally, the animals did not show overt symptoms or severe distress, and histopathological sections did not indicate any irregular cell morphology or pathology. Hematological profile of monkeys at the time points were taken (Figure 5-7). No significant abnormalities were noted in hemoglobin or hematocrit levels. A transient spike in white blood cell and lymphocytes were noted, likely as a reaction to the viral JO antigen. Cortisol and complement component 3 (C3) tests levels dipped transiently with each administration. Most other lymphocyte and granulocyte populations remained steady throughout the injections. There were no significant differences to be seen between the two animals except a residually higher white blood cell and lymphocyte count in the animal #2.

Looking further into the immune response in the animals, we carried out an inflammatory Th1/Th2 cytokine array on the macaque serum at various time points during and after each injection. The cytokines tested included interferon gamma, tumor necrosis factor (TNF), IL-6, IL-5, IL-4, and IL-2. Of these, IL-2 was not detected in any sample at any time point. Spikes in the other cytokines were detected very shortly after each injection, peaking at the 2 hour post-administration time point for each injection and increasing thereafter for subsequent injections, although only relevant amounts of IL-6, IL-5, and TNF were detected. Notable differences were seen between the two animals in the cytokine levels, as animal #2, which received no immunosuppression, reached IL-6 levels as high as 10,000 pg/mL (10 ng/mL) 2 hours after the

last administration of JO and Doxil ® (Figure 5-8). Animal #2 also showed high levels of TNF by the last injection of medication as well. Thus, the immunosuppressive regimen given to animal #1 in the form of cyclophosphamide and steroids is successful in suppressing immune response in the form of cytokines and cellular immune response, and no detrimental hematological or cytokine profiles were noted in the animal which received the full regimen of JO, Doxil®, and immunosuppression. However, the administration of JO and Doxil® without any immunosuppression results in increases in inflammatory cytokines, primarily IL-6.

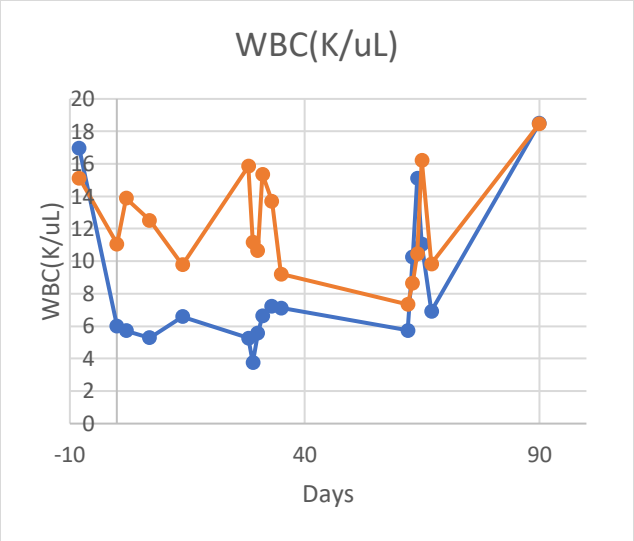
WBC(K/uL)
WBC(K/uL)
Days

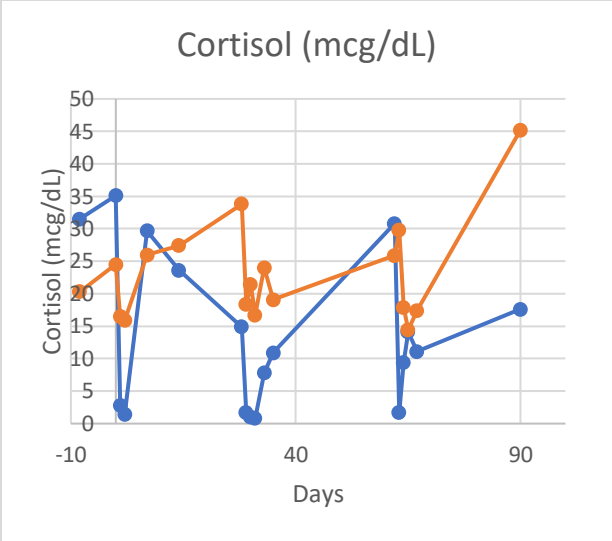
Cortisol (mcg/dL)
Cortisol (mcg/dL)
Days

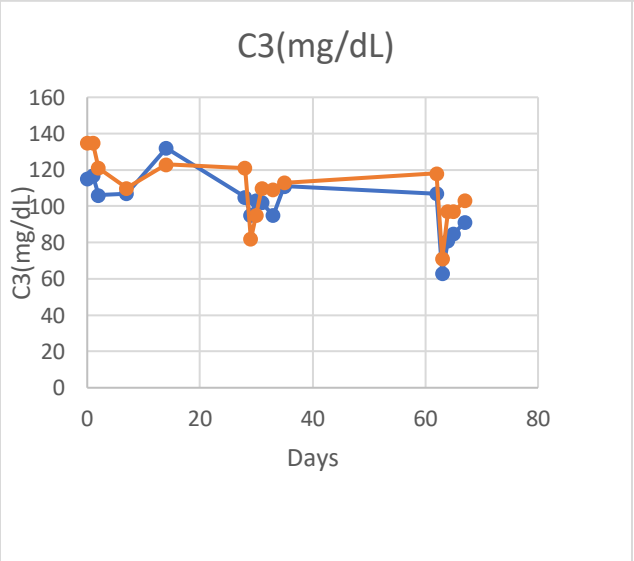
C3(mg/dL)
C3(mg/dL)
Days

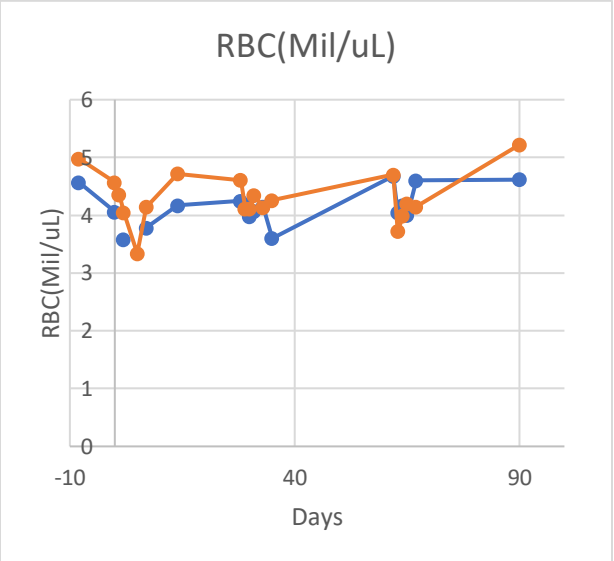
RBC(Mil/uL)
RBC(Mil/uL)
Days

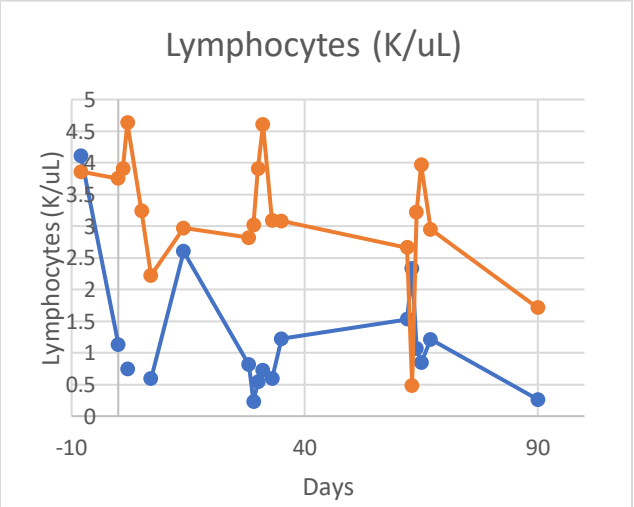
Lymphocytes (K/uL)
Lymphocytes (K/uL)
Days

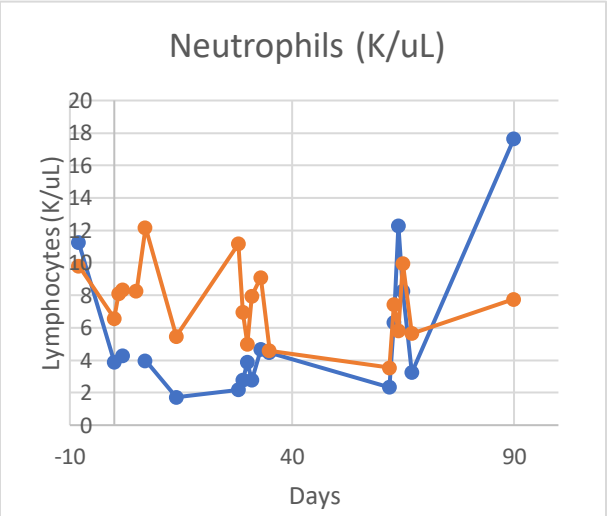
Neutrophils (K/uL)
Lymphocytes (K/uL)
Days

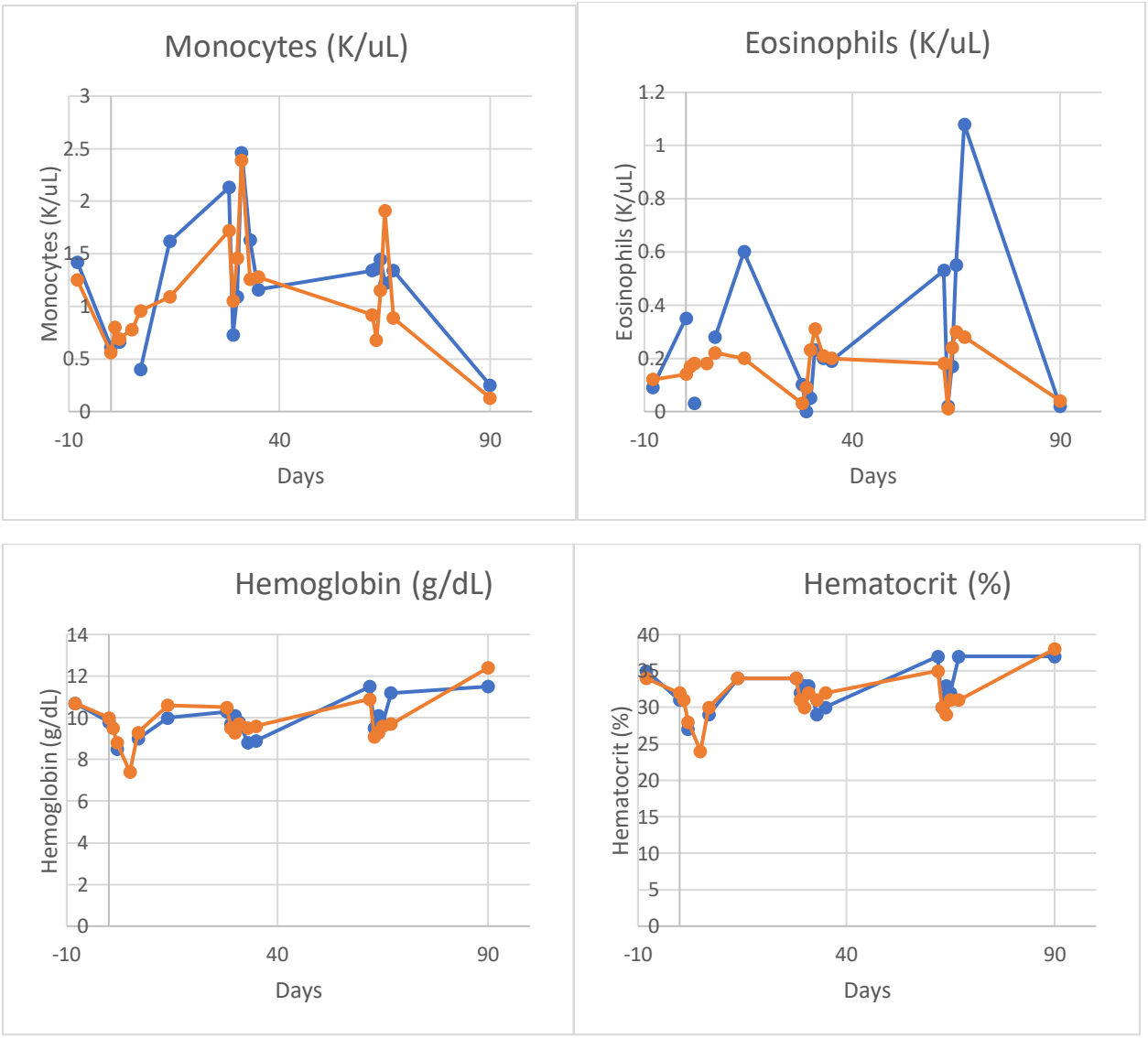

Figure 5-7 Hematological Parameters for animals after receiving JO and Doxil® Administrations

Blood samples were taken from macaques at indicated time points and a complete blood count (CBC) was performed on samples within 30 minutes of collection. Animal #1 is indicated by blue lines, while Animal #2 is indicated by the orange lines.

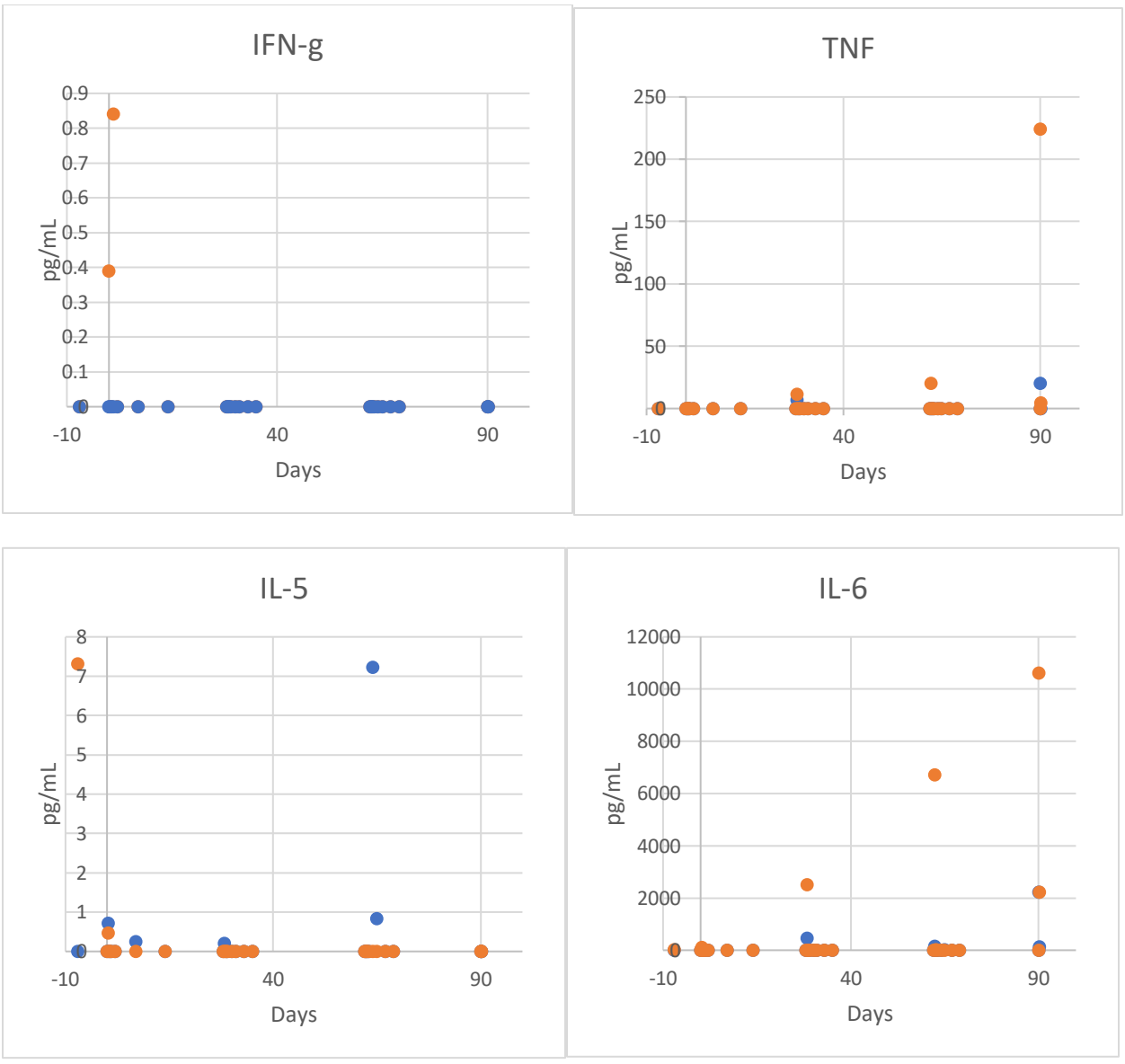

Figure 5-8 Inflammatory cytokine profiles of macaques after JO and Doxil ® administration.

Serum from macaques were taken at indicated time points and a multi-panel cytokine bead assay (CBA) was run using a BD LSR II. Blue dots indicate data for animal #1; orange dots indicate data for animal #2. Note the different ranges on the y-axis in pg/mL.

5.5 Discussion

The Junction Opener protein has already been investigated thoroughly in preclinical models to enhance tumor therapeutics by transiently opening solid tumor tight junctions to facilitate access and drug penetration into the solid tumor microenvironment. Its potential to enhance existing therapies in ovarian cancers and other epithelial cancers in humans will be explored in future clinical trials. However, the combination of a viral protein and a PLD formulation has the potential to cause pathology and immunogenicity in patients, and investigating it is therefore of critical importance prior to proceeding to a clinical trial. We carried out a preclinical immunogenicity and toxicity study in crab-eating macaques (*Macaca fascicularis)*, to measure immune response and to note any adverse reactions in animals as reference in proceeding with research in humans. As in a previous preclinical study of the JO+Doxil® combination in macaques, we administered a regimen that would be more similar to the regimen to be used in human clinical trials, 4 administrations over 16 weeks (in contrast to the previous 2 doses in 14 days) (163), with an added immunosuppression regimen to one of the animals as a way of suppressing the anti-JO response.

Animals did not show overt signs of pathology or serious adverse effects in response to 4 doses of JO+Doxil® combination, spaced over 4 months. This is similar to what was found during the previous preclinical macaque study, where no overt abnormalities were noted (163). This further corroborates the safety of JO administered intravenously, allaying concerns that have been raised that JO could target ubiquitous DSG2 in epithelial non-tumor cells and trigger EMT causing structural damage in normal organs or tissues.

We confirmed that the immune response was effectively suppressed by the immunosuppressive regimen of cyclophosphamide and steroids, demonstrated by the decreased levels of anti-JO

antibodies and the suppressed inflammatory cytokine levels in the immunosuppressed animal compared to the control animal, although this suppression faded by the 4th round of injections. This suggests the addition of Cytoxan® and additional immunomodulatory agents in a JO + Doxil® clinical trial could suppress inflammatory immune responses, thus decreasing the possibility of adverse reactions. Cyclophosphamide was used as a single agent before the development of platinum-based medications (182), and was investigated as a potential co-therapeutic with paclitaxel or cisplatin (183, 184). No severe safety issues were noted in such trials, further corroborating the use of cyclophosphamide as an immunomodulatory agent in such a regimen.

No significant issues were noted in the clearance of JO, with a half-life of about 6 hours. This is largely in line with previous macaque studies, where JO was undetectable by 3 days post administration (163). Surprisingly, with each subsequent administration the peak concentration decreased, indicating that clearance accelerated and may be a result of immune reaction and formation of immune complexes. Antibody levels accordingly increased with subsequent injections, and indeed immune complex formation could be a factor in the clearance. Immune complexes pose a significant threat to the patient, potentially manifesting in a multitude of disorders including complement activation, nephritis, vasculitis, inflammation, general immunopathology, and severe organ damage (185). While C3 activation did not increase, IL-6, a key pro-inflammatory cytokine, increased dramatically without the presence of immunosuppression. IL-6 is a constant concern for treatments as it can be a marker of immunopathology if present in excess. Adverse reactions in patients receiving CAR-T cells implicate IL-1 and IL-6 heavily in neurotoxicity and cytokine release syndrome (CRS)(186), and IL-6 is associated with immunopathology, CRS, and poor prognosis in COVID-19

infections(187, 188). Presence of JO was detected in multiple organs, and immunofluorescence analysis found that the JO may form immune complexes that are subsequently phagocytosed by cells such as macrophages in the lung or Kupffer cells in the liver, further contributing to clearance. The accelerating clearance and the decreasing peak concentration will be a critical point to observe in patients, and with the possibility of pre-existing immunity in some patients against Ad3, adjustment in the immunosuppression regimen or the dosage of JO may be needed. Doxil concentrations in serum followed a typical first-order kinetic linear profile and did not seem to cause drastic changes in hematologic parameters, save a transient decrease in lymphocytic cells with each administration. Notably, no antibody responses against PEG were detected, indicating that immune responses against PEG contained in PLD formulations do not have an impact on pharmacokinetics. Of particular concern was the possibility of antibodies against PEG triggering hypersensitivity to PEG, a ubiquitous molecule in modern society, and those fears appear to have been unfounded. There are indeed cases of hypersensitivity to PEGylated liposomes which can cause suboptimal pharmacokinetics and adverse reactions, occurring in up to 7% of Doxil® clinical trial participants (189). This may be due to pre-existing immunity to PEG, which has been described to affect a small minority of patients (190). The likelihood of PEG hypersensitivity is associated with multiple factors, including size of the PEG molecule, the therapeutic conjugate/cargo administered with PEGylated moieties, dosage, and frequency of drug administration (189, 191). The potential for emergence of anti-PEG responses will be closely monitored in future clinical trials, but indications from the macaque data do not indicate the JO+Doxil® combination as a major factor.

Overall, we were able to successfully test a combination of PLD and JO in *M. fascicularis,* testing the eventual regimen that would be implemented in clinical trials. While JO, an

engineered adenoviral protein, triggered some immunogenicity and cytokines as predicted, this did not manifest in overt symptoms and the immune response was further suppressed by an immunosuppressive regimen. Doxil® was well tolerated with no evidence of any humoral anti-PEG response. The addition of JO, which enhances cancer therapies by targeting epithelial tight junctions, to PLD holds great therapeutic potential, and there seem to be no major safety issues in monkeys. Toxicology trials of JO will continue in DSG2-transgenic mice to produce IND-enabling data and we will investigate the combination further in forthcoming ovarian cancer clinical trials.

5.6 Acknowledgements

The Washington National Primate Research Center (WaNPRC) handled the animals and administered treatments. Complete blood count (CBC) tests were carried out at the University of Washington Medical Center. Chang Li assisted with the cytokine flow cytometry bead (CBA) panels. Steve Roffler and Bingmae Chen provided anti-PEG antibodies for Doxil® detection and assisted in ELISA setup and analysis.

Chapter 6 CONCLUSIONS AND FUTURE DIRECTIONS

6.1 Overview

This dissertation focused on the further development of an adenoviral engineered protein, JO, and explored its therapeutic potential in epithelial cancers, specifically ovarian cancer. JO's binding partner and receptor, DSG2, was identified as a biomarker of ovarian cancer using tissue samples and clinical data. DSG2 expression correlated with disease progression, survival, and chemoresistance. This suggests the use of DSG2 as a biomarker and prognostic tool, as a potential addition to the sorely lacking molecular toolbox for ovarian cancer detection and prognosis. It also established the potential of targeting tumors expressing high levels of DSG2, suggesting the use of JO in ovarian cancer cases.

The development of JO as a co-therapeutic has previously been investigated to detail. Chapter 3 concentrated on further facilitating its use by integrating new modes of drug delivery by conjugation of JO to PLD formulations. A conjugatable form of JO, JOC-x, was formed by the addition of a cysteine to its C-terminus, facilitating the addition of a conjugated payload by means of a maleimide-sulfhydryl chemical linkage. The conjugation was successful and was confirmed by the increase in nanoparticle size and the detection of JO in the JOC-LD mixture. The DSG2 binding properties of JO and the cytotoxic properties of PLD were retained, and the JOC-PLD performed superior to Doxil® alone or the separate combination of JO + Doxil®, suggesting the potential of JOC-PLD to further enhance the anti-tumor properties of PLD and additionally mediate a dose-sparing effect and a decrease in systemic side effects.

Lastly, we tested the possibility of JO and Doxil® to trigger immunogenic or toxic effects in animal models, as preparation for its eventual use in ovarian cancer patients. Antibodies against

JO were detected but they were successfully suppressed by an immunosuppressive regimen comprised of cyclophosphamide and steroids; no antibodies were detected against the PEG portion of Doxil®. The pharmacokinetic profile of JO in the serum showed a faster-than-expected clearance, but did not deviate significantly from previous PK studies of JO in macaques. Notably, the monkeys showed no overt symptoms or pathology over 4 administrations in a span of 16 weeks, suggesting that the regimen would likely have favorable safety profiles in a clinical context.

6.2 Discussion and Future Steps

Many advances in ovarian cancer have been made in recent years but the tools available for both treatment and diagnosis remain sparse, with relatively few approvals for use compared to other cancers. Advances in molecular diagnostics for ovarian cancer have mostly involved panels of previously found markers, but sensitivity and specificity do not warrant for these to be used independently of biopsy or surgery. The addition of DSG2 as a molecular biomarker and prognostic could contribute greatly to this field. Preliminary analyses of ovarian cancer samples indicate a correlation with disease progression, chemoresistance, and survival; not many biomarkers are able to identify all of these factors in cancers. Granted, these are preliminary data looking mostly at averages of survival and histopathological data. The logical next steps would be to analyze DSG2 expression more closely in serum of ovarian cancer patients and associate it with disease staging and/or chemoresistance. The survival data are also preliminary and had a small sample size, which could be further corroborated with a larger number of patients. Ultimately, the definitive trial would involve a blinded analysis of an ovarian cancer cohort, to assess the predictive capability of DSG2 of cancer chemoresistance and outcome.

The development of JO as a tumor co-therapeutic holds much promise and this dissertation explored its further enhancement. The conjugation of a therapeutic protein to its cargo has mostly been explored in the context of antibody-drug conjugates (ADC), or protein-polymer (mostly PEG) conjugates to enhance bioavailability and specificity (51, 192). JO has the advantages of enhanced homing, and the opening of junctions, thus facilitating drug delivery to the site and penetration into the tumor milieu. In comparison to antibodies and polymers, JOC-x is easily produced in *E. coli* at high yields (160) and the conjugation process (maleimide-sulfhydryl conjugation) is commonly used throughout the industry. JOC was found to maintain the DSG2-binding capabilities of the JO protein, indicating that the removal of native cysteines and the addition of the terminal cysteine did not affect binding kinetics. The mode of multimerization, however, was expected to change as JOC removed the positively charged dimerization domain (DD), allowing the cysteines' S-S linkages to take over the role. JO is not able to mediate its junction-opening activity without higher-order complex and multimerization, and in JOC-x the formation of such complexes is conserved through sulfhydryl interactions. Interestingly, the conjugation of JOC-x through its cysteine to human serum albumin or liposomal doxorubicin did not significantly compromise its DSG2 binding capabilities, indicating that the loss of the sulfhydryl interactions may in part be compensated for by the avidity of JOC-x coating the surface of its cargo. A logical next step in analyzing JOC-x conjugates would be to quantify the number of JOC copies on the surface of the conjugates, which can likely be done through means such as mass spectrometry.

The successful conjugation of liposomal doxorubicin to JOC-x poses many therapeutic benefits, including ease of administration and dose sparing. Liposomal formulations increase bioavailability through its slower release mechanism and its homing to tumor through the leaky

tumor-associated blood vessels (i.e. “passive targeting”)(193). PLD is a second-generation liposome, often referred to as stealth liposomes, which make use of a PEGylated coat on to further enhance persistence and also to decrease clearance by the mononuclear phagocyte system (194). The homing mechanism of PLD is further improved with JOC-x, which targets an epithelial tumor biomarker DSG2, along with the added benefit of tumor milieu penetration. The JOC-LD conjugate was able to retain both the DSG2-binding capabilities of JO and the cytotoxic capabilities of the PLD payload, which increased its likelihood to be a successful therapeutic candidate. JOC-LD’s *in vivo* efficacy in a cancer xenograft model in mice proved many of the advantages of JOC-LD over the individual components JO and PLD, ultimately resulting in a longer survival and a notable 40% cure rate which was not seen in the separate administration group. This increased efficacy of the JOC-LD conjugate at the same doxorubicin equivalent dose as Doxil® indicates the possibility of dose sparing, meaning the efficacy of a certain dose of Doxil® may be achieved with a lower dose of JOC-LD. This, in conjunction with ease of administration, makes JOC-LD a candidate therapeutic to investigate further. Future steps would include more detailed biophysical analysis of the JOC-LD, including electron microscopy to confirm integrity of liposomes and conjugated JOC, the quantification of JOC on the surface of LD. Further *in vivo* investigations making use of multiple tumor cell line, specifically for ovarian cancer (e.g. ovc316 cells) could be used in xenograft models to establish JOC-LD’s efficacy in multiple types of epithelial cancers.

Finally, this dissertation explored the possibility of immunogenicity and toxicity generated by the combination of JO and Doxil® in crab-eating macaques (*M. fascicularis)*. As the therapeutic characterization of JOC-LD was insufficient for use in larger animals, we were only able to explore the therapeutic combination of JO and Doxil® separately. Antibodies to JO were

detected as expected, but the addition of an immunosuppressive regimen was able to abate antibody levels sufficiently. Notably, no adverse reactions or overt pathology were seen, which indicates the safety of the regimen for use in larger animals and eventually humans. The clearance of JO from serum was faster than expected, and the elevated antibodies were found to be a factor. We found that the formation of immune complexes and uptake by phagocytic cells as part of the mononuclear phagocyte system in liver and lungs is likely responsible for clearance. For a candidate therapeutic, this could be a fatal shortcoming, as immune complexes can mediate multiple disorders and immunopathology. The suppression of antibodies will be a crucial factor in future clinical trials, and indeed the inclusion of cyclophosphamide as was done in the macaque trials may need to be included in human trials with optimization. To overcome fast clearance and immune complexes, adjusting the dose of immunosuppression and JO will need to be further explored in NHPs and patients. The immunosuppression regimen may also be needed to address the inflammatory responses that were observed, as the JO+Doxil® combination triggered a robust IL-6 response without immunosuppression. IL-6 overexpression is the archetypal marker of immunopathology and cytokine release syndrome and must be controlled in human clinical trials. In the NHP trial, IL-6 levels in serum were sufficiently controlled only with the immunosuppression regimen, thus necessitating the regimen in future trials. Immediate future steps in the NHP experiments will involve an additional animal with doubled JO dosage (2 mg/kg to 4 mg/kg), and the retention of the immunosuppression regimen. We hypothesize that the peak concentration will be higher, and the half-time will be longer. However, the antibody and cytokine levels will be observed very closely as there is a high probability that these will increase accordingly and it remains to be seen whether the immunosuppression regimen as it

stands will be able to effectively suppress it. All of the data generated will inform the parameters of the eventual human clinical trial, where safety will be of paramount importance.

The objective of this dissertation was to explore a novel mode of therapy, confirm its target molecule as a cancer-specific target, and to enhance its delivery by mode of conjugation to a chemotherapeutic payload. There are still many steps to confirming the conjugated product as a bona fide therapeutic candidate, but the data generated regarding JOC-LD in this dissertation will move it along the therapeutic development pipeline. Overall, the establishment of DSG2 as a biomarker of ovarian cancer and JOC-LD as a therapeutic candidate, with their own respective strengths and benefits compared to current tools, will be powerful additions in the fight against ovarian cancer and by extension, other solid tumors.

REFERENCES

1. Bray F, Ferlay J, Soerjomataram I, Siegel RL, Torre LA, Jemal A. Global cancer statistics 2018: GLOBOCAN estimates of incidence and mortality worldwide for 36 cancers in 185 countries. CA Cancer J Clin. 2018;68(6):394-424.

2. Wang H, Naghavi M, Allen C, Barber RM, Bhutta ZA, Carter A, et al. Global, regional, and national life expectancy, all-cause mortality, and cause-specific mortality for 249 causes of death, 1980–2015: a systematic analysis for the Global Burden of Disease Study 2015. The Lancet. 2016;388(10053):1459-544.

3. Survival Rates of Ovarian Cancer: American Cancer Society; 2015 [Available from: https://www.cancer.org/cancer/ovarian-cancer/detection-diagnosis-staging/survival-rates.html.

4. Ovarian Cancer Types: Cancer Treatment Centers of America; 2020 [Available from: https://www.cancercenter.com/cancer-types/ovarian-cancer/types.

5. Types & Stages of Ovarian Cancer: National Ovarian Cancer Coalition; 2015 [Available from: http://ovarian.org/about-ovarian-cancer/what-is-ovarian-cancer/types-a-stages.

6. Neff RT, Senter L, Salani R. BRCA mutation in ovarian cancer: testing, implications and treatment considerations. Therapeutic advances in medical oncology. 2017;9(8):519-31.

7. Bookman M. Optimal primary therapy of ovarian cancer. Annals of Oncology. 2016;27(suppl_1):i58-i62.

8. Garcia MA, Nelson WJ, Chavez N. Cell–cell junctions organize structural and signaling networks. Cold Spring Harbor perspectives in biology. 2018;10(4):a029181.

9. Alberts B, Johnson A, Lewis J, Raff M, Roberts K, Walter P. Cell junctions. Molecular Biology of the Cell 4th edition: Garland Science; 2002.

10. Kumar NM, Gilula NB. The gap junction communication channel. Cell. 1996;84(3):381-8.

11. Niessen CM. Tight junctions/adherens junctions: basic structure and function. Journal of investigative dermatology. 2007;127(11):2525-32.

12. Kniesel U, Wolburg H. Tight junctions of the blood–brain barrier. Cellular and molecular neurobiology. 2000;20(1):57-76.

13. Slomiany B, Slomiany A. Mucus and gastric mucosal protection. the Stomach: Springer; 1993. p. 116-43.

14. Garrod DR. Desmosomes and hemidesmosomes. Current opinion in cell biology. 1993;5(1):30-40.

15. Dubash AD, Green KJ. Desmosomes. Current Biology. 2011;21(14):R529-R31.

16. Delva E, Tucker DK, Kowalczyk AP. The desmosome. Cold Spring Harbor perspectives in biology. 2009;1(2):a002543-a.

17. Garrod D, Chidgey M, North A. Desmosomes: differentiation, development, dynamics and disease. Current opinion in cell biology. 1996;8(5):670-8.

18. Shin K, Fogg VC, Margolis B. Tight Junctions and Cell Polarity. Annual Review of Cell and Developmental Biology. 2006;22(1):207-35.

19. Garrod D, Chidgey M. Desmosome structure, composition and function. Biochimica et Biophysica Acta (BBA) - Biomembranes. 2008;1778(3):572-87.

20. Gross S, Walden P. Immunosuppressive mechanisms in human tumors: why we still cannot cure cancer. Immunology letters. 2008;116(1):7-14.

21. Valkenburg KC, de Groot AE, Pienta KJ. Targeting the tumour stroma to improve cancer therapy. Nature reviews Clinical oncology. 2018;15(6):366-81.

22. Choi IK, Strauss R, Richter M, Yun CO, Lieber A. Strategies to increase drug penetration in solid tumors. Front Oncol. 2013;3:193.

23. Tannock IF, Lee CM, Tunggal JK, Cowan DS, Egorin MJ. Limited penetration of anticancer drugs through tumor tissue: a potential cause of resistance of solid tumors to chemotherapy. Clin Cancer Res. 2002;8(3):878-84.

24. Minchinton AI, Tannock IF. Drug penetration in solid tumours. Nat Rev Cancer. 2006;6(8):583-92.

25. Fessler SP, Wotkowicz MT, Mahanta SK, Bamdad C. MUC1* is a determinant of trastuzumab (Herceptin) resistance in breast cancer cells. Breast Cancer Res Treat. 2009;118(1):113-24.

26. Oliveras-Ferraros C, Vazquez-Martin A, Cufi S, Queralt B, Baez L, Guardeno R, et al. Stem cell property epithelial-to-mesenchymal transition is a core transcriptional network for predicting cetuximab (Erbitux) efficacy in KRAS wild-type tumor cells. J Cell Biochem. 2011;112(1):10-29.

27. Lee CM, Tannock IF. The distribution of the therapeutic monoclonal antibodies cetuximab and trastuzumab within solid tumors. BMC Cancer. 2010;10:255.

28. Christiansen JJ, Rajasekaran AK. Reassessing epithelial to mesenchymal transition as a prerequisite for carcinoma invasion and metastasis. Cancer Res. 2006;66(17):8319-26.

29. Ghebremedhin B. Human adenovirus: Viral pathogen with increasing importance. European Journal of Microbiology & Immunology. 2014;4(1):26-33.

30. Rowe WP, Huebner RJ, Gilmore LK, Parrott RH, Ward TG. Isolation of a Cytopathogenic Agent from Human Adenoids Undergoing Spontaneous Degeneration in Tissue Culture. Proceedings of the Society for Experimental Biology and Medicine. 1953;84(3):570-3.

31. Rux JJ, Burnett RM. Adenovirus structure. Human gene therapy. 2004;15(12):1167-76.

32. CDC. Adenoviruses 2017 [Available from: https://www.cdc.gov/adenovirus/index.html.

33. SM Wold W, Toth K. Adenovirus vectors for gene therapy, vaccination and cancer gene therapy. Current gene therapy. 2013;13(6):421-33.

34. Lee CS, Bishop ES, Zhang R, Yu X, Farina EM, Yan S, et al. Adenovirus-Mediated Gene Delivery: Potential Applications for Gene and Cell-Based Therapies in the New Era of Personalized Medicine. Genes & diseases. 2017;4(2):43-63.

35. Liu Q, Zaiss AK, Colarusso P, Patel K, Haljan G, Wickham TJ, et al. The role of capsid–endothelial interactions in the innate immune response to adenovirus vectors. Human gene therapy. 2003;14(7):627-43.

36. Alba R, Bosch A, Chillon M. Gutless adenovirus: last-generation adenovirus for gene therapy. Gene therapy. 2005;12(1):S18-S27.

37. Nwanegbo E, Vardas E, Gao W, Whittle H, Sun H, Rowe D, et al. Prevalence of neutralizing antibodies to adenoviral serotypes 5 and 35 in the adult populations of The Gambia, South Africa, and the United States. Clinical and diagnostic laboratory immunology. 2004;11(2):351-7.

38. Mast TC, Kierstead L, Gupta SB, Nikas AA, Kallas EG, Novitsky V, et al. International epidemiology of human pre-existing adenovirus (Ad) type-5, type-6, type-26 and type-36 neutralizing antibodies: correlates of high Ad5 titers and implications for potential HIV vaccine trials. Vaccine. 2010;28(4):950-7.

39. Abbink P, Lemckert AAC, Ewald BA, Lynch DM, Denholtz M, Smits S, et al. Comparative seroprevalence and immunogenicity of six rare serotype recombinant adenovirus vaccine vectors from subgroups B and D. Journal of virology. 2007;81(9):4654-63.

40. Wang H, Li Z-Y, Liu Y, Persson J, Beyer I, Möller T, et al. Desmoglein 2 is a receptor for adenovirus serotypes 3, 7, 11 and 14. Nature medicine. 2011;17(1):96.

41. Bewley MC, Springer K, Zhang Y-B, Freimuth P, Flanagan JM. Structural analysis of the mechanism of adenovirus binding to its human cellular receptor, CAR. Science. 1999;286(5444):1579-83.

42. Gaggar A, Shayakhmetov DM, Lieber A. CD46 is a cellular receptor for group B adenoviruses. Nature medicine. 2003;9(11):1408-12.

43. Arnberg N. Adenovirus receptors: implications for targeting of viral vectors. Trends in Pharmacological Sciences. 2012;33(8):442-8.

44. Haque E, Banik U, Monwar T, Anthony L, Adhikary AK. Worldwide increased prevalence of human adenovirus type 3 (HAdV-3) respiratory infections is well correlated with heterogeneous hypervariable regions (HVRs) of hexon. PLOS ONE. 2018;13(3):e0194516.

45. Schmitz H, Wigand R, Heinrich W. Worldwide epidemiology of human adenovirus infections. Am J Epidemiol. 1983;117(4):455-66.

46. Arnemann J, Spurr NK, Magee AI, Buxton RS. The human gene (DSG2) coding for HDGC, a second member of the desmoglein subfamily of the desmosomal cadherins, is, like DSG1 coding for desmoglein DGI, assigned to chromosome 18. Genomics. 1992;13(2):484-6.

47. Kamekura R, Kolegraff KN, Nava P, Hilgarth RS, Feng M, Parkos CA, et al. Loss of the desmosomal cadherin desmoglein-2 suppresses colon cancer cell proliferation through EGFR signaling. Oncogene. 2013;33:4531.

48. Brennan D, Mahoney MG. Increased expression of Dsg2 in malignant skin carcinomas: A tissue-microarray based study. Cell Adhesion & Migration. 2009;3(2):148-54.

49. Barber AG, Castillo-Martin M, Bonal DM, Rybicki BA, Christiano AM, Cordon-Cardo C. Characterization of desmoglein expression in the normal prostatic gland. Desmoglein 2 is an independent prognostic factor for aggressive prostate cancer. PLoS One. 2014;9(6):e98786.

50. Beckman RA, Weiner LM, Davis HM. Antibody constructs in cancer therapy: protein engineering strategies to improve exposure in solid tumors. Cancer. 2007;109(2):170-9.

51. Peer D, Karp JM, Hong S, Farokhzad OC, Margalit R, Langer R. Nanocarriers as an emerging platform for cancer therapy. Nature nanotechnology. 2007;2(12):751-60.

52. Koch PJ, Goldschmidt MD, Walsh MJ, Zimbelmann R, Franke WW. Complete amino acid sequence of the epidermal desmoglein precursor polypeptide and identification of a second type of desmoglein gene. Eur J Cell Biol. 1991;55(2):200-8.

53. Posch MG, Posch MJ, Geier C, Erdmann B, Mueller W, Richter A, et al. A missense variant in desmoglein-2 predisposes to dilated cardiomyopathy. Molecular genetics and metabolism. 2008;95(1-2):74-80.

54. Syrris P, Ward D, Asimaki A, Evans A, Sen-Chowdhry S, Hughes SE, et al. Desmoglein-2 mutations in arrhythmogenic right ventricular cardiomyopathy: a genotype–phenotype characterization of familial disease. European heart journal. 2007;28(5):581-8.

55. Pilichou K, Nava A, Basso C, Beffagna G, Bauce B, Lorenzon A, et al. Mutations in desmoglein-2 gene are associated with arrhythmogenic right ventricular cardiomyopathy. Circulation. 2006;113(9):1171-9.

56. Beyer I, Cao H, Persson J, Song H, Richter M, Feng Q, et al. Coadministration of epithelial junction opener JO-1 improves the efficacy and safety of chemotherapeutic drugs. Clin Cancer Res. 2012;18(12):3340-51.

57. Beyer I, van Rensburg R, Strauss R, Li Z, Wang H, Persson J, et al. Epithelial junction opener JO-1 improves monoclonal antibody therapy of cancer. Cancer Res. 2011;71(22):7080-90.

58. Wang H, Beyer I, Persson J, Song H, Li Z, Richter M, et al. A new human DSG2-transgenic mouse model for studying the tropism and pathology of human adenoviruses. J Virol. 2012;86(11):6286-302.

59. Wang H, Li Z, Yumul R, Lara S, Hemminki A, Fender P, et al. Multimerization of adenovirus serotype 3 fiber knob domains is required for efficient binding of virus to desmoglein 2 and subsequent opening of epithelial junctions. J Virol. 2011;85(13):6390-402.

60. Wang H, Ducournau C, Saydaminova K, Richter M, Yumul R, Ho M, et al. Intracellular signaling and desmoglein 2 shedding triggered by human adenoviruses Ad3, Ad14, and Ad14P1 Journal of Virology. 2015;accepted.

61. Lu ZZ, Wang H, Zhang Y, Cao H, Li Z, Fender P, et al. Penton-dodecahedral particles trigger opening of intercellular junctions and facilitate viral spread during adenovirus serotype 3 infection of epithelial cells. PLoS Pathog. 2013;9(10):e1003718.

62. Wang H, Li ZY, Liu Y, Persson J, Beyer I, Moller T, et al. Desmoglein 2 is a receptor for adenovirus serotypes 3, 7, 11 and 14. Nat Med. 2011;17(1):96-104.

63. Richter M, Yumul R, Wang H, Saydaminova K, Ho M, May D, et al. Preclinical safety and efficacy studies with an affinity-enhanced epithelial junction opener and PEGylated liposomal doxorubicin. Mol Ther Methods Clin Dev. 2015;2:15005.

64. Beyer I, van Rensburg R, Strauss R, Li Z, Wang H, Persson J, et al. Epithelial junction opener JO-1 improves monoclonal antibody therapy of cancer. Cancer research. 2011;71(22):7080-90.

65. Richter M, Yumul R, Wang H, Saydaminova K, Ho M, May D, et al. Preclinical safety and efficacy studies with an affinity-enhanced epithelial junction opener and PEGylated liposomal doxorubicin. Molecular Therapy-Methods & Clinical Development. 2015;2.

66. Amieva MR, Vogelmann R, Covacci A, Tompkins LS, Nelson WJ, Falkow S. Disruption of the epithelial apical-junctional complex by Helicobacter pylori CagA. Science. 2003;300(5624):1430-4.

67. Rossing MA, Wicklund KG, Cushing-Haugen KL, Weiss NS. Predictive value of symptoms for early detection of ovarian cancer. Journal of the National Cancer Institute. 2010;102(4):222-9.

68. Risch HA, Marrett LD, Jain M, Howe GR. Differences in risk factors for epithelial ovarian cancer by histologic type: results of a case-control study. American journal of epidemiology. 1996;144(4):363-72.

69. Bhoola S, Hoskins WJ. Diagnosis and management of epithelial ovarian cancer. Obstetrics & Gynecology. 2006;107(6):1399-410.

70. Ueland FR. A Perspective on Ovarian Cancer Biomarkers: Past, Present and Yet-To-Come. Diagnostics (Basel, Switzerland). 2017;7(1):14.

71. Muinao T, Deka Boruah HP, Pal M. Diagnostic and Prognostic Biomarkers in ovarian cancer and the potential roles of cancer stem cells - An updated review. Exp Cell Res. 2018;362(1):1-10.

72. Torre LA, Trabert B, DeSantis CE, Miller KD, Samimi G, Runowicz CD, et al. Ovarian cancer statistics, 2018. CA: a cancer journal for clinicians. 2018;68(4):284-96.

73. Gordon AN, Granai CO, Rose PG, Hainsworth J, Lopez A, Weissman C, et al. Phase II study of liposomal doxorubicin in platinum- and paclitaxel-refractory epithelial ovarian cancer. J Clin Oncol. 2000;18(17):3093-100.

74. Muggia FM, Hainsworth JD, Jeffers S, Miller P, Groshen S, Tan M, et al. Phase II study of liposomal doxorubicin in refractory ovarian cancer: antitumor activity and toxicity modification by liposomal encapsulation. J Clin Oncol. 1997;15(3):987-93.

75. Markman M, Kennedy A, Webster K, Peterson G, Kulp B, Belinson J. Phase 2 trial of liposomal doxorubicin (40 mg/m(2)) in platinum/paclitaxel-refractory ovarian and fallopian tube cancers and primary carcinoma of the peritoneum. Gynecol Oncol. 2000;78(3 Pt 1):369-72.

76. Gordon AN, Fleagle JT, Guthrie D, Parkin DE, Gore ME, Lacave AJ. Recurrent epithelial ovarian carcinoma: a randomized phase III study of pegylated liposomal doxorubicin versus topotecan. J Clin Oncol. 2001;19(14):3312-22.

77. Pignata S, Scambia G, Ferrandina G, Savarese A, Sorio R, Breda E, et al. Carboplatin plus paclitaxel versus carboplatin plus pegylated liposomal doxorubicin as first-line treatment for patients with ovarian cancer: the MITO-2 randomized phase III trial. J Clin Oncol. 2011;29(27):3628-35.

78. Bookman MA, Greer BE, Ozols RF. Optimal therapy of advanced ovarian cancer: carboplatin and paclitaxel vs. cisplatin and paclitaxel (GOG 158) and an update on GOG0 182-ICON5. Int J Gynecol Cancer. 2003;13(6):735-40.

79. Yuan F, Leunig M, Huang SK, Berk DA, Papahadjopoulos D, Jain RK. Microvascular permeability and interstitial penetration of sterically stabilized (stealth) liposomes in a human tumor xenograft. Cancer Res. 1994;54(13):3352-6.

80. Huang SK, Stauffer PR, Hong K, Guo JW, Phillips TL, Huang A, et al. Liposomes and hyperthermia in mice: increased tumor uptake and therapeutic efficacy of doxorubicin in sterically stabilized liposomes. Cancer Res. 1994;54(8):2186-91.

81. Kirpotin DB, Drummond DC, Shao Y, Shalaby MR, Hong K, Nielsen UB, et al. Antibody targeting of long-circulating lipidic nanoparticles does not increase tumor localization but does increase internalization in animal models. Cancer Res. 2006;66(13):6732-40.

82. Alagkiozidis I, Facciabene A, Carpenito C, Benencia F, Jonak Z, Adams S, et al. Increased immunogenicity of surviving tumor cells enables cooperation between liposomal doxorubicin and IL-18. J Transl Med. 2009;7:104.

83. Key Statistics for Ovarian Cancer: American Cancer Society; 2018 [Available from: https://www.cancer.org/cancer/ovarian-cancer/about/key-statistics.html.

84. Curti BD. Physical barriers to drug delivery in tumors. Critical Reviews in Oncology/Hematology. 1993;14(1):29-39.

85. Anderson JM. Molecular structure of tight junctions and their role in epithelial transport. Physiology. 2001;16(3):126-30.

86. Anderson JM, Van Itallie CM. Physiology and function of the tight junction. Cold Spring Harb Perspect Biol. 2009;1(2):a002584.

87. Guttman JA, Finlay BB. Tight junctions as targets of infectious agents. Biochimica et Biophysica Acta (BBA)-Biomembranes. 2009;1788(4):832-41.

88. Bergelson JM, Cunningham JA, Droguett G, Kurt-Jones EA, Krithivas A, Hong JS, et al. Isolation of a common receptor for Coxsackie B viruses and adenoviruses 2 and 5. Science. 1997;275(5304):1320-3.

89. Garrod D, Chidgey M. Desmosome structure, composition and function. Biochimica et Biophysica Acta (BBA)-Biomembranes. 2008;1778(3):572-87.

90. Klessner JL, Desai BV, Amargo EV, Getsios S, Green KJ. EGFR and ADAMs cooperate to regulate shedding and endocytic trafficking of the desmosomal cadherin desmoglein 2. Mol Biol Cell. 2009;20(1):328-37.

91. Wang H, Ducournau C, Saydaminova K, Richter M, Yumul R, Ho M, et al. Intracellular Signaling and Desmoglein 2 Shedding Triggered by Human Adenoviruses Ad3, Ad14, and Ad14P1. J Virol. 2015;89(21):10841-59.

92. Brennan D, Mahoney MG. Increased expression of Dsg2 in malignant skin carcinomas: A tissue-microarray based study. Cell Adh Migr. 2009;3(2):148-54.

93. Harada H, Iwatsuki K, Ohtsuka M, Han GW, Kaneko F. Abnormal desmoglein expression by squamous cell carcinoma cells. Acta Derm Venereol. 1996;76(6):417-20.

94. Cai F, Zhu Q, Miao Y, Shen S, Su X, Shi Y. Desmoglein-2 is overexpressed in non-small cell lung cancer tissues and its knockdown suppresses NSCLC growth by regulation of p27 and CDK2. J Cancer Res Clin Oncol. 2017;143(1):59-69.

95. Sun R, Ma C, Wang W, Yang S. Upregulation of desmoglein 2 and its clinical value in lung adenocarcinoma: a comprehensive analysis by multiple bioinformatics methods. PeerJ. 2020;8:e8420.

96. Jin R, Wang X, Zang R, Liu C, Zheng S, Li H, et al. Desmoglein-2 Modulates Tumor Progression and Osimertinib Drug Resistance through the EGFR/Src/PAK1 Pathway in Lung Adenocarcinoma. Cancer Letters. 2020.

97. Han CP, Yu YH, Wang AG, Tian Y, Zhang HT, Zheng ZM, et al. Desmoglein-2 overexpression predicts poor prognosis in hepatocellular carcinoma patients. Eur Rev Med Pharmacol Sci. 2018;22(17):5481-9.

98. Biedermann K, Vogelsang H, Becker I, Plaschke S, Siewert JR, Hofler H, et al. Desmoglein 2 is expressed abnormally rather than mutated in familial and sporadic gastric cancer. J Pathol. 2005;207(2):199-206.

99. Beyer I, van Rensburg R, Lieber A. Overcoming physical barriers in cancer therapy. Tissue Barriers. 2013;1(1):e23647.

100. Wang CE, Yumul RC, Lin J, Cheng Y, Lieber A, Pun SH. Junction opener protein increases nanoparticle accumulation in solid tumors. J Control Release. 2018;272:9-16.

101. Kuk C, Kulasingam V, Gunawardana CG, Smith CR, Batruch I, Diamandis EP. Mining the ovarian cancer ascites proteome for potential ovarian cancer biomarkers. Mol Cell Proteomics. 2009;8(4):661-9.

102. Xie H, Xu H, Hou Y, Cai Y, Rong Z, Song W, et al. Integrative prognostic subtype discovery in high-grade serous ovarian cancer. J Cell Biochem. 2019.

103. Kim KH, Dmitriev IP, Saddekni S, Kashentseva EA, Harris RD, Aurigemma R, et al. A phase I clinical trial of Ad5/3-Delta24, a novel serotype-chimeric, infectivity-enhanced, conditionally-replicative adenovirus (CRAd), in patients with recurrent ovarian cancer. Gynecol Oncol. 2013;130(3):518-24.

104. Hemminki O, Bauerschmitz G, Hemmi S, Kanerva A, Cerullo V, Pesonen S, et al. Preclinical and clinical data with a fully serotype 3 oncolytic adenovirus Ad3-hTERT-E1A in the treatment of advanced solid tumors. . Molecular Therapy. 2010;18(S1):S74.

105. Koski A, Kangasniemi L, Escutenaire S, Pesonen S, Cerullo V, Diaconu I, et al. Treatment of Cancer Patients With a Serotype 5/3 Chimeric Oncolytic Adenovirus Expressing GMCSF. Mol Ther. 2010.

106. Strauss R, Li ZY, Liu Y, Beyer I, Persson J, Sova P, et al. Analysis of epithelial and mesenchymal markers in ovarian cancer reveals phenotypic heterogeneity and plasticity. PLoS One. 2011;6(1):e16186.

107. Chou J, Fitzgibbon MP, Mortales CL, Towlerton AM, Upton MP, Yeung RS, et al. Phenotypic and transcriptional fidelity of patient-derived colon cancer xenografts in immune-deficient mice. PLoS One. 2013;8(11):e79874.

108. Rustin GJ, Vergote I, Eisenhauer E, Pujade-Lauraine E, Quinn M, Thigpen T, et al. Definitions for response and progression in ovarian cancer clinical trials incorporating RECIST 1.1 and CA 125 agreed by the Gynecological Cancer Intergroup (GCIG). Int J Gynecol Cancer. 2011;21(2):419-23.

109. Schummer M, Drescher C, Forrest R, Gough S, Thorpe J, Hellstrom I, et al. Evaluation of ovarian cancer remission markers HE4, MMP7 and Mesothelin by comparison to the established marker CA125. Gynecol Oncol. 2012;125(1):65-9.

110. Saydaminova K, Strauss R, Xie M, Bartek J, Richter M, van Rensburg R, et al. Sensitizing ovarian cancer cells to chemotherapy by interfering with pathways that are involved in the formation of cancer stem cells. Cancer Biol Ther. 2016;17(10):1079-88.

111. Seiden MV. Progress in gynecologic cancer. Semin Oncol. 2009;36(2):90.

112. Ozols RF, Bundy BN, Greer BE, Fowler JM, Clarke-Pearson D, Burger RA, et al. Phase III trial of carboplatin and paclitaxel compared with cisplatin and paclitaxel in patients with optimally resected stage III ovarian cancer: a Gynecologic Oncology Group study. J Clin Oncol. 2003;21(17):3194-200.

113. Cannistra SA. Cancer of the ovary. N Engl J Med. 2004;351(24):2519-29.

114. Rustin GJ, Nelstrop AE, Tuxen MK, Lambert HE. Defining progression of ovarian carcinoma during follow-up according to CA 125: a North Thames Ovary Group Study. Ann Oncol. 1996;7(4):361-4.

115. Rustin GJ, van der Burg ME, Griffin CL, Guthrie D, Lamont A, Jayson GC, et al. Early versus delayed treatment of relapsed ovarian cancer (MRC OV05/EORTC 55955): a randomised trial. Lancet. 2010;376(9747):1155-63.

116. Peitsch WK, Doerflinger Y, Fischer-Colbrie R, Huck V, Bauer AT, Utikal J, et al. Desmoglein 2 depletion leads to increased migration and upregulation of the chemoattractant secretoneurin in melanoma cells. PLoS One. 2014;9(2):e89491.

117. Kamekura R, Kolegraff KN, Nava P, Hilgarth RS, Feng M, Parkos CA, et al. Loss of the desmosomal cadherin desmoglein-2 suppresses colon cancer cell proliferation through EGFR signaling. Oncogene. 2014;33(36):4531-6.

118. Yashiro M, Nishioka N, Hirakawa K. Decreased expression of the adhesion molecule desmoglein-2 is associated with diffuse-type gastric carcinoma. Eur J Cancer. 2006;42(14):2397-403.

119. Hutz K, Zeiler J, Sachs L, Ormanns S, Spindler V. Loss of desmoglein 2 promotes tumorigenic behavior in pancreatic cancer cells. Mol Carcinog. 2017;56(8):1884-95.

120. Kuryk L, Moller A-S, editors. Oncolytic adenovirus Ad5/3-D24-GM-CSF infects, replicates, and lyses ovarian cancer cells through desmoglein-2 cell entry receptor. American Society for Gene and Cell Therapy (ASGCT); 2020; Boston, MA.

121. Kuryk L, Møller ASW. Chimeric Oncolytic Ad5/3 Virus Replicates and Lyses Ovarian Cancer Cells through Desmoglein‐2 Cell Entry Receptor. Journal of Medical Virology.

122. Green SK, Karlsson MC, Ravetch JV, Kerbel RS. Disruption of cell-cell adhesion enhances antibody-dependent cellular cytotoxicity: implications for antibody-based therapeutics of cancer. Cancer Res. 2002;62(23):6891-900.

123. Lavin SR, McWhorter TJ, Karasov WH. Mechanistic bases for differences in passive absorption. J Exp Biol. 2007;210(Pt 15):2754-64.

124. Lipinski CA, Lombardo F, Dominy BW, Feeney PJ. Experimental and computational approaches to estimate solubility and permeability in drug discovery and development settings. Adv Drug Deliv Rev. 2001;46(1-3):3-26.

125. Wang H, Yumul R, Cao H, Ran L, Fan X, Richter M, et al. Structural and functional studies on the interaction of adenovirus fiber knobs and desmoglein 2. J Virol. 2013;87(21):11346-62.

126. Barrios K, Celis E. TriVax-HPV: an improved peptide-based therapeutic vaccination strategy against human papillomavirus-induced cancers. Cancer Immunol Immunother. 2012;61(8):1307-17.

127. Cho HI, Barrios K, Lee YR, Linowski AK, Celis E. BiVax: a peptide/poly-IC subunit vaccine that mimics an acute infection elicits vast and effective anti-tumor CD8 T-cell responses. Cancer Immunol Immunother. 2013;62(4):787-99.

128. Bianchi F, Pretto S, Tagliabue E, Balsari A, Sfondrini L. Exploiting poly(I:C) to induce cancer cell apoptosis. Cancer Biol Ther. 2017;18(10):747-56.

129. Muller E, Christopoulos PF, Halder S, Lunde A, Beraki K, Speth M, et al. Toll-Like Receptor Ligands and Interferon-gamma Synergize for Induction of Antitumor M1 Macrophages. Front Immunol. 2017;8:1383.

130. Shime H, Kojima A, Maruyama A, Saito Y, Oshiumi H, Matsumoto M, et al. Myeloid-derived suppressor cells confer tumor-suppressive functions on natural killer cells via polyinosinic:polycytidylic acid treatment in mouse tumor models. J Innate Immun. 2014;6(3):293-305.

131. Shime H, Matsumoto M, Oshiumi H, Tanaka S, Nakane A, Iwakura Y, et al. Toll-like receptor 3 signaling converts tumor-supporting myeloid cells to tumoricidal effectors. Proc Natl Acad Sci U S A. 2012;109(6):2066-71.

132. Durmort C, Stehlin C, Schoehn G, Mitraki A, Drouet E, Cusack S, et al. Structure of the fiber head of Ad3, a non-CAR-binding serotype of adenovirus. Virology. 2001;285(2):302-12.

133. Lausch V, Hermann P, Laue M, Bannert N. Silicon nitride grids are compatible with correlative negative staining electron microscopy and tip-enhanced Raman spectroscopy for use in the detection of micro-organisms. J Appl Microbiol. 2014;116(6):1521-30.

134. Fender P, Hall K, Schoehn G, Blair GE. Impact of human adenovirus type 3 dodecahedron on host cells and its potential role in viral infection. J Virol. 2012;86(9):5380-5.

135. Humphrey W, Dalke A, Schulten K. VMD: visual molecular dynamics. J Mol Graph. 1996;14(1):33-8, 27-8.

136. Breitz HB, Weiden PL, Beaumier PL, Axworthy DB, Seiler C, Su FM, et al. Clinical optimization of pretargeted radioimmunotherapy with antibody-streptavidin conjugate and 90Y-DOTA-biotin. J Nucl Med. 2000;41(1):131-40.

137. Domingo RJ, Reilly RM. Pre-targeted radioimmunotherapy of human colon cancer xenografts in athymic mice using streptavidin-CC49 monoclonal antibody and 90Y-DOTA-biotin. Nucl Med Commun. 2000;21(1):89-96.

138. Green DJ, Frayo SL, Lin Y, Hamlin DK, Fisher DR, Frost SH, et al. Comparative Analysis of Bispecific Antibody and Streptavidin-Targeted Radioimmunotherapy for B-cell Cancers. Cancer Res. 2016.

139. Heppeler A, Froidevaux S, Eberle AN, Maecke HR. Receptor targeting for tumor localisation and therapy with radiopeptides. Curr Med Chem. 2000;7(9):971-94.

140. Janssen M, Frielink C, Dijkgraaf I, Oyen W, Edwards DS, Liu S, et al. Improved tumor targeting of radiolabeled RGD peptides using rapid dose fractionation. Cancer Biother Radiopharm. 2004;19(4):399-404.

141. Zhang WJ, Luo X, Song G, Wang XY, Shao XX, Guo ZY. Design, recombinant expression and convenient A-chain N-terminal europium-labelling of a fully active human relaxin-3 analogue. FEBS J. 2012;279(8):1505-12.

142. DeNardo SJ, Kukis DL, Miers LA, Winthrop MD, Kroger LA, Salako Q, et al. Yttrium-90-DOTA-peptide-chimeric L6 radioimmunoconjugate: efficacy and toxicity in mice bearing p53 mutant human breast cancer xenografts. J Nucl Med. 1998;39(5):842-9.

143. Deshpande SV, DeNardo SJ, Kukis DL, Moi MK, McCall MJ, DeNardo GL, et al. Yttrium-90-labeled monoclonal antibody for therapy: labeling by a new macrocyclic bifunctional chelating agent. J Nucl Med. 1990;31(4):473-9.

144. Giblin MF, Gali H, Sieckman GL, Owen NK, Hoffman TJ, Forte LR, et al. In vitro and in vivo comparison of human Escherichia coli heat-stable peptide analogues incorporating the 111In-DOTA group and distinct linker moieties. Bioconjug Chem. 2004;15(4):872-80.

145. Sosabowski JK, Mather SJ. Conjugation of DOTA-like chelating agents to peptides and radiolabeling with trivalent metallic isotopes. Nat Protoc. 2006;1(2):972-6.

146. Hasimu A, Ge L, Li QZ, Zhang RP, Guo X. Expressions of Toll-like receptors 3, 4, 7, and 9 in cervical lesions and their correlation with HPV16 infection in Uighur women. Chin J Cancer. 2011;30(5):344-50.

147. Cancer Statistics: National Cancer Institute; 2018 [Available from: https://www.cancer.gov/about-cancer/understanding/statistics.

148. Mirzaei HR, Rodriguez A, Shepphird J, Brown CE, Badie B. Chimeric antigen receptors T cell therapy in solid tumor: challenges and clinical applications. Frontiers in immunology. 2017;8:1850.

149. Cho K, Wang X, Nie S, Shin DM. Therapeutic nanoparticles for drug delivery in cancer. Clinical cancer research. 2008;14(5):1310-6.

150. Monneret C, editor Platinum anticancer drugs. From serendipity to rational design. Annales pharmaceutiques francaises; 2011: Elsevier.

151. L Arias J. Drug targeting strategies in cancer treatment: an overview. Mini reviews in medicinal chemistry. 2011;11(1):1-17.

152. Jiang K, Rankin CR, Nava P, Sumagin R, Kamekura R, Stowell SR, et al. Galectin-3 regulates desmoglein-2 and intestinal epithelial intercellular adhesion. Journal of Biological Chemistry. 2014;289(15):10510-7.

153. Wang H, Ducournau C, Saydaminova K, Richter M, Yumul R, Ho M, et al. Intracellular signaling and desmoglein 2 shedding triggered by human adenoviruses Ad3, Ad14, and Ad14P1. Journal of virology. 2015;89(21):10841-59.

154. Chen L, Liu X, Zhang J, Liu Y, Gao A, Xu Y, et al. Characterization of desmoglein 2 expression in ovarian serous tumors and its prognostic significance in high-grade serous carcinoma. International Journal of Clinical and Experimental Pathology. 2018;11(10):4977.

155. Hüttenhain R, Choi M, de la Fuente LM, Oehl K, Chang C-Y, Zimmermann A-K, et al. A targeted mass spectrometry strategy for developing proteomic biomarkers: a case study of epithelial ovarian cancer. Molecular & Cellular Proteomics. 2019;18(9):1836-50.

156. Cai F, Zhu Q, Miao Y, Shen S, Su X, Shi Y. Desmoglein-2 is overexpressed in non-small cell lung cancer tissues and its knockdown suppresses NSCLC growth by regulation of p27 and CDK2. Journal of cancer research and clinical oncology. 2017;143(1):59-69.

157. Tan LY, Mintoff C, Johan MZ, Ebert BW, Fedele C, Zhang YF, et al. Desmoglein 2 promotes vasculogenic mimicry in melanoma and is associated with poor clinical outcome. Oncotarget. 2016;7(29):46492.

158. Han C, Yu Y, Wang A, Tian Y, Zhang H, Zheng Z, et al. Desmoglein-2 overexpression predicts poor prognosis in hepatocellular carcinoma patients. Eur Rev Med Pharm Sci. 2018;22:5481-9.

159. Beyer I, van Rensburg R, Lieber A. Overcoming physical barriers in cancer therapy. Tissue Barriers. 2013;1(1):3340-51.

160. Pitner R, Kim J, Davis-Bergthold J, Turner C, Vassal-Stermann E, Wang H, et al. structure-based Design of JoC-x, a Conjugatable tumor tight Junction opener to enhance Cancer therapy. Scientific reports. 2019;9(1):1-13.

161. Yumul R, Richter M, Lu Z-Z, Saydaminova K, Wang H, Wang C-HK, et al. Epithelial junction opener improves oncolytic adenovirus therapy in mouse tumor models. Human gene therapy. 2016;27(4):325-37.

162. Beyer I, Cao H, Persson J, Song H, Richter M, Feng Q, et al. Coadministration of epithelial junction opener JO-1 improves the efficacy and safety of chemotherapeutic drugs. Clinical cancer research. 2012;18(12):3340-51.

163. Richter M, Yumul R, Wang H, Saydaminova K, Ho M, May D, et al. Preclinical safety and efficacy studies with an affinity-enhanced epithelial junction opener and PEGylated liposomal doxorubicin. Molecular Therapy-Methods & Clinical Development. 2015;2:15005.

164. Ravasco JM, Faustino H, Trindade A, Gois PM. Bioconjugation with maleimides: A useful tool for chemical biology. Chemistry–A European Journal. 2019;25(1):43-59.

165. Schiffelers RM, Koning GA, ten Hagen TL, Fens MH, Schraa AJ, Janssen AP, et al. Anti-tumor efficacy of tumor vasculature-targeted liposomal doxorubicin. Journal of Controlled Release. 2003;91(1-2):115-22.

166. Seo JW, Mahakian LM, Kheirolomoom A, Zhang H, Meares CF, Ferdani R, et al. Liposomal Cu-64 labeling method using bifunctional chelators: poly (ethylene glycol) spacer and chelator effects. Bioconjugate chemistry. 2010;21(7):1206-15.

167. Altai M, Membreno R, Cook B, Tolmachev V, Zeglis BM. Pretargeted Imaging and Therapy. J Nucl Med. 2017;58(10):1553-9.

168. Fontaine SD, Reid R, Robinson L, Ashley GW, Santi DV. Long-term stabilization of maleimide–thiol conjugates. Bioconjugate chemistry. 2015;26(1):145-52.

169. Arcamone F, Cassinelli G, Fantini G, Grein A, Orezzi P, Pol C, et al. Adriamycin, 14-hydroxydaimomycin, a new antitumor antibiotic from S. Peucetius var. caesius. Biotechnology and Bioengineering. 1969;11(6):1101-10.

170. Johnson-Arbor K, Patel H, Dubey R. Doxorubicin. StatPearls [Internet]: StatPearls Publishing; 2019.

171. Tacar O, Sriamornsak P, Dass CR. Doxorubicin: an update on anticancer molecular action, toxicity and novel drug delivery systems. Journal of Pharmacy and Pharmacology. 2013;65(2):157-70.

172. Fornari FA, Randolph JK, Yalowich JC, Ritke MK, Gewirtz DA. Interference by doxorubicin with DNA unwinding in MCF-7 breast tumor cells. Mol Pharmacol. 1994;45(4):649-56.

173. Nguyen J, Solimando DA, Jr., Waddell JA. Carboplatin and Liposomal Doxorubicin for Ovarian Cancer. Hosp Pharm. 2016;51(6):442-9.

174. Olson RD, Mushlin PS. Doxorubicin cardiotoxicity: analysis of prevailing hypotheses. The FASEB journal. 1990;4(13):3076-86.

175. Tardi P, Boman N, Cullis P. Liposomal doxorubicin. Journal of drug targeting. 1996;4(3):129-40.

176. Green AE, Rose PG. Pegylated liposomal doxorubicin in ovarian cancer. Int J Nanomedicine. 2006;1(3):229-39.

177. Barenholz YC. Doxil®—the first FDA-approved nano-drug: lessons learned. Journal of controlled release. 2012;160(2):117-34.

178. Liposomal Doxorubicin Market Analysis By Product, (J&J [Doxil/Caelyx], Sun Pharma [Lipodox], Teva [Myocet], Others), By Application, (Multiple Myeloma, Kaposi Sarcoma, Ovarian, Breast, Kidney Cancer), And Segment Forecasts, 2018 - 2024. Grand View Research; 2015.

179. Vogels R, Zuijdgeest D, van Rijnsoever R, Hartkoorn E, Damen I, de Béthune MP, et al. Replication-deficient human adenovirus type 35 vectors for gene transfer and vaccination: efficient human cell infection and bypass of preexisting adenovirus immunity. J Virol. 2003;77(15):8263-71.

180. Alberts DS, Garcia DJ. Safety aspects of pegylated liposomal doxorubicin in patients with cancer. Drugs. 1997;54(4):30-5.

181. Doxil(R) - Package Insert. 2007.

182. Handolias D, Quinn M, Foo S, Mileshkin L, Grant P, Dutu G, et al. Oral cyclophosphamide in recurrent ovarian cancer. Asia‐Pacific Journal of Clinical Oncology. 2016;12(1):e154-e60.

183. Alberts DS, Liu P, Hannigan EV, O'Toole R, Williams SD, Young JA, et al. Intraperitoneal cisplatin plus intravenous cyclophosphamide versus intravenous cisplatin plus intravenous cyclophosphamide for stage III ovarian cancer. New England Journal of Medicine. 1996;335(26):1950-5.

184. McGuire WP, Hoskins WJ, Brady MF, Kucera PR, Partridge EE, Look KY, et al. Cyclophosphamide and cisplatin compared with paclitaxel and cisplatin in patients with stage III and stage IV ovarian cancer. New England Journal of Medicine. 1996;334(1):1-6.

185. Warren JS, Ward PA. Immune Complex Diseases. eLS2017. p. 1-9.

186. Norelli M, Camisa B, Barbiera G, Falcone L, Purevdorj A, Genua M, et al. Monocyte-derived IL-1 and IL-6 are differentially required for cytokine-release syndrome and neurotoxicity due to CAR T cells. Nature medicine. 2018;24(6):739-48.

187. Zhang C, Wu Z, Li J-W, Zhao H, Wang G-Q. The cytokine release syndrome (CRS) of severe COVID-19 and Interleukin-6 receptor (IL-6R) antagonist Tocilizumab may be the key to reduce the mortality. International journal of antimicrobial agents. 2020:105954.

188. Moore JB, June CH. Cytokine release syndrome in severe COVID-19. Science. 2020;368(6490):473-4.

189. Szebeni J, Baranyi L, Savay S, Milosevits J, Bunger R, Laverman P, et al. Role of complement activation in hypersensitivity reactions to doxil and hynic PEG liposomes: experimental and clinical studies. Journal of liposome research. 2002;12(1-2):165-72.

190. Wenande E, Garvey LH. Immediate-type hypersensitivity to polyethylene glycols: a review. Clinical & Experimental Allergy. 2016;46(7):907-22.

191. Judge A, McClintock K, Phelps JR, MacLachlan I. Hypersensitivity and loss of disease site targeting caused by antibody responses to PEGylated liposomes. Molecular Therapy. 2006;13(2):328-37.

192. Thanou M, Duncan R. Polymer-protein and polymer-drug conjugates in cancer therapy. Current opinion in investigational drugs (London, England: 2000). 2003;4(6):701-9.

193. Deshpande PP, Biswas S, Torchilin VP. Current trends in the use of liposomes for tumor targeting. Nanomedicine (Lond). 2013;8(9):1509-28.

194. Immordino ML, Dosio F, Cattel L. Stealth liposomes: review of the basic science, rationale, and clinical applications, existing and potential. Int J Nanomedicine. 2006;1(3):297-315.